博士論文

Investigation of heat and mass transfer mechanisms of water droplets in upward air stream with simultaneous measurements of internal temperature and flow distributions

(温度速度分布同時計測法を用いた上昇流中の液滴における熱と質量の輸送に関する研究)

周騫

Investigation of heat and mass transfer mechanisms of water droplets in upward air stream with simultaneous measurements of internal temperature and flow distributions

A dissertation submitted to

The University of Tokyo

In partial fulfillment of the requirements

For the degree of

Doctor of Philosophy

In

Nuclear Engineering & Management

By

Qian ZHOU

July 2017

Advisor: Nejdet ERKAN, Project Associate Professor, Department of Nuclear Engineering and Management

Contents

Nomenclature

Symbol	Description
I	Intensity of phosphorescence emission
t	Elapsed time
τ	Phosphorescence decay constant
K_{II}	WII coefficient
k_r	Chemical reaction rate constant
T	Temperature
A	Pre-exponential factor
E_a	Activation energy
R_g	Universal gas constant
$\overline{(\Delta x)^2}$	Mean squared displacement
D	Diffusion constant
k_B	Boltzmann constant
η	Viscosity
a	Radius of Brownian particles
n	Index of refraction
φ	Angle of incidence (in chapter 2)
h	Radial distance
R	Droplet diameter
(x, y)	2D Cartesian coordinates
(r, θ)	2D polar coordinates
(u, v)	Velocities in Cartesian coordinates
v	Velocity
Nu	Nusselt number
Re	Reynolds number
Pr	Prandtl number
Sh	Sherwood number
Sc	Schmidt number
B_H	Heat transfer number
B_M	Mass transfer number
k	Thermal conductivity
ρ	Density
μ	Dynamic viscosity
c_p	Specific heat at constant pressure
L	Latent heat of liquid
Y	Vapor mass fraction
h	Heat transfer coefficient
K	Mass transfer coefficient

D_m	Mass diffusivity
Δt	Evaporation time
A	Area of droplet surface
M	Molar mass
c_A	Molar concentration of the evaporating species
P	Vapor partial pressure
φ	Humidity (in chapter 4)
ΔT	Temperature increase of droplet
m	Mass of evaporating droplet

Subscripts	Description
0	Initial (in chapter 2)
t	Momentary (in chapter 2)
i	Detected (in chapter 2)
o	Phosphorescence
a	Air
d	Droplet
0	On object plane (in chapter 3)
i	On image plane (in chapter 3)
r	Radial component
t	Tangential component (in chapter 3)
L	Liquid
∞	Gas stream
g	Gas
s	Surface, saturated
$vapor$	Vapor

Figure list

Table list

1. Introduction

1.1. Containment spray system

1.1.1.General introduction of containment spray system

A containment vessel is a reinforced steel structure enclosing a nuclear reactor. It is designed, in any emergency, to contain the escape of radiation to a maximum pressure in the range of 410 to 1400 kPa, as the fourth and final barrier to radioactive release. In case of a severe accident in a LWR, a probable pipe failure, therewith coolant leakage, may result in a high temperature and pressure circumstance inside the containment.

The high temperature and overpressure condition inside the containment can be extremely dangerous because it may cause structural failure and destroy the leak tightness of the containment vessel. Besides, some amount of hydrogen might be produced by the reactor fuel cladding oxidation and can be spread to the whole containment volume, which may induce a risk of locally flammable or even explosive gas mixtures in the containment.

One of the accident mitigation systems used in nuclear power plants is the spray system inside the containment vessel. As shown in Figure 1-1 [1], containment spray nozzles are usually installed at the top inside the containment. During reactor accidents, the containment spray can reduces the high pressure generated by condensing the steam and cooling the gas atmosphere inside the containment vessel.
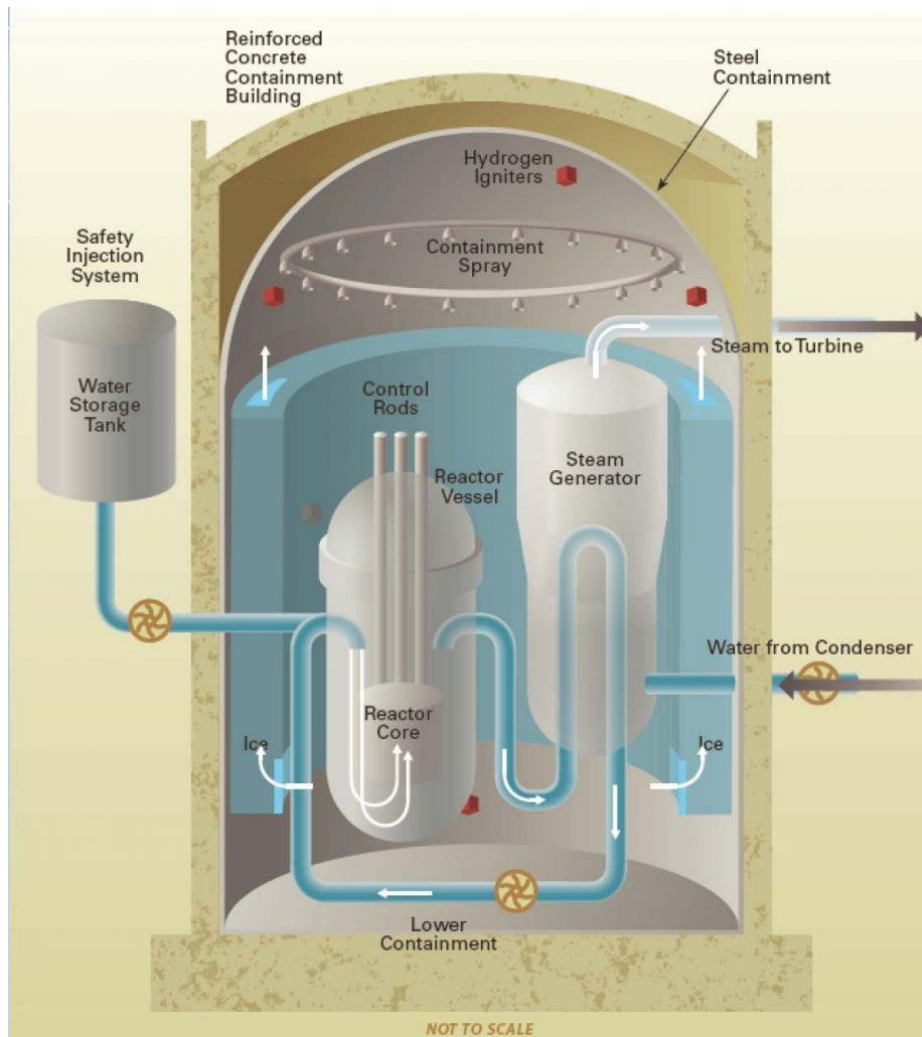
Figure 1-1. Accident mitigation systems inside containment vessel including
containment spray cooling [1]

1.1.2. Cooling and depressurization mechanisms of containment spray

The cooling and depressurization behavior of containment spray is a complicated heat and mass transfer process including phase-change. It is essential important to provide a good understanding with an effective estimation methodology of the heat and mass transfer that take place between a spray and the surrounding confined gas for reactor safety system design and failure analysis.

Different from the common spray cooling objective to cool down hot surface, containment spray systems perform as space spray with several phases and following features: a). heat and mass transfer on falling droplets becomes the dominant mechanisms; b). at the beginning of the spray, the evaporation of the flying droplets massively occurred, cooled down the circumstance inside the containment vessel, and the vapor saturation ratio increased fast; c). the circumstance inside the containment became near saturated condition in a short time, afterwards, the direct contact condensation on droplets became the dominant mechanism, and newly injected low temperature spray mixing (heat transfer) results in temperature decrease.

As shown in Figure 1-2 [2], the global characterization of the spray test inside containment vessel experimental facility demonstrated three phases A, B and C before equilibrium phase D. In phase A, the mean gas temperature inside the vessel decreased rapidly, because of massive spray droplets evaporation. The vapor saturation ratio increased to approximately 1 within a short time (116s in the test), and there was also some increase in the gas mole number, which means that the pressure inside the vessel may also increase a little at the beginning of the spray due to droplets evaporation. Thereafter, in phase B, the circumstance inside the containment became near saturated condition. Droplet evaporation may still occurred in some unsaturated region, but the decrease in gas mole number indicated this phase to be a global condensing phase. The mean gas temperature decreased mainly due to the convective heat transfers between the gas and injected low temperature droplets. The gas in the containment became globally saturated at the end of phase B. Phase C was the saturated phase, in which newly injected low temperature spray cooled the gas and consequently the direct contact condensation on droplets became the dominant mechanism, which induced the decrease in gas mole number (depressurization).
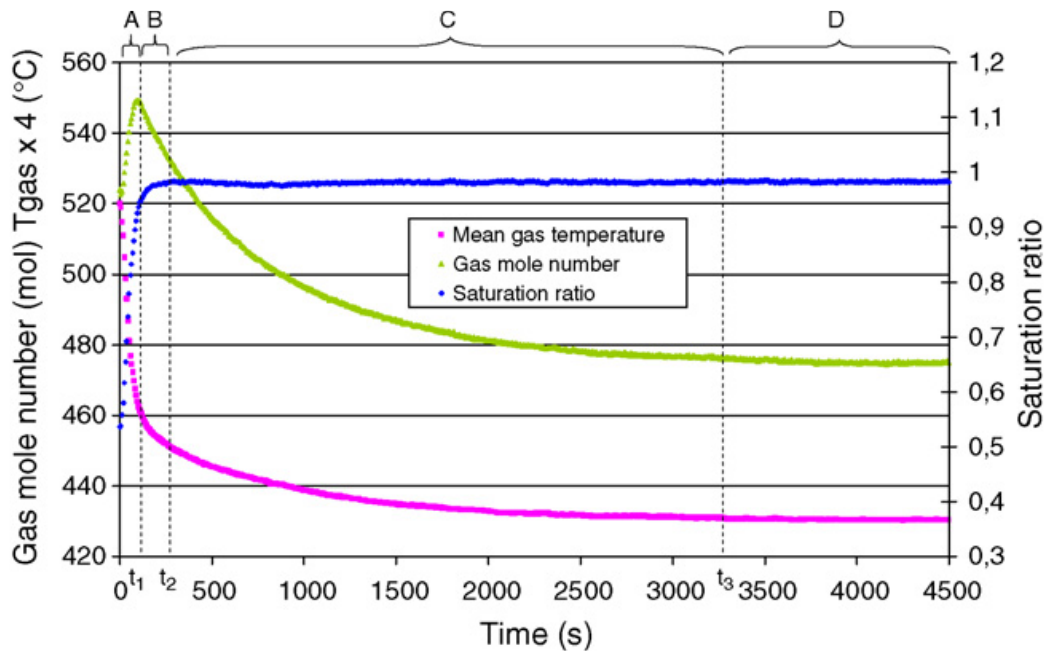
Figure 1-2. Global characterization of the spray test [2]

After approximately 1 hour of spray, the containment spray stepped into the final equilibrium phase D. In this phase, the heat removed from the gas mixture by the injected droplets was considered to be compensated by the heat flux transferred to the gas by the heated walls. Therefore, the gas temperature remained constant and neither evaporation nor condensation may occurred on the surface of droplets.

1.2. Review of previous research on containment spray

1.2.1. Experimental and numerical research on spray

In recent years, containment vessel experimental facilities equipped with spray system have been constructed for compositive large-scale experimental researches to simulate typical accidental thermal-hydraulic flow conditions in the containment vessel. Numerous studies have been conducted to investigate the heat and mass transfer performance of containment sprays experimentally in large containment vessel experimental facilities with various numerical simulations.

1) Large-scale experimental facilities and related studies

4

For example, the TOSQAN facility constructed in France is a large stainless steel cylindrical enclosure devoted to simulate typical thermal hydraulic flow conditions representative of a severe accident in nuclear-pressurized water reactor (PWR) containment. The specificity of the TOSQAN facility is characterized by a high level of instrumentation that provides detailed information on local and non-intrusive characterization of the two-phase flow for CFD codes validation. The overview of the TOSQAN facility is shown in Figure 1-3. [3] Spray system is installed inside the facility with optical diagnostics equipment. Steam can be injected into the vessel from the lower injection nozzle to simulate the accidental circumstance in the reactor containment vessel. A helium nozzle is also equipped for hydrogen simulation, to study light non-condensable gas mixing caused by spray activation.
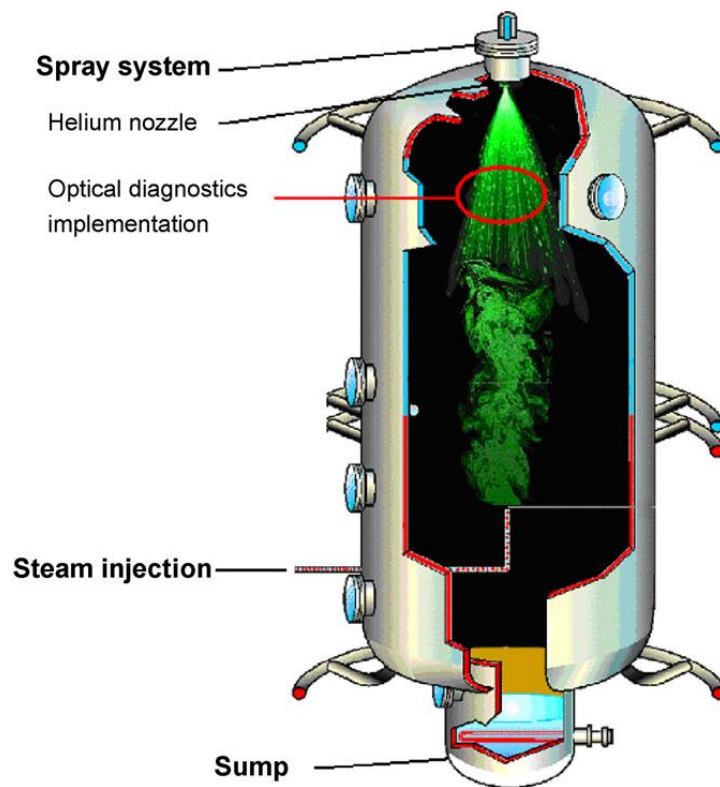
Figure 1-3. Overview of the TOSQAN facility [3]

Various researches on containment spray have been conducted experimentally in the TOSQAN facility, such as studies on different spray operating parameters (e.g. spray mass flow rate, spray temperature at the injection point). With overall spray

visualization and measurements for the characterization of spray clouds, gas temperature, droplets velocity, droplet size and steam fraction were obtained locally inside the vessel, and the containment spray performance was investigated from very local phenomena to global behavior with the experiment data. The four phases global dynamics (vaporization, condensation, and mixing) introduced in Section 1.1.2 has been reported and an analytically calculation method has been developed to quantify the intensity of these exchanges using the enthalpy balance equation in order to establish the theoretical gas cooling rates and equilibrium temperatures. [2, 4]
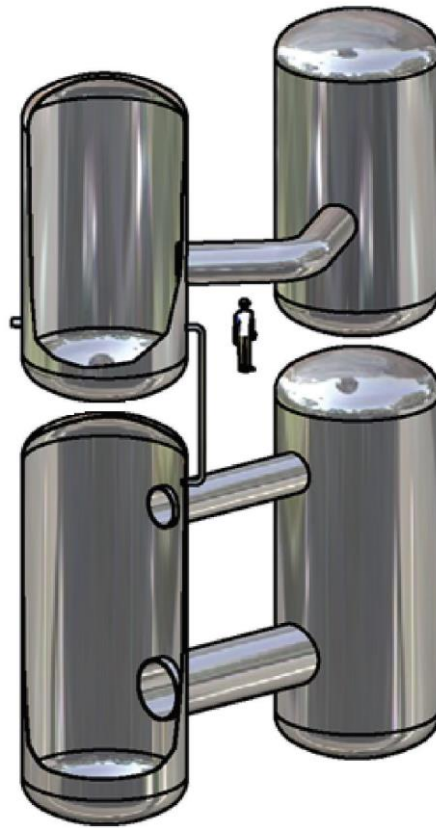
Figure 1-4. Schematic for the multi-compartment geometry of the PANDA facility [5]

The PANDA facility is another large-scale experimental facility for safety investigations of reactor containment vessel, which is a multi-compartmental thermal hydraulic facility located in Switzerland. The facility is multipurpose, and the applications cover integral containment response tests, component tests, primary system tests, and separate effect tests. Figure 1-4 gives a schematic for the multi-compartment geometry of the PANDA facility. [5]

Because the PANDA facility consists of six thermally insulated stainless steel cylindrical vessels with interconnecting pipes, researches focusing on the helium layer breakup and mass transfer between the compartments during postulated accidents can be conducted experimentally using several vessels with locally equipped diagnostics devices for gas atmosphere (such as pressure, temperature, helium molar fraction). For example, experiments have been done by O. Auban et al. [6] in order to investigate the large-scale gas mixing and stratification phenomena during steam injection related to LWR containment studies inside two upper vessels of the PANDA facility. Further investigations have been done by N. Erkan et al. [7] to evaluate the effects of water sprays on the mitigation of containment pressure for the cases of two non-condensable gases (i.e. air-helium) and only one non-condensable gas (i.e. helium), and the effect of stratified helium layer breakup and initial gas composition on the transient behavior of depressurization and mass transport has also been investigated. The results showed that the spray activation is very effective to mix the gas atmosphere and mitigate the overall containment pressure.

2) Numerical studies

These experimental researches have provided a good deal of data for theoretical investigations to evaluate the containment spray system behavior.

M. Babić [8] et al. have developed two- and three-dimensional models of the TOSQAN vessel. The modelling used an Eulerian description of the continuous phase (gas), a Lagrangian description of the dispersed phase (spray droplets), and a two-way interaction between the phases. Droplets were modelled as sources or sinks of energy, mass and momentum in the single-phase gaseous field. The mass and heat transfer of flying droplets was calculated with widely used Ranz and Marshall correlations. In their calculations, the evaporation of deposited droplets was also considered as a simple droplet–wall interaction model. Figure 1-5 shows the comparison of the pressure evolutions for TOSQAN 101 spray test and their calculation results. It can be observed that the depressurization rate was over-predicted in their calculations.
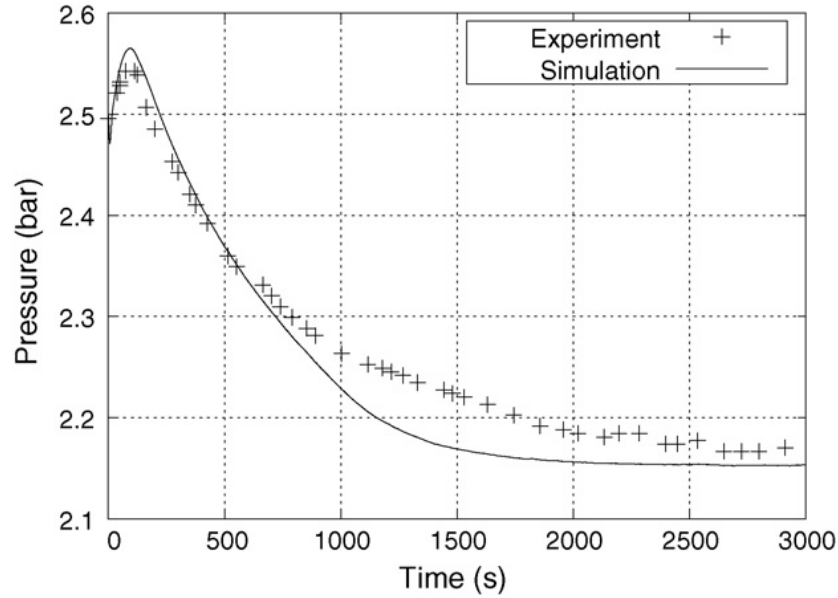
Figure 1-5. TOSQAN 101 spray test — comparison of measured and calculated

pressure evolutions [8]

S. Mimouni et al. [9] have developed a spray modelling implemented in NEPTUNE CFD for TOSQAN spray tests. In their models, the droplet evaporation at the wall has also been taken into consideration. Their calculations managed to reproduce the mixing of helium by the spray, and they believed that the prediction of the transient behavior should be improved by including in the model corrections based on better understanding of the influence of the dispersed phase on the turbulence of the continuous phase. Figure 1-6 shows the comparison between the spray test and their calculation of the pressure evolution. The depressurization rate was over-predicted as well in their calculations.
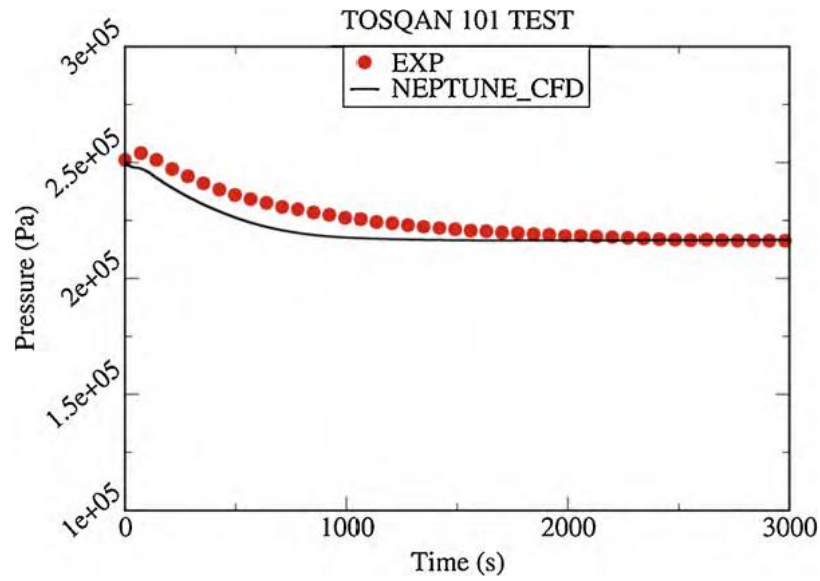
Figure 1-6. TOSQAN 101 spray test — time evolution of the pressure [9]

S. Mimouni et al. [10] have also applied their spray model in the large-scale thermal-hydraulic PANDA test facility. The interfacial heat and mass transfer between droplets and gas was calculated using the correlations of Frössling/Ranz-Marshall in their models. The results also indicated the over-prediction of depressurization rate inside the vessel (shown in Figure 1-7).
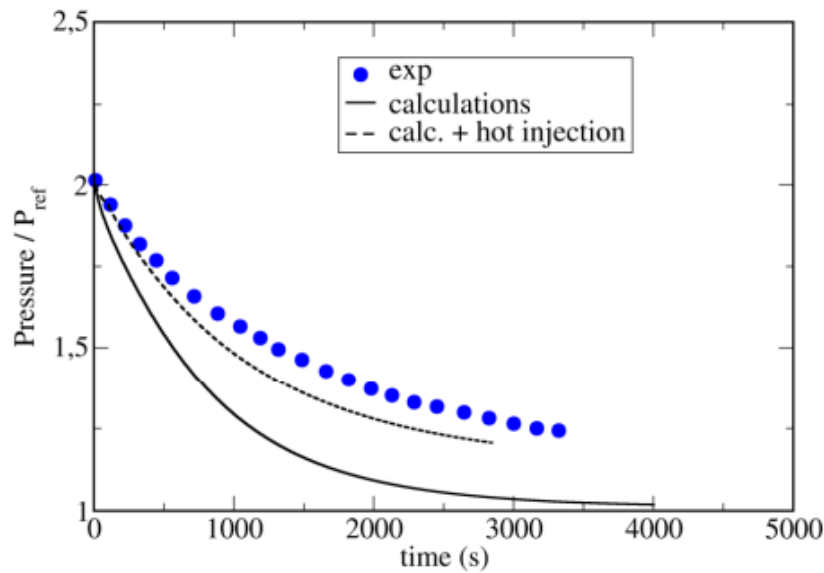
Figure 1-7. TOSQAN 101 spray test — time evolution of the pressure [10]

M. Andreani and N. Erkan [11] have reported their numerical investigation on the effect of spray on the gas mixing in the multi-compartment geometry of the PANDA facility using the GOTHIC code. Standard correlations are used in GOTHIC for calculating heat and mass transfer between the droplets and the surrounding gas. For convective heat transfer between fluid and walls standard correlations are implemented in GOTHIC for natural convection. Their code also tended to over-predict the depressurization rate, and the temperature decrease of gas temperature was over-predicted as well (see Figure 1-8 and Figure 1-9).
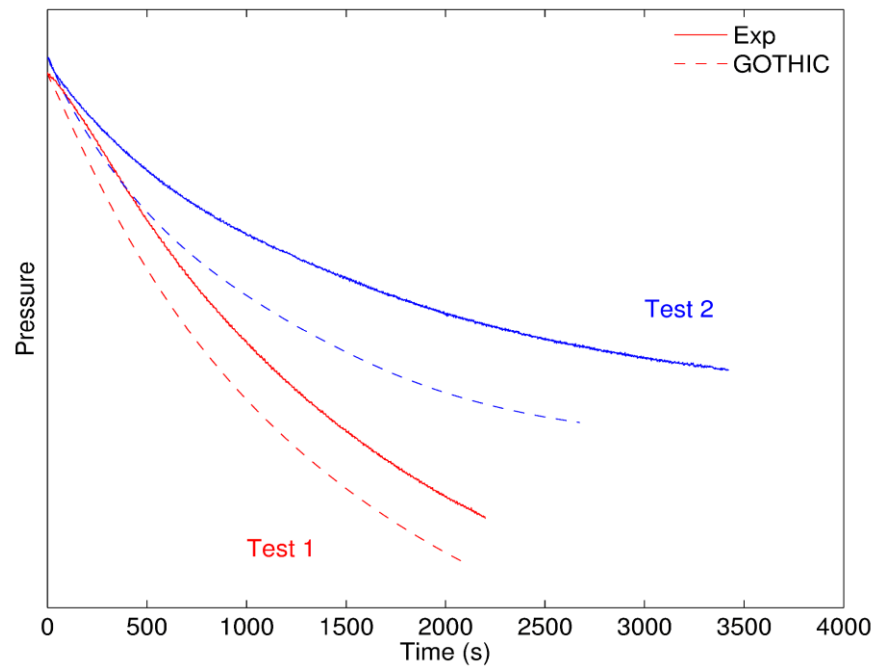
Figure 1-8. PANDA spray test — comparison between calculated and measured pressure [11]
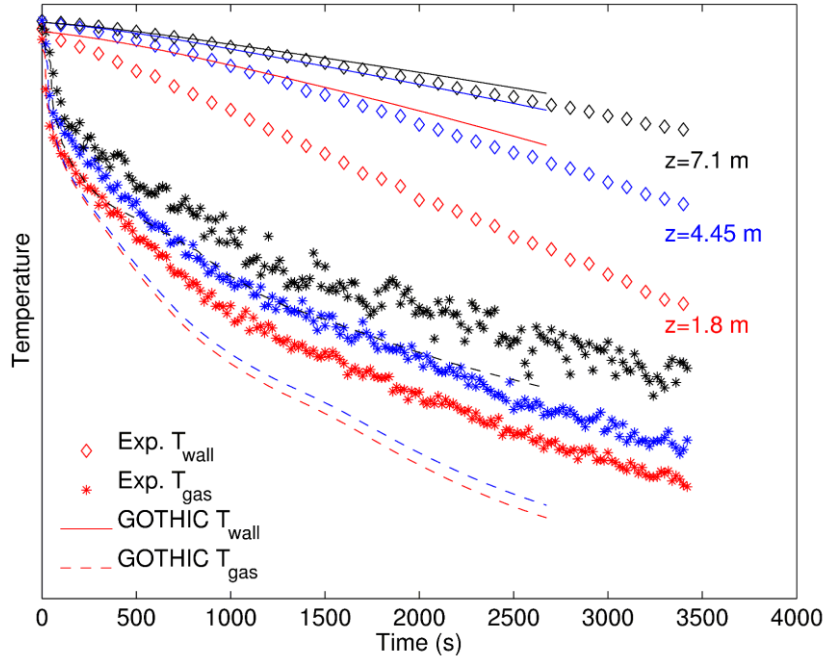
Figure 1-9. PANDA spray test — comparison of wall and gas temperature at various elevations in vessel [11]

Above-mentioned researches, up to now, various numerical simulations with sophisticated computational fluid dynamics (CFD) models have not been able to reproduce the depressurization and gas mixture flows adequately. Although many researches have been done for the thermo-hydraulic studies on containment spray cooling including overall spray visualization and measurements, the detailed investigations, especially experimental studies, have not been conducted enough to provide a complete fundamental understanding for the mechanisms of droplet mass and heat transfer.

1.2.2. Fundamental research on droplet heat and mass transfer

One of the important factors governing the spray cooling and depressurization is based on the mechanisms of heat and mass transfer between flying liquid droplets and the surrounding gas which are modelled with various empirical correlations. However,

most of the CFD codes do not take into account of the droplet's internal thermal-hydraulic conditions, which contain highly transient exchange phenomena.

As mentioned above, some existing well-known correlations are widely used to calculate the heat and mass transfer of flying droplets, such as Frössling correlation and Ranz & Marshall correlation. Researchers have been working on finding an effective and sufficiently accurate calculation method to evaluate the behavior of spray droplets for decades. The theory of droplet thermal-hydraulic behavior has been systematically developed and introduced in academic books [12, 13]. M. Birouk and I. Gökalp [14] have given a remarkable overview of current research status of droplet evaporation in turbulent flows.

Internal flow may developed inside the flying droplets in mixture gas due to the shear force of air stream on droplet surface. This kind of vorticity distributed within a liquid sphere is known as the Hill's spherical vortex [15]. The internal flow is usually consider to enhance the water mixing inside the flying droplets and influence mass and heat transfer. For example, the enhancement of internal mixing was modelled by introducing an enhanced liquid thermal conductivity by M. Renksizbulut and R. J. Haywood [16] during their calculations of transient droplet evaporation. Figure 1-10 shows one of the streamline figures of gas-phase and liquid-phase flow from their calculations. The internal motion driven by air stream can be clearly observed.
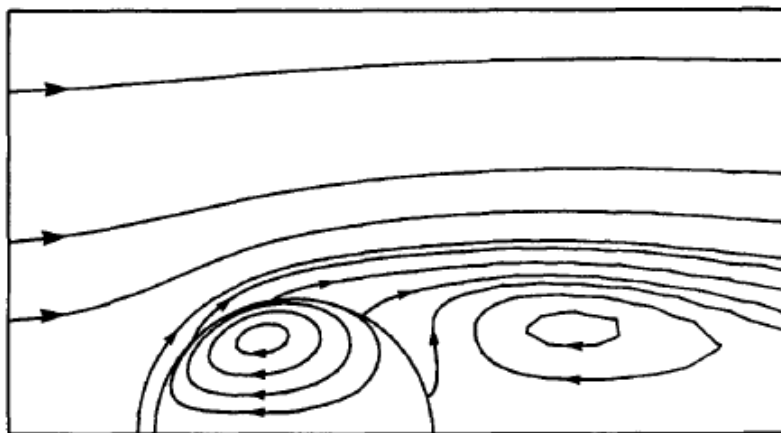
Figure 1-10. The flow field during the droplet evaporation period [16]

Massive researches on droplet vaporization model have been conducted for spray combustion calculations. Although the temperature and pressure range in these researches may be different from that in the containment spray, most of the calculation functions and methods are available in common. B. Abramzon and W. A. Sirignano [17] have given a detailed calculation model for droplet vaporization including gas phase and liquid phase analysis, and they also compared the calculation results using various existing models.

Since this heat and mass exchange is a complicated process including droplet internal flow circulation, heat and mass diffusion with phase change, the related mechanisms of flying spray droplets behaviors in surrounding gas mixture have not been fully understood yet. Currently, few experimental data has been reported for detailed temperature and flow measurements inside water droplets, especially for the beginning of droplet evaporation during the development of droplet internal circulation, which contains highly transient exchange phenomena and requires high time and spatial resolution of temperature and velocity measurement techniques.

1.3. Review of detailed measurement techniques

1.3.1. Optical thermometry

To investigate the phenomena of flying droplets at a fundamental level, the crucial task is to obtain detailed flow velocity and temperature distributions inside the droplets and study the interaction between the heat and mass transfer mechanisms.

Optical measurement techniques are widely employed for temperature and pressure measurements in multi-dimensional fields. Optical measurements are capable of providing high spatial resolution and high temperature and pressure sensitivity with good accuracy. Luminescence sensors can be effectively used for thermometry because they are based on the principle of temperature-dependent light emission. For example, laser-induced fluorescence can be used for temperature distribution measurements, both

on solid surfaces and in liquids [18, 19]. Phosphorescence materials can be used to measure temperature as well as pressure distribution; for example, in luminophore temperature- and pressure-sensitive paints [20].

Thermographic phosphors have also been used by A Omrane et al. [21] to measure the temperature distribution of both single droplets and sprays. Figure 1-11 shows their two-dimensional temperature measurements of a free falling droplet and the water spray. In their measurements, laser induced emission from thermographic phosphor seeded to the investigated liquid was detected by a fast framing camera. The technique they proposed can provides single shot figure of temperature distributions of droplets and spray field.
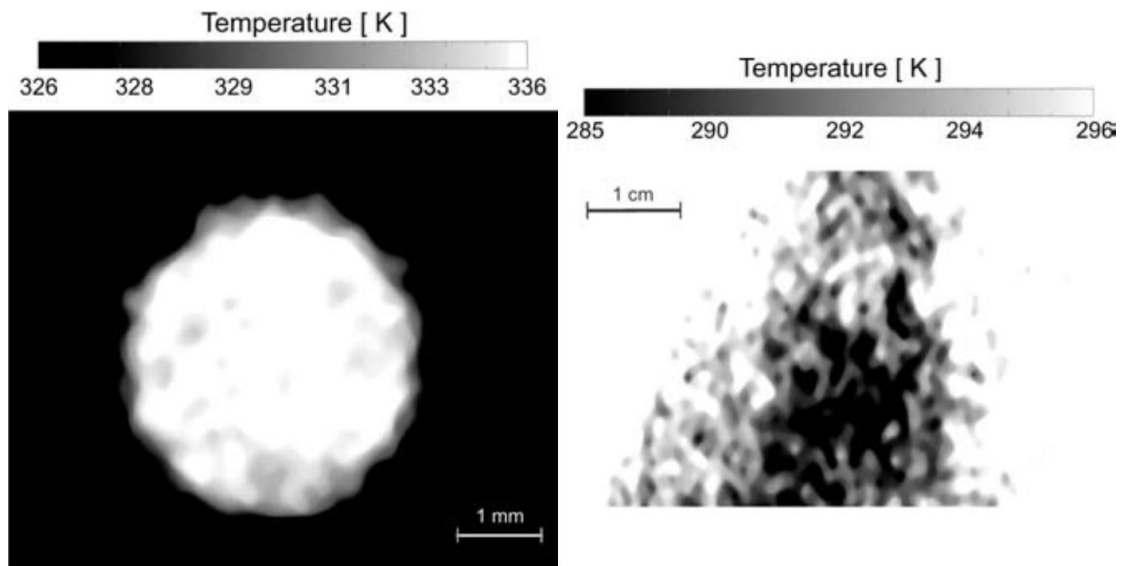
Figure 1-11. The two-dimensional temperature measurements of a free falling droplet and the water spray using thermographic phosphors [21]

The principle of optical thermometry can be easily explained. Figure 1-12 gives a decay curve of the phosphorescence emission intensity under ultra-violet laser excitation obtained in this study. The decay is exponential and the decay constant is a function of local temperature. Fluorescence also decay exponentially, but compared with phosphorescence, its lifetime is very short (nanoseconds). Therefore, laser induced

fluorescence techniques are usually intensity based and applied for highly instantaneous measurements such as a heated jet with turbulent heat transport and mixing [22].
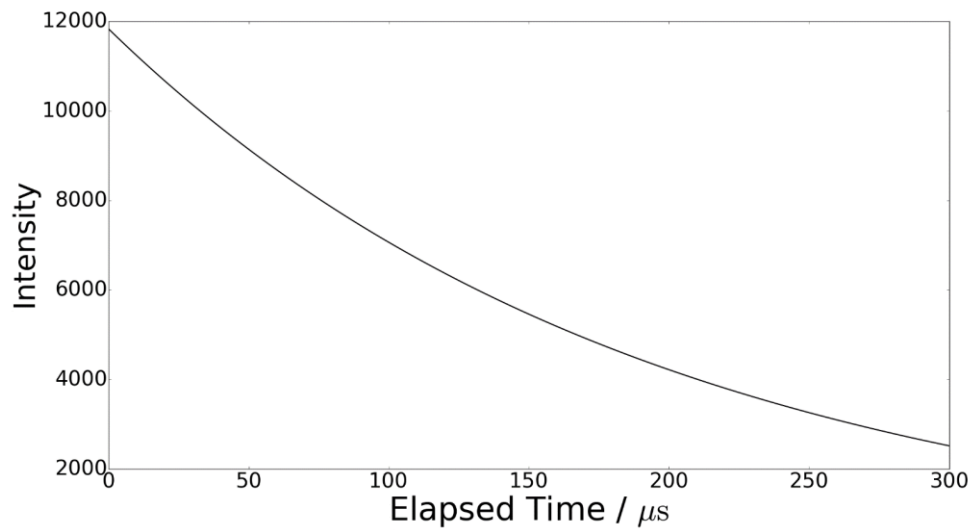
Figure 1-12. The exponential phosphorescence decay

Basically, temperature measurement techniques using luminescence sensors under pulsed laser excitation include two kinds of analyzing methods, intensity based method for the instant phenomenon fluorescence, and lifetime based method for the relatively persistent phenomenon phosphorescence. It is worth to noting that decay rate analysis is generally robust than intensity measuring, because it will not be obviously affected by changes in the light, sensor concentration, optical geometry and some other factors [20]. Besides, phosphor thermometry may also be free from momentary fluorescence emitted from materials other than the applied sensor.

1.3.2. Combined temperature and velocity measurements using PIV-TSP

In recent years, different kinds of detailed measurement systems that focus on millimeter-scale fluid domains have been investigated and developed. Particle image velocimetry (PIV), a well-established technique for flow visualization, is widely used for micro-flow velocity measurements. For example, N. Erkan et al. [23] investigated the spreading velocity inside a water droplet impinging onto a glass substrate using

time-resolved PIV. Confocal micro-PIV was used to perform the three-dimensional visualization of internal flow inside a droplet moving in a micro-channel [24]. Ninomiya et al. [25] performed PIV measurements to visualize the liquid–liquid flow around and inside a droplet of an aqueous solution of glycerol falling in silicone oil under the consideration that the refractive indices of glycerol and silicone oil match each other.

Optical temperature measurements can be combined with PIV by using a high-speed camera. In the past decades, this method has been developed and used to perform simultaneous velocity and temperature measurements for gas or liquid flow [22, 26–30]. For example, measurements of natural convection were performed in silicone oil from 22 °C to 52 °C using phosphor-dyed temperature-sensitive particles (TSP) as tracer particles for thermometry and PIV simultaneously [26, 27].

In the above-mentioned studies, the temperature measurement calibrations performed to obtain a correlation between phosphorescence light decay and local fluid temperatures were relatively easy because the calibration was mostly performed on the measurement device to reduce the error originating from local phosphorescence intensity differences induced by uneven particle density and laser illumination. However, in the combined measurement method, local pixel intensity differences are likely to be more significant than those in the thermographic phosphorescence method without PIV because the pixel intensity needs to be locally distinguishable for performing replacement calculations of the interrogation window in PIV analysis. Therefore, it is necessary to determine the effect of local intensity differences on the intensity decay constant. In addition, in-situ calibration may not always be possible on millimeter scales because of the limitations of temperature probing for the calibration, which requires the temperature to be stable and controllable.

1.4. Objective of this work

Currently, the existing computational models have difficulties in reproducing the depressurization rate and temperature decrease of the containment spray cooling adequately. One possible reason is that the widely used correlations can't well estimate the complicated phenomena of droplets heat and mass exchange with droplet internal convective motions. Previously, few experimental studies have been conducted on the heat and mass transfer of spray droplets concerning droplets internal flow due to the difficulties in simultaneous measurements of temperature and flow distributions inside water droplets.

The purpose of this study is to investigate the heat and mass transfer mechanisms of water droplets in air stream experimentally, and to evaluate the adequacy of the widely-used heat and mass transfer correlations for spray droplets. At current stage in this study, our research focused on the droplet evaporation behaviors in upward air stream, considering that the droplet evaporation is the dominate mechanism at the beginning of the containment spray in phase A, and the evaporation is the inverse process of condensation, therefore they can be evaluated with similar correlations, thus this investigation may also be helpful to improve our understanding of the phase B-D of containment spray.

In chapter 2, the PIV-TSP measurement technique was improved to apply the technique to study the transient phenomena of flying spray droplets. An ex-situ calibration method was developed to employ phosphorescence thermometry for the investigation of heat and mass transfer in small-scale geometries such as the one inside evaporating pendant water droplets, and the effect of local noise was discussed and quantified.

In chapter 3, the improved technique was used to measure the temperature and flow distributions inside evaporating water droplets with an anti-distortion algorithm to correct the systematic error induced by the light refraction. The droplet internal

convective mechanisms were investigated with continuous measurements of flow distributions inside the evaporating droplets in upward air stream at different temperature.

In chapter 4, temperature and flow distributions were measured continuously inside the pendant water droplets evaporating in upward air stream to investigate the droplets heat and mass exchange phenomena. The experimental results were compared with the calculations using the widely-used correlations for droplet heat and mass transfer, and the adequacy of the correlations was discussed.

All in all, the final objective of this work is to investigate the mechanisms of heat and mass transfer between spray droplets and surrounding gas during the containment spray cooling by detailed temperature and flow measurements inside droplets. Currently in this paper, the development of the measurement technique and the experimental investigation of the droplet evaporation behavior in air stream with this technique are the main missions.

2. Simultaneous velocity and temperature measurements technique

In this study, an ex-situ calibration method was developed to employ phosphorescence thermometry for the investigation of heat and mass transfer in small-scale geometries such as the one inside evaporating pendant water droplets, and the effect of local noise was discussed and quantified [31]. Europium (III) thenoyltrifluoroacetonate (EuTTA)-dyed particles were adopted as tracers for the PIV and temperature measurement. The developed calibration and measurement technique exhibited high accuracy and temperature sensitivity and could be applied to various measurement geometries. Hence, we conclude that it could be used for further investigations on the heat and mass transfer inside a pendant droplet located in an upward air stream.

2.1. Experimental setup

2.1.1. Optical apparatus and imaging system

Figure 2-1 shows a schematic view of the experimental setup used for PIV-TSP calibration and measurement. The correlation between the phosphorescence light intensity decay rate and temperature is related to various factors such as the type of the applied fluid and sensitivity of the high-speed camera. Calibration experiments and data analysis were performed to quantify this correlation.
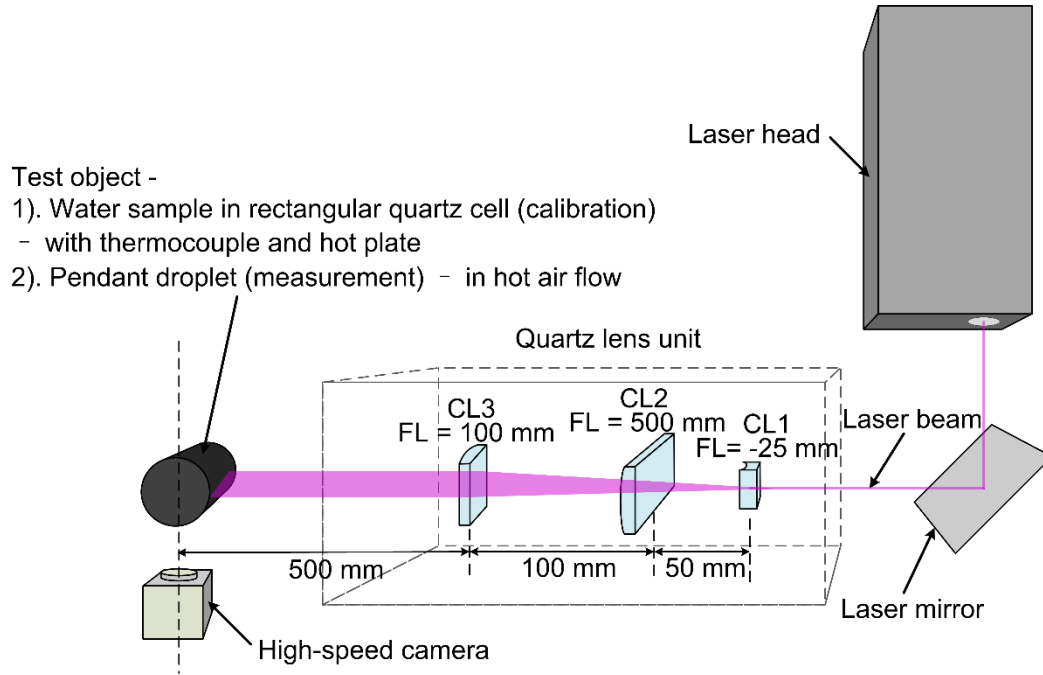
Figure 2-1. Schematic view of PIV-TSP system

Tracer particles were excited by a pulsed ultraviolet (UV) laser sheet of 355-nm wavelength. The laser system used in this study was a Nano-PIV Series laser (LPU1000) manufactured by Litron Lasers. This double-head laser system can generate pairs of laser pulses separated by 1 ms at a maximum repetition rate of 100 Hz. The pulse duration of the laser was 4 ns, and the pulse energy was 15 mJ.

A CMOS high-speed camera (Photron FASTCAM Mini AX200 900K-M-16GB) was used to record the time-series phosphorescence decay images. The camera was fitted with a Leica Z16 APO zoom macroscope (16:1, 3.2×) and a 1× plan-apochromatic objective (working distance: 97 mm). The camera recording speed was 20,000 fps, and the image resolution was 640×480 pixel. The camera was located in front of the test object, and the photographic direction was at a right angle to the laser sheet.
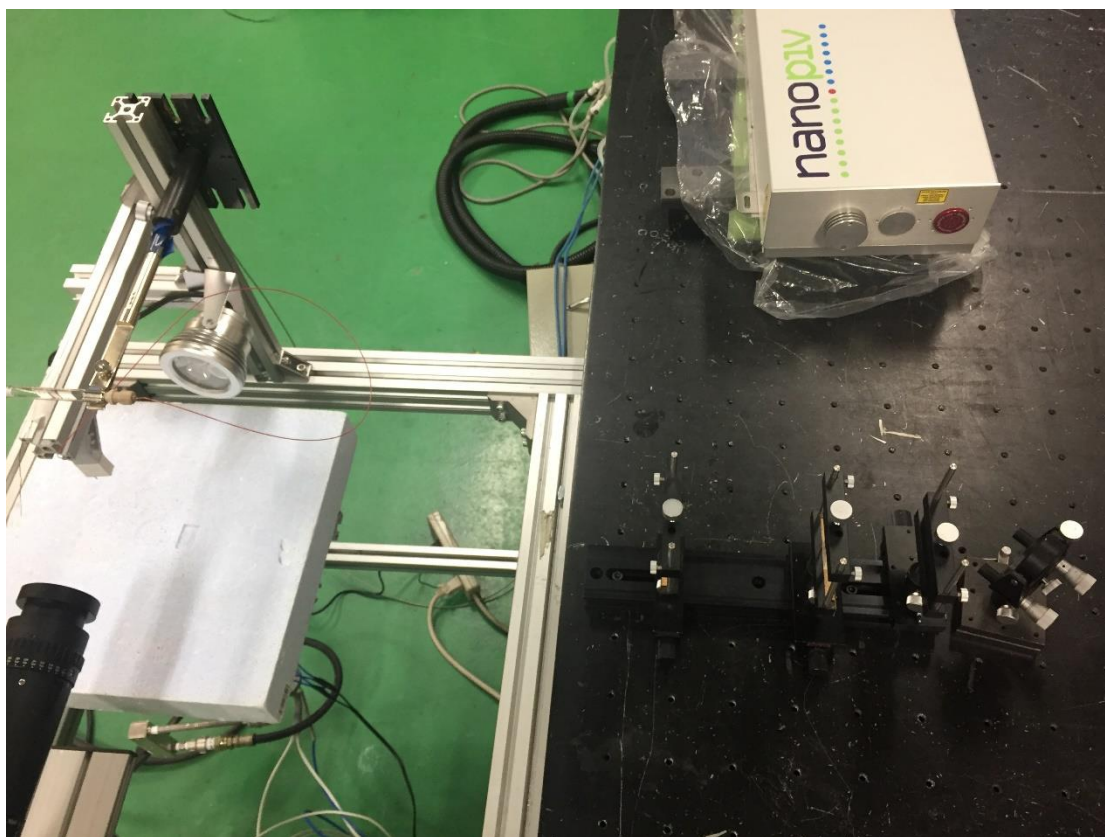
Figure 2-2. Photo of the experiment apparatus

Figure 2-2 gives a photo of the experiment apparatus. The generated laser sheet was focused in a direction perpendicular to the axis of the lens unit and target and was reflected by a high-energy Nd:YAG laser mirror with high reflectivity (>98.5%–99.5%) at the 355-nm wavelength for a 45° angle of incidence. An elliptical laser beam was shaped into a 1-mm thick laser sheet using a lens unit consisting of three cylindrical quartz lenses, and centered at the quartz cell or water droplet. The combination of the FL = −25 mm and the FL = 100 mm cylindrical lenses produces an approximately 10 mm tall non-diverging laser sheet. And the FL = 500 mm cylindrical lens reduced the thickness of the light sheet. Minimum energy loss and good laser-sheet stability were ensured by using optical instruments made of quartz with good UV light transmission and high temperature stability. The arrangement of the lens unit can be observed from the photo, and can be adjusted on the railway shown in Figure 2-2.

2.1.2.Experimental equipment and temperature-sensitive particles

To determine the effect of local intensity differences on the phosphorescence decay rate and obtain high-accuracy calibration, an ex-situ calibration method was developed. Ex-situ means that different test section from the measurement target was used for calibration experiments.

In this study, calibration experiments were performed in a rectangular quartz cell to obtain the relationship between the phosphorescence intensity decay constant and local fluid temperature (Figure 2-3).
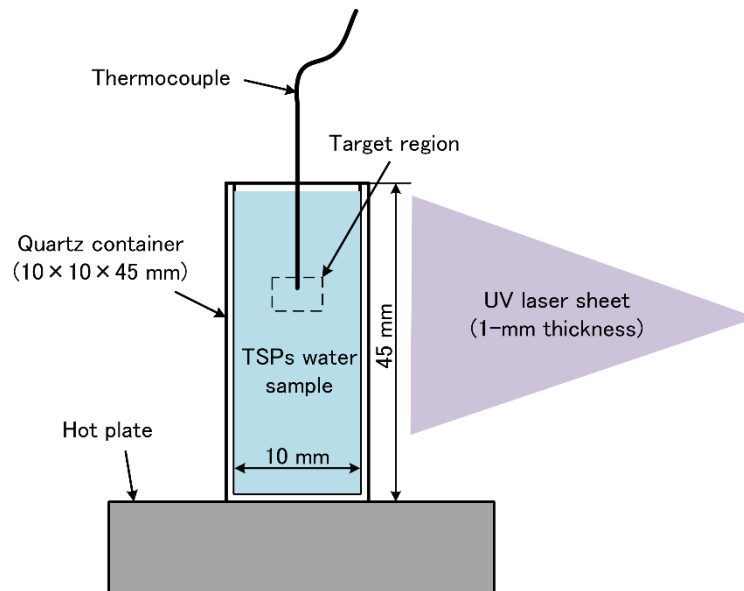
Figure 2-3. Test section for calibration

The size of this region was so small (approximately 3×4 mm) that no significant temperature gradients existed in it and the temperature distribution inside the target region recorded by the high-speed camera was assumed uniform; this was also confirmed during the tests. A hot plate was used to heat the cell from the bottom and thereby set different temperatures ranging from room temperature (approximately

20 °C) to 80 °C. A thermocouple was installed in the area to be photographed inside the water sample to record the corresponding temperature.
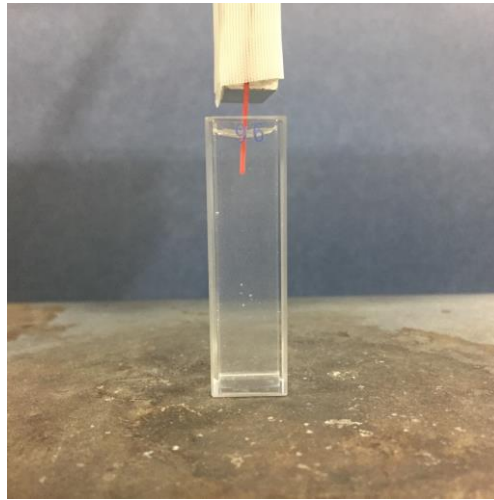
Figure 2-4. Photo of the test section for calibration

Figure 2-4 gives a photo of the rectangular quartz container used for calibration experiments filled with water sample, located on the hot plate. The calibration error was the difference between the temperature measured by the thermocouple and that calculated using TSP analysis.
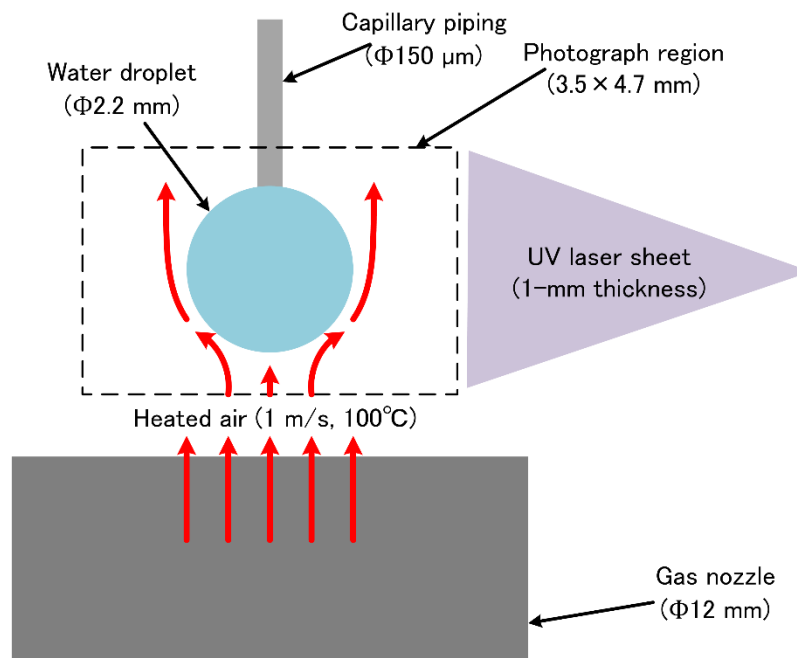
Figure 2-5. Measurement target

The calibration results were applied to the pendant water droplets. The diameter of the droplet was controlled to be approximately 2 mm using a micro-syringe. As shown in Figure 2-5, the investigated droplet was placed in an upward air stream. A hot airstream with 1 m/s flow velocity was generated using an air compressor having a buffer tank. The air temperature was controlled using a heater having an on-off switch. The temperature distribution and velocity field inside the evaporating droplet were measured.

The measurement areas were approximately 2-mm-diameter vertical sections of the water droplet and a (3×4)-mm rectangular target region in the quartz container. As mentioned previously, similar investigations have already been conducted in silicone oil [27]. In this study, similar sphere particles were used in water. Ion-exchanged spheres (MCI GEL, Mitsubishi Chemical Co.) with a mean diameter of 10 μm were used as tracer particles. To prepare the dye solution, plenty of EuTTA (100.0 mg) was dissolved in ethanol (20.0 ml). The particles were dyed by soaking in the solution, and dried gradually at 60 °C for approximately 6 hours. Considering the effects of particle precipitation, particle agglomeration, and phosphor material elution by water, the water containing the particles stay in a condition suitable for PIV-TSP measurements for approximately half an hour after an ultrasonic treatment.

2.1.3.Signal control
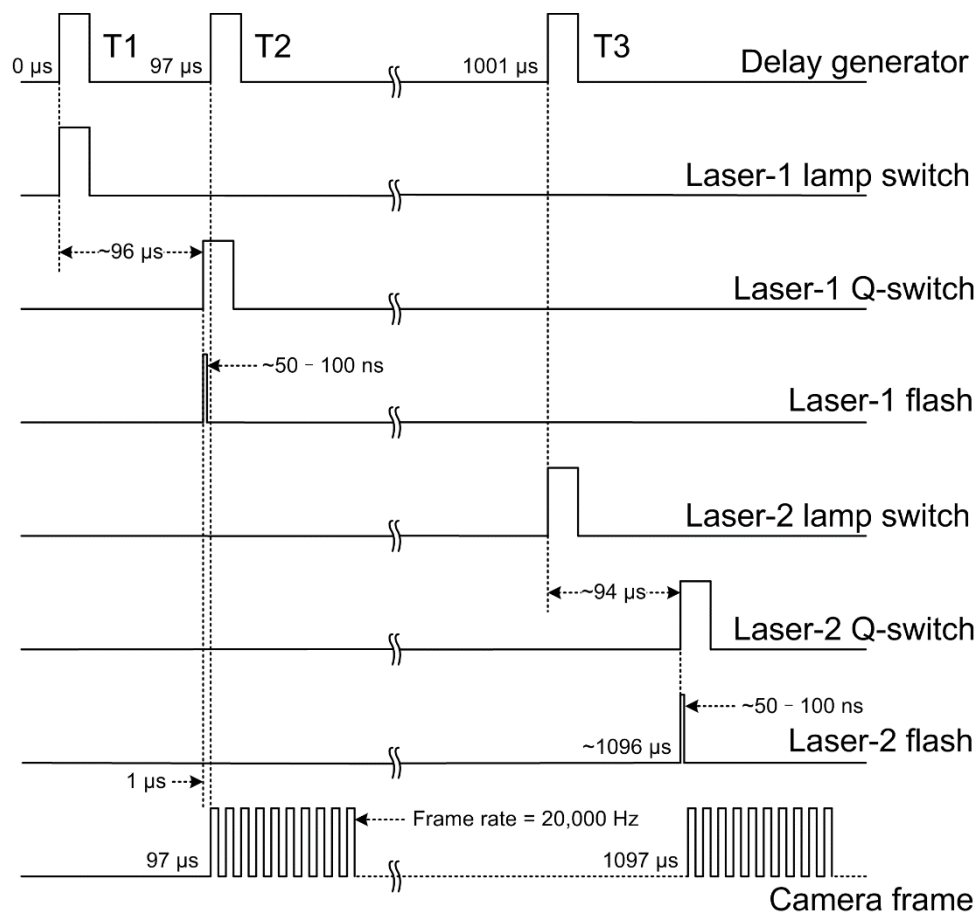
Figure 2-6. Timing chart for signal control

Phosphorescence decay images were recorded under low-room-lighting conditions to reduce background noise. The exposure time of each frame was 50 μs, and seven of these images were used for TSP image processing. A delay pulse generator (Quantum Composers 9614+) was used to control the laser and high-speed camera according to the timing chart shown in Figure 2-6.
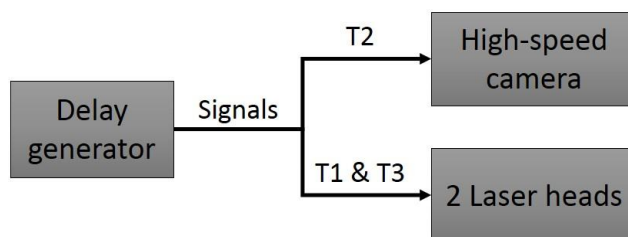
Figure 2-7. Signal transmission

The signals T1 and T3 were given to laser-1 and laser-2 respectively, while the signal T2 was given to the high-speed-camera, as shown in Figure 2-7. Considering the default optimum delay between the lamp switch and Q-switch, different delays were introduced to ensure that the first image of the phosphorescence decay was recorded 1 μs after the generation of the excitation laser pulse. These delays were introduced to avoid the noise caused by reflection or momentary fluorescence emitted from materials other than EuTTA. Under this signal control, two excitation laser pulse occurred with a time interval of 1 ms, and the exposure of the first frame of each decay occurred 1 μs after them. Sequences of decay images were used for phosphorescence decay analysis, while two images straight after adjacent laser flashes were used for PIV analysis.

2.2. Ex-situ Calibration

2.2.1. Calibration experiment

The TSP temperature is measured by calculating the exponential decay rate constant of EuTTA phosphorescence (visible light, peak emission wavelength 612 nm) under UV laser excitation from a sequence of decay images. The lifetime of the decay is approximately several hundred microseconds in the temperature range from room temperature (approximately 20 °C) to 80 °C; the lifetime shortens as the temperature rises. For temperature calculation, it is necessary to obtain the correlation curve between the decay constant and temperature. For the water sample containing TSPs in the rectangular quartz cell ($10 \times 10 \times 45$ mm), decay images were recorded by performing experiments at different temperatures and particle densities for calibration. Figure 2-8 shows the sequence of decay images recorded at 23.3 °C and 58.3 °C. To avoid a decrease in the laser intensity along the horizontal axis in the target field, the particle density was set to an optimum level.

Decay images at 23.3°C

Decay images at 58.3°C
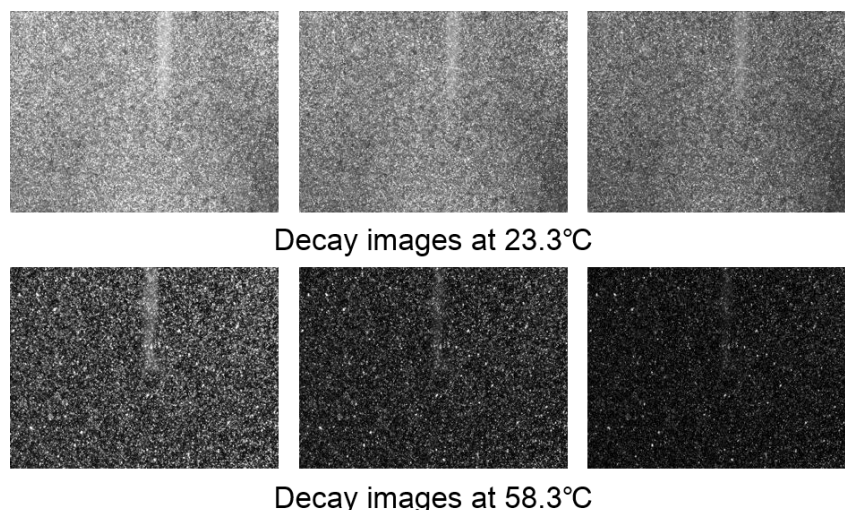
Figure 2-8. Sequential decay images recorded inside the water sample at 23.3 °C and 58.3 °C

The sequential phosphorescence decay images were recorded while the water temperature was changed at intervals of approximately 5 °C. The mean decay constant was calculated from the sequential decay images obtained under laser flashes. The temperature measured by the thermocouple was used to obtain the relationship between liquid temperature T and phosphorescence decay constant τ.

As above-mentioned, phosphorescence decay images were recorded with the water temperature changing at intervals of about 5°C from room temperature (approximately 20°C) to 80°C. Using sequences of decay images, local intensity exponential decay constant was computed spatially by image processing and analysis. The monochrome images were recorded in PNG format of 16 bits high quality (640×480 pixels in size), which means that the intensity of pixels is in the range of 0-65,535. During calibration, the computational procedure was conducted in each interrogation window of 32×32 pixels.

Exponential decay constants were computed for each interrogation window by image processing and analysis. First, the intensity data of pixels were read from the sequential decay images of one laser flash. The background noise induced by the ambient light was reduced by subtracting the background image recorded just before

the laser flash from the decay image. Second, the relative value of the window phosphorescence intensity was calculated, and then, the exponential decay rate of the phosphorescence intensity was obtained using least squares fitting for each interrogation window.

2.2.2.Calibration method

The decay constant was calculated for each interrogation window as follows.

1) Phosphorescence intensity in each interrogation window

The group of pixel intensity values for all 1,024 pixels in each interrogation window was found compliant with a lognormal distribution. Figure 2-9 shows two examples of the distributions of pixel values in the interrogation window.
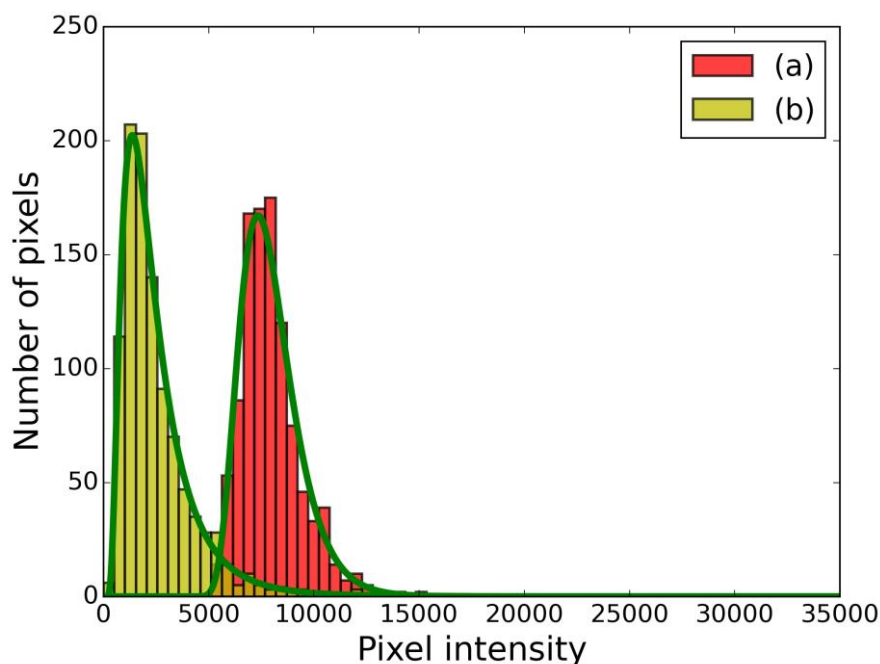
Figure 2-9. Two examples of the log-normal distribution fitting data of pixel values in the interrogation window. The distribution of pixel values in an interrogation window in the phosphorescence emission image obtained at 45.8 °C, at a high-particle-density condition (a), mean value 7960, geometric standard deviation 0.35 and a low-particle-density condition (b), mean value 2531, geometric standard deviation 0.91.

The mean value of the distribution was adopted as the phosphorescence intensity in each interrogation window to reduce the influence of fluctuations in the maximum intensity values. The results (phosphorescence decay constant) obtained by using the mean value of the lognormal distribution and the arithmetic mean of all the pixel intensities were quite similar for the high intensity cases. However, when the pixel values in the phosphorescence emission images were low, the method using the mean value of the lognormal distribution provided a more robust estimate compared to that obtained using the arithmetic mean.
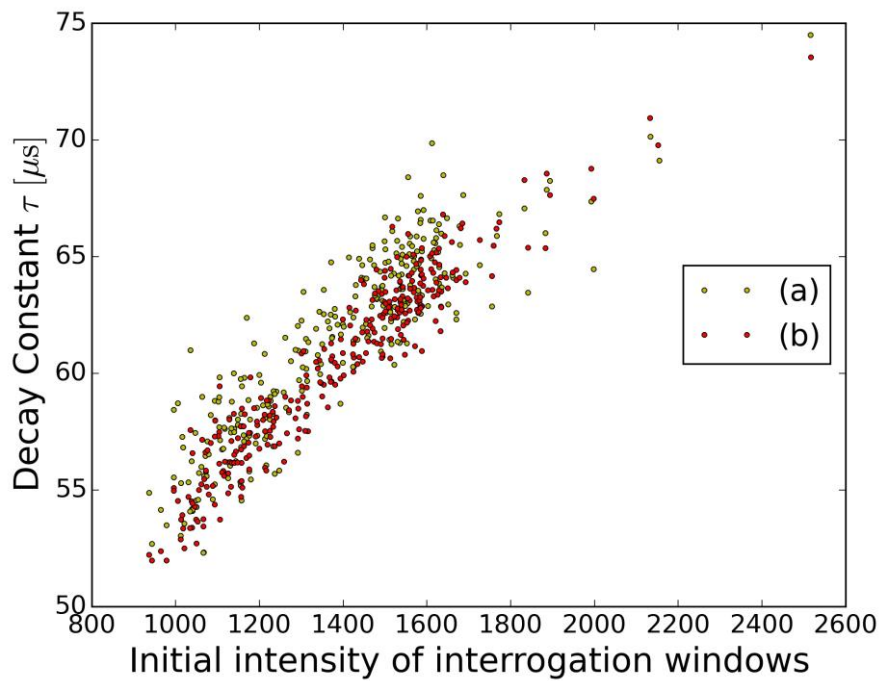
Figure 2-10. A comparison of the intensity decay constant data obtained in each interrogation window at a low intensity case by using two methods. (a) Using the summation of all the pixel intensities as the phosphorescence intensity in each interrogation window and (b) using the mean value of the log-normal distribution as the phosphorescence intensity in each interrogation window.

Figure 2-10 shows a comparison of the results obtained using this method with the data calculation results obtained by simply considering the arithmetic mean of all the pixel intensities as the phosphorescence intensity in each interrogation window. As seen, in the case of using the simple arithmetic mean, decay constants are overly scattered,

while dispersion of the decay constant values for an initial intensity is reduced for the lognormal case. The method of calculating the phosphorescence decay constant in each interrogation window will be introduced later in this section. Figure 2-10 also shows that the initial intensity of the interrogation window may affect the phosphorescence decay constant in this window. This effect will be discussed in section 2.2.3.

Another method is to use the summation of some maximum values of the pixel intensity in the interrogation windows, represent the emission of particles. This method provides similar results as the method using the mean value of the lognormal distribution. However, it even takes more time than the lognormal distribution method.

The scale parameter (geometric standard deviation) of the lognormal distribution in each window also indicates the local data quality. As shown in Figure 2-9, for the low-particle-density condition, the geometric standard deviation of the distribution was 0.91, which is larger than the geometric standard deviation at the high-particle-density condition (0.35). The large geometric standard deviation indicated that the pixel values were spread out in the interrogation window, and the possible deviation induced by fluctuations in the intensity values may be large. As an example, the decay constants of phosphorescence at 45.8 °C obtained from the high-particle-density condition (Figure 2-9(a)) and the low-particle-density condition (Figure 2-9(b)) are given in section 2.3.1, and smaller data deviation were obtained from the interrogation windows with smaller scale parameters of its pixel value distributions.

This method using the mean value of the lognormal distribution can be effective to obtain a good measurements accuracy of low intensity decay images. However, it takes longer time for the computations of image processing than the method using the arithmetic mean. These two methods should be evaluated carefully to choose one of them during the data analysis.

2) Phosphorescence intensity in each interrogation window

The phosphorescence intensity variation with time was evaluated in terms of relative logarithmic values. The momentary phosphorescence intensity is given by Eq. 2-1:

$$I_t = I_0 e^{-\frac{t}{\tau}} \tag{2-1}$$

In Eq. 2-1 I_0 is the initial intensity obtained from the first image and τ is the decay constant. To estimate the decay constant according to this equation, the relative logarithm values $\ln(I_t/I_0)$ were plotted using the decay image number as the x-coordinate.
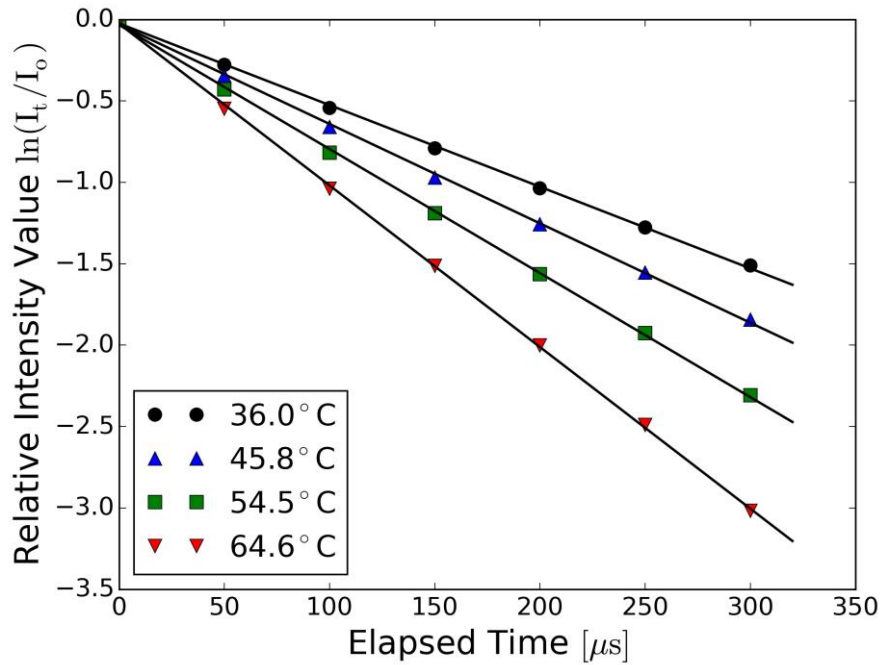
Figure 2-11. Relationship between time and relative value of phosphorescence

Consequently, the intensity value for frame 0 (the first frame) is a constant value of 0, and then, the intensity linearly decreases and takes negative values. Considering the exposure time of each frame, the relative intensity value and elapsed time were fitted by the least-squares method, and the decay constant τ was determined from the linear slope for each interrogation window. The aforementioned calculation process was found to be reliable when the correlation coefficient of the data fitting in Figure 8 was greater than 0.999. At high temperatures, a minimum of five images were used in the

31

computation. The relationship between the relative intensity value and elapsed time in a chosen interrogation window at the image center is shown in Figure 2-11 for several recorded temperatures. As seen, the decay curves exhibit a good linear tendency.
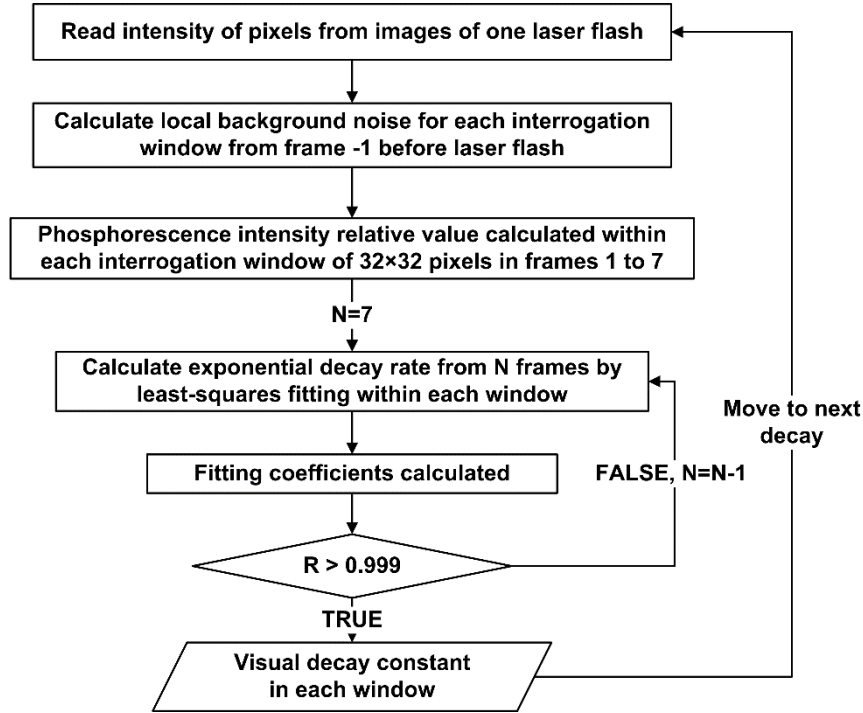
Figure 2-12. Computation flow chart of phosphorescence decay constant

The above computational process was repetitively carried out in each interrogation window to obtain the distribution of decay constants for different temperature conditions. The computation flow chart is shown in Figure 2-12.

2.2.3. Initial intensity effect

The local decay constant obtained from each interrogation window appeared to be location dependent, which was attributed to the local fluid condition and presence of optical noise. One solution to eliminate this discrepancy is to calibrate the correlation curve between the decay constant and temperature locally [27]. However, this method applies only to in-situ conditions where the calibration setup is identical to the test setup. When the ex-situ calibration method is used to measure temperature and velocity in

small scales for cases where thermocouple intrusion is not possible, such as in a droplet, the location discrepancy needs to be understood and quantified.

In the decay images recorded by the high-speed camera, the deviations between different locations were represented by the pixel intensity differences. Therefore, the phosphorescence intensity in each interrogation window obtained from the first frame of decay, denoted as the window initial intensity (WII), was investigated together with the discrepancy in the calculated decay constant.
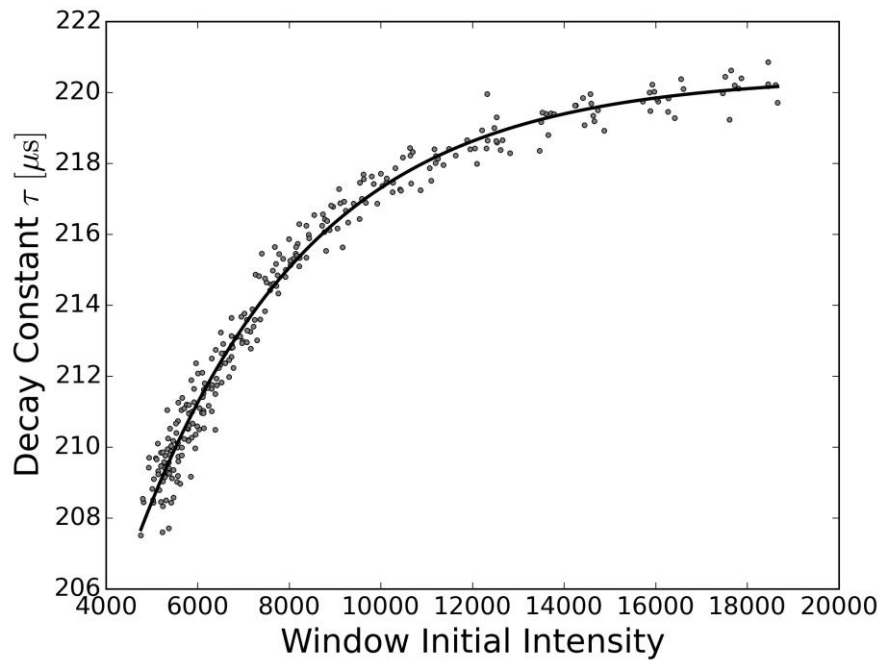
Figure 2-13. WII-varying window decay constant obtained from one image sequence at room temperature (approximately 20 °C)

The results of the decay constant computation showed good regularity, which indicated that the WII affected the local decay constant as the coefficient of a half sigmoid function, as shown in Figure 2-13. In windows with a high WII (greater than 10,000), the intensity difference had no major effect on the decay constant, whereas in windows with a lower WII, the local decay constant appeared to be smaller, in other words, a more rapid decay occurred. In high-particle-density situations, for a wide range of WIIs, the relationship between the local decay constant and WII could be understood

more distinctly from the scatter diagram, and the correlation functions were obtained by utilizing the least-squares method with high curve-fitting coefficients. Figure 2-13 gives the scatter diagram of WII-varying local decay constants calculated from a sequence of decay images at approximately 20 °C and the fitting correlation curve in the form of the positive part of a hyperbolic tangent function.

The WII of decay varied with the local particle density, laser illumination power, and water temperature. At a lower WII condition, the phosphorescence emission decayed faster in images, and the degree of linearity of the decay lines became worse. In the calibration experiments that were conducted, we found that the WII effect (the WII coefficient function) did not change markedly with difference in the laser illumination power or the particle density. However, the WII coefficient function changed significantly with change in the camera settings (e.g. magnification, position, frame rate, image resolution).
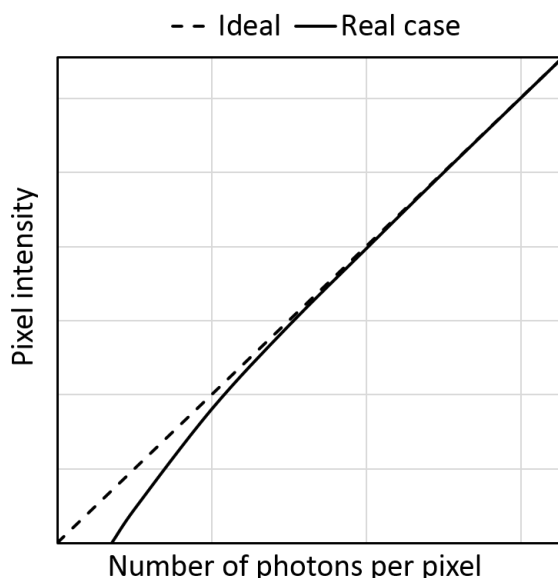
Figure 2-14. The discrepancy between pixel intensity in images recorded by the high-speed camera and light intensity (number of photons per pixel)

According to our observations, a possible reason for this WII effect could be a systematic discrepancy between the pixel intensity in images and the light intensity (number of photons per pixel) in the high-speed CMOS camera. This discrepancy

becomes more significant when the camera operates at a low light intensity, as qualitatively demonstrated in Figure 2-14.

It should be noticed that Figure 2-14 is not a quantitative graph, but just a graph to demonstrate the possible source of the systematic error. It is difficult to obtain the accurate curve of this camera issue because it is not possible for us to obtain the number of photons per pixel, and the degree of linearity of the decay lines became worse at low pixel intensities. Besides, the accurate function of this curve is not necessary for the measurements. Therefore we just gave a general curve to demonstrate this discrepancy as a possible reason of the WII effect.

The low light intensity is often the case in PIV-TSP measurements because of the phosphorescence decay (e.g. 5,000 is less than 10% of maximum pixel intensity in 16 bits). Therefore, the WII effect becomes significant and should be quantified during TSP calibration and analysis; recalibration of the WII effect is necessary when the camera settings have been changed. Especially when this measurement technique is applied for droplet measurements, since the optical distortion occurred when the lights pass through the curved surface of droplets may induce an intensity change or changes in the distributions of pixel intensity values in the interrogation windows.

During the experiments, the decay images in different WII ranges were recorded under multiple temperature conditions. By considering temperature to be the primary factor affecting the phosphorescence decay constant, the WII effect was estimated independently from the temperature effect in this study. Verification tests under different particle density conditions were additionally performed at a constant temperature; the results of these tests indicated a WII effect similar to that caused by temperature differences.

$$\tau_i = K_{II} \cdot \tau_o \qquad (2\text{-}2)$$

$$K_{II} = K_{II}(I_0) = \tanh(a + bI_0) \qquad (2\text{-}3)$$

In the above equations, K_{II} is the WII coefficient introduced to evaluate the WII effect as an influence coefficient, and it is a function of the WII I_0; τ_i is the detected decay constant obtained from recorded decay images by image processing; and τ_o is the phosphorescence decay constant correlated to the phosphorescence energy state transition.
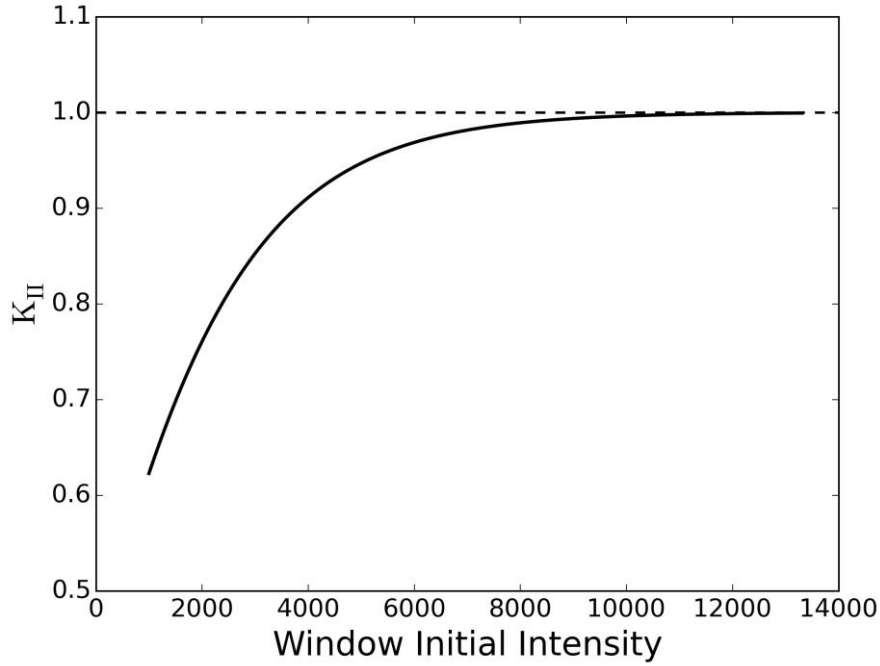
Figure 2-15. WII coefficient (K_{II})

By scaling the decay constant data obtained under different temperature conditions along with the corresponding WII of phosphorescence decay, the WII coefficient function $K_{II}(I_0)$ was obtained by least squares fitting in the form of the positive part of a hyperbolic tangent function as shown in Eq. 2-3. The obtained function curve is shown in Figure 2-15, in which the constants a and b were calculated to be 0.463 and 2.679×10^{-4}, respectively.

2.2.4. Calibration results

In principle, luminescence-lifetime-based temperature measurements can be estimated according to the Arrhenius equation [32, 33], which is concisely expressed by Eq. 2-4.

$$k_r = Ae^{-E_a/(R_g T)} \tag{2-4}$$

$$\ln\left(1/\tau_o\right) = a + b\left(1/T\right) \tag{2-5}$$

Eq. 2-4 gives the relationship between the chemical reaction rate constant k_r and absolute temperature T (in kelvin). In this equation, A is the pre-exponential factor, E_a is the activation energy, and R_g is the universal gas constant. In this study, the phosphorescence decay constant τ_o of phosphorescence decay is linearly related to the inverse value of the decay constant. Therefore, as shown in Eq. 2-5, $\ln\left(1/\tau_o\right)$ is considered linearly associated with the inverse value of the local absolute temperature.

As described previously, τ_o can be determined from the calculated detected decay constant and corresponding WII coefficient from each interrogation window. Accordingly, by analyzing a sequence of decay images used for calibration, τ_o was computed from a large number of windows. By using the testing temperature, the arithmetic mean value of the obtained τ_o was considered in the evaluation of the relationship between the temperature and decay constant.

The standard deviations of these decay constants may serve as an indicator of the calibration accuracy. The phosphorescence decay constant, τ_o, was 163.9 ± 2.9 μs at 45.8 °C with an average WII of 2,633 for all the interrogation windows (low-particle-density condition) and 165.8 ± 0.6 μs at 45.8 °C with an average WII of 7,480 for all the interrogation windows (high-particle-density condition). Therefore, good data coherence was obtained between different particle densities when the WII was in an appropriate range not less than 1,500. The results also indicated that as the WII became

larger, better calibration accuracy was achieved. Because decay occurred faster at higher temperatures (lower WII), an increase in temperature also induced a larger calibration error. This indicated that the TSP method had a higher accuracy at lower temperature ranges than at higher temperature ranges.

The sequences of decay images recorded under the high-particle-density condition were used to calculate τ_o at various temperatures; τ_o was found to be 200.4 ± 0.8 μs at 36.0 °C (mean WII: 10,767), 136.1 ± 0.9 μs at 54.5 °C (mean WII: 5,560), and 103.8 ± 1.8 μs at 74.1 °C (mean WII: 1,600). The correlation between the temperature and decay constant is shown in Figure 2-16.
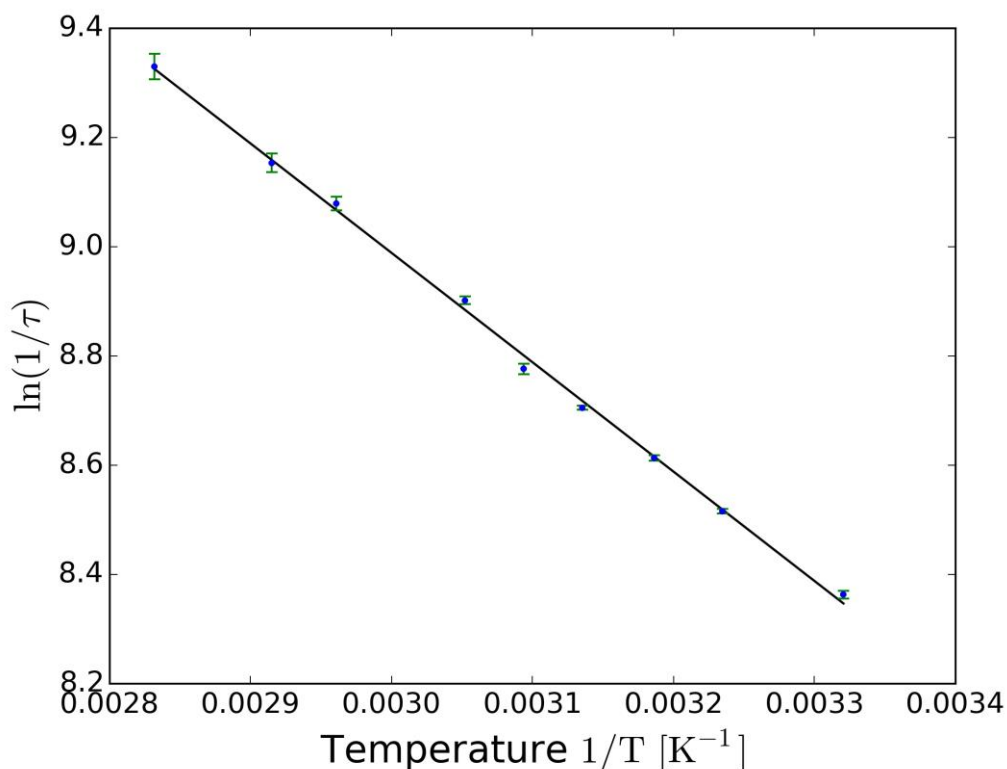
Figure 2-16. Relationship between temperature and τ_o

A comparison of the obtained result with the result obtained in silicone oil (where the decay constant was 217 μs at 49.0 °C) indicated that the phosphorescence decay was faster for the TSPs in water [27]. The difference in the detected decay constant could be greater because the ex-situ calibration method considers the initial intensity effect.

This TSP calibration results can be used together with PIV analysis using the signal control mentioned above in section 2.1.3. In this study, during measurements, the local liquid temperature was obtained in the interrogation windows (16 × 16) pixel during image possessing, and for this window size, the spatial resolution of the measurement was approximately 0.12 mm. A higher resolution can be achieved by TSP analysis using smaller interrogation windows or windows that partly overlap with each other. The size of interrogation windows for PIV analysis was 32 × 32 pixel with 50% overlap. Since interrogation windows of size 16 × 16 pixel were used during TSP analysis, the temperature and velocity distributions can be obtained inside the droplets with the same spatial resolution. A minimum threshold for the correlation was added into the PIV calculation procedure for higher accuracy. Data with correlation coefficient less than 0.5 were eliminated and then recalculated using linear interpolation of four adjacent vectors.

2.3. Discussions

2.3.1. Effectiveness of ex-situ method

The local water temperature can be measured by using the obtained T-τ_o correlation function. The in-situ calibration method is used to calculate the temperature directly from the detected decay constant by utilizing the T-τ correlation function. In the case of the ex-situ calibration that considers the WII effect, the phosphorescence decay constant is obtained first from the detected decay constant together with the WII, and then, the temperature is calculated from the constant. With regard to the experimental calibration data, the temperature in each interrogation window in the target region can also be inversely calculated using the obtained detected decay constant by this method.

Figure 2-17 shows a comparison of the inversely calculated temperature distributions in all the interrogation windows of the calibration target region at 45.8 °C using in-situ (a) and ex-situ (c) calibration methods together with the phosphorescence

emission image. The particle phosphorescence image (b) clearly shows that the phosphorescence intensity decreases from the right side to the left for different local laser powers caused by the absorption of high-density particles. A comparison of the temperature distributions in (a) and (c) shows that the intensity difference causes artificial spatial differences in the temperature distribution obtained by the in-situ calibration method and that no such differences appear in the result calculated using the proposed ex-situ method. The temperature distribution obtained using the ex-situ method (c) also shows less calibration error with a smaller deviation.

(a) In-situ calibration method, 45.2 ± 0.37 °C

(b) Phosphorescence emission

(c) Ex-situ calibration method, 45.4 ± 0.19 °C
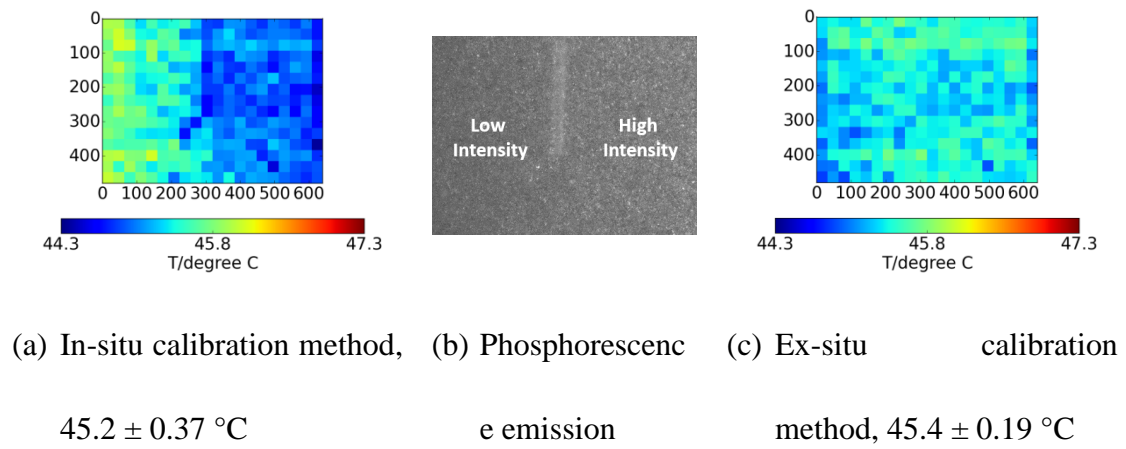
Figure 2-17. Inversely calculated temperature distribution at 45.8 °C using in-situ and ex-situ calibration methods along with phosphorescence emission image

At 45.8 °C, the arithmetic mean value of the measured temperature obtained using the ex-situ calibration method was 45.4 °C. According to the definition of the measurement error given in Section 2, the TSP measurement error was 0.4 °C and the standard deviation was ±0.19 °C because the water temperature measured by the thermocouple was 45.8 °C. The inversely calculated temperature maps indicated that the error became larger as the temperature increased, and as an example, the error was 0.9 °C with a standard deviation of ±1.03 °C at 69.9 °C. Considering the accuracy of the thermocouple used for the water temperature measurement, the error in the TSP calibration results was within the acceptable range.

Figure 2-17 shows that the TSP analysis performed using the ex-situ calibration method is free from errors induced by local optical noise caused by the non-uniformity of the varying laser power and particle density. The improved ex-situ calibration method can also be applied to various measurement fields having different geometries.

2.3.2. Advantages and limitations

In previous sections, the methodology and results of 2-D liquid temperature and velocity measurements using PIV-TSP analysis were described. Images obtained using a high-speed camera indicated that the use of TSP with EuTTA provided high temperature and time sensitivity, high spatial resolution, and high accuracy of transient measurements. This measurement technique using the ex-situ calibration method can be effective for investigations on fluid heat and mass transfer. Temperature-sensitive particles could be used with various working fluids such as gas, water, organic fuels, and possibly cryogenic fluids, and different phosphorescence materials could be developed for various temperature regions.

It should be noted that if this technique was used to measure the liquid temperature and velocity through a curved gas-liquid interface, such as the internal temperature and flow of a water droplet, the light refraction and reflection occurred through the curved surface may cause image intensity change and distortion. The noise caused by reflection or momentary fluorescence emitted from materials other than EuTTA has been avoid by the signal control. Using the ex-situ calibration method with the WII effect, the laser intensity variation before the excitation induced by the light refraction and reflection has already been considered. Because we considered that the WII effect was caused by the camera issue (see Figure 2-14), the intensity variation within the droplet due to the lensing effect may not induce systematic error on the temperature measurements as well. The image distortion can induce changes in temperature and flow distributions on the image plane, which should be taken into consideration. In this study, an anti-distortion algorithm was added into the PIV-TSP analysis procedure to correct the coordinate

displacement caused by distortion and to obtain the velocity distribution on the object plane. This algorithm will be introduced in section 3.1.2.

In this study, 5–7 images were used in the phosphorescence decay computation, and this number could be varied with different camera frame rates and image quality. Measurements of the spatial resolution could also be adjusted by changing the size of the interrogation windows and by using overlapping windows. It should be noted that these adjustments in the calculation might affect the accuracy of measurements. The intensity of the decay images are related to the light sensitivity of the high-speed camera. Therefore, the re-calibration of the WII effect and T-τ_o correlation might be necessary to obtain an acceptable measurement accuracy for each camera.

1) Simultaneity of temperature and velocity measurements

Simultaneous temperature and velocity measurements can be realized using the TSP method combined with PIV analysis. Because decay images recorded at 20,000 fps were used for image processing, the simultaneity and dependability of TSP and PIV can be discussed as follows. Two images obtained directly after adjacent flashes separated at 20 frames were used for the PIV analysis. The results showed that the window displacement was less than 20 pixels in the entire target region; therefore, the displacement of the particles did not cause any interference in the TSP analysis. Images were recorded in the order of milliseconds, which ensured the simultaneity of the transient temperature and velocity measurements for general fluid phenomena.

2) WII effect

For simplifying the analysis, the WII effect was assumed independent of the fluid temperature in this study. Although the results showed good regularity with small errors, this assumption might have created some discrepancies. Another method to handle the WII effect is shown in Figure 2-13, wherein a WII-invariant decay constant is computed for each sequence of decay images during curve fitting without assuming that the WII effect is independent of the varying temperature. However, the origin phosphorescence

decay constant becomes incalculable in the temperature computation procedure. Nevertheless, this method will be a good approach to understand the WII effect in detail in further research.

3) Brownian motion of TSP

The Brownian motion of the applied 10 μm temperature-sensitive particles can be easily calculated according to the theory of the Brownian movement [34].

$$\overline{(\Delta x)^2} = 2Dt \tag{2-6}$$

$$D = \frac{k_B T}{6\pi\eta a} \tag{2-7}$$

Eq. 2-6 indicates the mean squared displacement $\overline{(\Delta x)^2}$ (MSD) in terms of the time elapsed t and the diffusivity. The diffusion constant D can be obtained according to Eq. 2-7, where k_B is the Boltzmann constant, T is the temperature, η is the viscosity of the liquid, and a the radius of the Brownian particles.

The obtained MSD of two adjacent decay images in this study was approximate $(3.82 \times 10^{-4} \ \mu m)^2$ at 20 °C and $(1.29 \times 10^{-3} \ \mu m)^2$ at 80 °C, roughly of only the order of 10^{-5} pixel. Therefore, the 10 μm particles Brownian motion will not affect the PIV-TSP measurements.

2.4. Conclusion of the chapter

In this study, a phosphorescence-decay-based simultaneous velocity and temperature measurement technique was investigated using a developed TSP analysis along with an ex-situ calibration method combined with PIV.

Calibration experiments have been conducted in a rectangular quartz container from room temperature (approximately 20 °C) to 80 °C, and the obtained decay images have been analyzed by image processing.

The calibration results showed that the initial intensity of phosphorescence decay, which varied with the local particle density and laser power, affected the local decay constant as the coefficient of a half sigmoid function. Considering this initial intensity effect, a correlation curve between the temperature and exponential decay constant was obtained by referring to the Arrhenius equation.

The calibration accuracy for the liquid temperature and particle density was ±0.4 °C and ±0.9 °C at 45.8 °C and 69.9 °C, respectively. The spatial resolution of the measurement was approximately 0.12 mm, which could be controlled by the size of the interrogation windows used during image possessing.

The proposed technique is expected to be useful in conducting investigations on the mechanisms of heat and mass transfers between droplets and carrier gases. Furthermore, it can potentially improve our understanding of the heat and mass exchange mechanisms within a droplet's internal flow structures and temperature gradients.

3. Droplet evaporation experiments method and droplet internal flow

3.1. Experimental equipment and method

The PIV-TSP method was used to measure the 2-D transient temperature distribution and velocity field inside a pendant water droplet evaporating in an upward stream of air. Figure 3-1 shows a sequence of phosphorescence decay images of the pendant droplet recorded at approximately 20 °C.
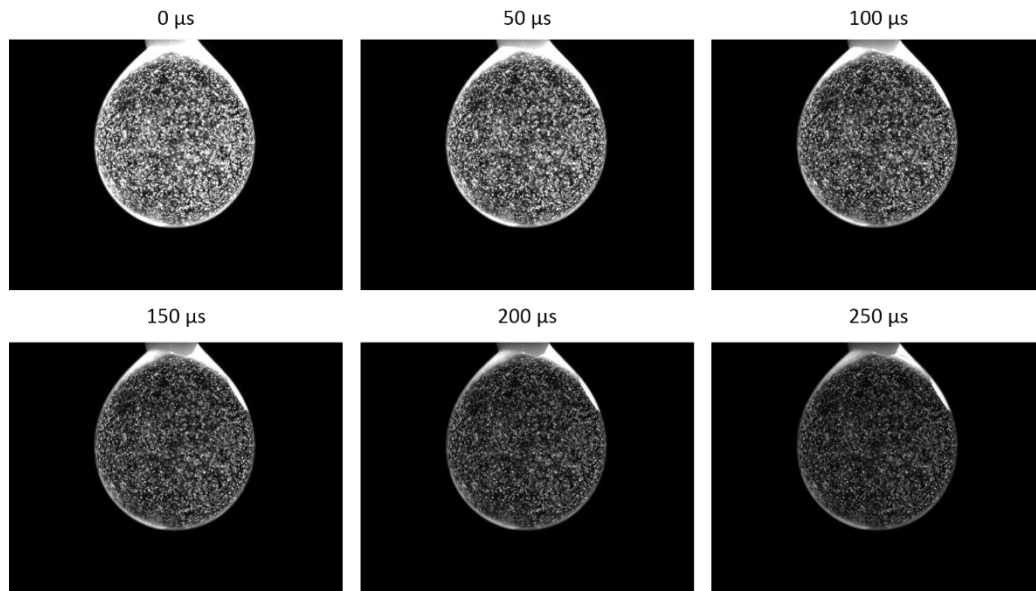
Figure 3-1. Sequence of phosphorescence decay images of the pendant droplet at room temperature (approximately 20 °C)

As mentioned above, the temperature distribution inside the pendant droplet was obtained by TSP analysis. For a higher spatial resolution of measurements, different from the (32×32) pixel interrogation windows used during calibration, the local liquid temperature was obtained in the interrogation windows (16×16) pixel during image possessing, and for this window size, the spatial resolution of the measurement was approximately 0.12 mm. A higher resolution can be achieved by TSP analysis using

45

smaller interrogation windows or windows that partly overlap with each other. The size of interrogation windows for PIV analysis was 32×32 pixel with 50% overlap. Since interrogation windows of size 16×16 pixel were used during TSP analysis, the temperature and velocity distributions can be obtained inside the droplets with the same spatial resolution. A minimum threshold for the correlation was added into the PIV calculation procedure for higher accuracy. Data with correlation coefficient less than 0.5 were eliminated and then recalculated using linear interpolation of four adjacent vectors.

3.1.1.Equipment for droplet evaporation experiment

The PIV-TSP system introduced in chapter 2 was used to investigate the droplet evaporation. During the droplet measurements, the test-section for calibration was replaced by the evaporating droplets. The equipment used to generate a pendant droplet as the measurement target has been briefly introduced in section 2.1.2.

1) **Measurement target**
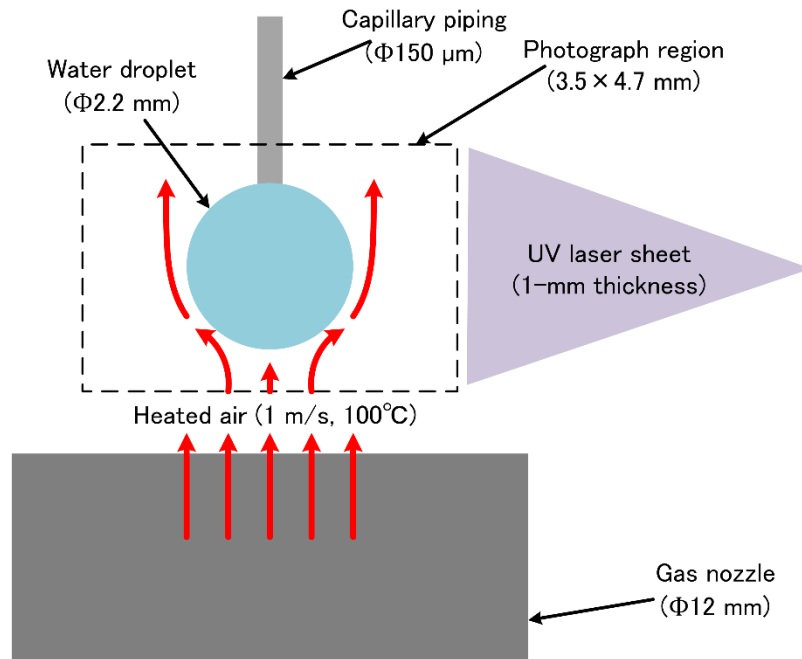
Figure 3-2. A pendant droplet as the Measurement target

The diameter of the droplet was controlled to be approximately 2 mm using a micro-syringe. As shown in Fig. 3-2, the investigated droplet was placed in an upwards air stream. The air stream was generated by an air compressor and heated by a heater with on-off control, and the air flow channel was controlled with an on-off electromagnetic valve. The terminal velocity of a 2 mm diameter free-falling water droplet in air is about 5 m/s. For droplet stability (small deformation and vibration), air stream velocity was 1 m/s in experiments.

Figure 3-3. Photo of a pendant droplet generated at the orifice of the capillary piping

Figure 3-3 gives a photo of a pendant droplet generated at the orifice of the capillary piping. The droplet was located just above the outlet of the air gas channel.

2) **Signal control**
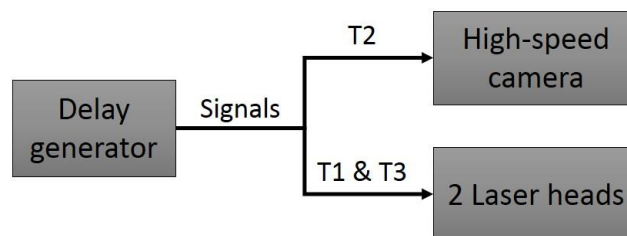
Figure 3-4. Signal transmission

In order to measure the temperature and flow distributions inside the water droplets continuously, the signals T1, T2 and T3 were given to the high-speed camera and the laser machine cyclically with a time period of 15 milliseconds or 20 milliseconds. The trigger mode of the high-speed camera was the RANDOM mode during the droplet evaporation experiments. The RANDOM mode is a recording mode where the camera records an event for a predetermined number of frames at every press on the REC button, which is useful to shoot any event that takes place intermittently, using a signal generator connected to the camera that sends out a trigger signal to the camera at every occurrence of the event [35]. With the timing chart for signal control introduced in section 2.1.3, the high-speed camera started to record decay images at 20,000 fps, 1 μs after the generation of the excitation laser pulse. Besides, two excitation laser pulse occurred with a time interval of 1 ms, so the first image of the phosphorescence decay excited by the second laser flash was the 21st image recorded. Therefore, the number of frames to record at every trigger was set to 40.

Under this signal control, continuous measurements can be implemented for the beginning of droplet evaporation after air stream started.

3.1.2. Optical distortion correction

The curved surface of the water droplets can act as a lens, and induce optical distortion inside the droplets by light refraction. Some algorithms have been reported for correcting this kind of distortion [36-38]. Figure 3-5 gives the droplet profile and the results of distortion applied to a regular grid [37].
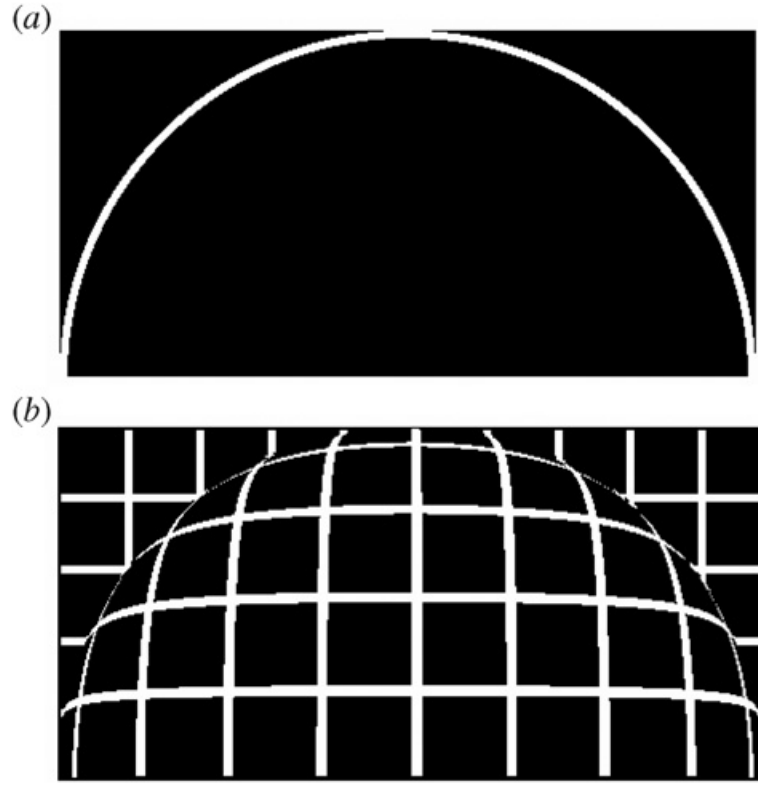
Figure 3-5. Droplet profile and the results of distortion applied to a regular grid [37]

In this study, an anti-distortion algorithm was added into the PIV-TSP analysis procedure to correct the coordinate displacement caused by distortion and to obtain the velocity distribution on the object plane using the velocity mapping method proposed by Kang et al. [36].
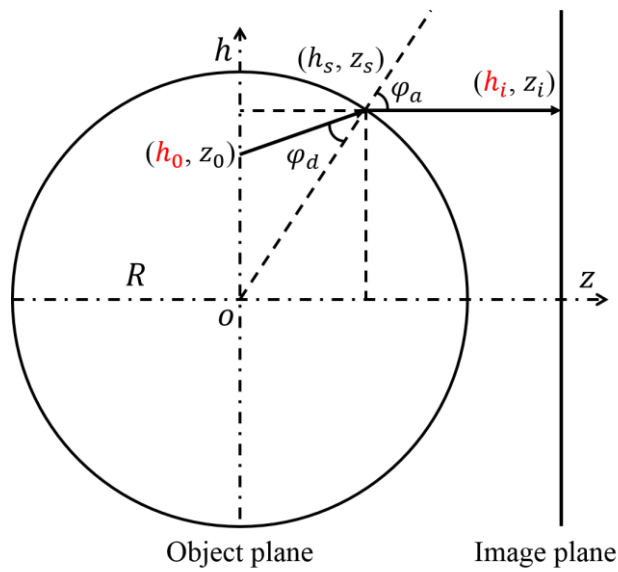
Figure 3-6. The radial distance change on the image plane caused by light refraction

As shown in Figure 3-6, the radial distance h changed from the true location h_0 on the object plane to the imaging location h_i on the image plane caused by light refraction. According to Snell's law of refraction,

$$n_d \sin\varphi_d = n_a \sin\varphi_a \tag{3-1}$$

In Eq. 3-1, n_d, n_a are the indices of refraction of water and air, respectively, and φ_d, φ_a are the angles of incidence and refraction, respectively. The relationship between h_0 and h_i can be given by

$$h_0 = \left(1 - \frac{\tan(\varphi_a - \varphi_d)}{\tan\varphi_a}\right) h_i = \beta h_i \tag{3-2}$$

Where

$$\beta = \frac{1}{\sqrt{1 - k^2} \sqrt{(n_d/n_a)^2 - k^2} + k^2} \tag{3-3}$$

And k is the ratio between h_i and the droplet diameter R.

$$k = {h_i}/{R} \tag{3-4}$$

Eq. 3-2, Eq. 3-3 and Eq. 3-4 indicated that the radial distance was enlarged on the image plane by the lensing effect of the curved droplet surface.
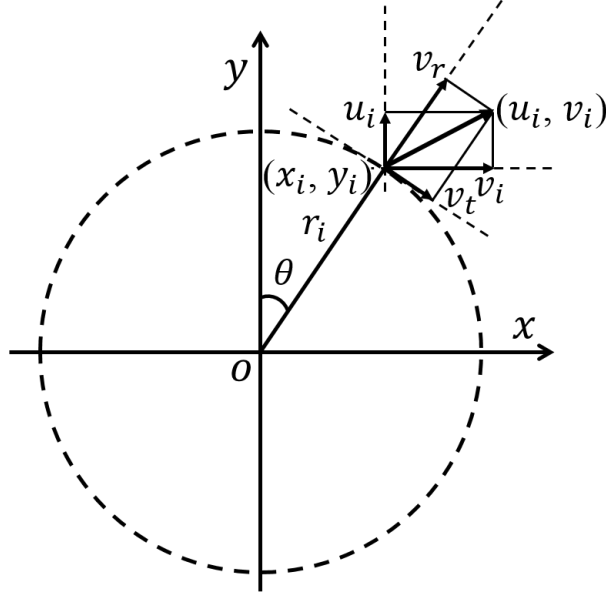
Figure 3-7. Coordinate system and the velocity decomposition in Cartesian coordinate
and in polar coordinate

The optical distortion in the 2D temperature and velocity distributions can be corrected using Eq. 3-2, Eq. 3-3 and Eq. 3-4. As shown in Figure 3-7, the (x, y) 2D Cartesian and (r, θ) polar coordinate systems are built with the origin at the center of the droplet.

In the following equations, the symbols with subscript i represent the coordinates and components of velocity on the image plane, and the symbols with subscript 0 represent the coordinates and components of velocity on the object plane.

In the (r, θ) polar coordinate system, the coordinate displacement between the object plane and the image plane only occurred on the radial direction which results in the following expressions.

$$\theta_0 = \theta \tag{3-5}$$

$$r_0 = \beta r_i = \frac{r_i}{\sqrt{1 - (r_i/R)^2}\sqrt{(n_d/n_a)^2 - (r_i/R)^2} + (r_i/R)^2} \tag{3-6}$$

Therefore, in the (x, y) Cartesian coordinate system, the coordinate displacement caused by the distortion can be easily corrected by the following equations.

$$x_0 = \beta x_i \tag{3-7}$$

$$y_0 = \beta y_i \tag{3-8}$$

Here

$$\beta = \frac{1}{\sqrt{1-k^2}\sqrt{(^{n_d}/_{n_a})^2 - k^2 + k^2}} \tag{3-9}$$

$$k = {}^{r_i}/_R \tag{3-10}$$

$$r_i = \sqrt{x_i^2 + y_i^2} \tag{3-11}$$

Conversion between the velocity decomposition in the Cartesian and polar coordinates can be given as follows.

$$v_r = \sin\theta u_i + \cos\theta v_i \tag{3-12}$$

$$v_t = \cos\theta u_i - \sin\theta v_i \tag{3-13}$$

In order to obtain the velocity distribution on the object plane before the optical distortion, we take the time derivative of Eq. 3-5 and 3-6.

$$v_{r0} = \frac{dr_0}{dt} = v_r \frac{\partial r_0}{\partial r_i} \tag{3-14}$$

$$v_{t0} = r_0 \frac{d\theta_0}{dt} = \frac{r_0\, r_i d\theta}{r_i\,\, dt} = \beta v_t \tag{3-15}$$

The derivative $\partial r_0 /_{\partial r_i}$ can be easily calculated using the Python library SymPy. Figure 3-8 gives a curve of the relationship between r_0 (ratio to R from 0 to 1.0) on the object plane and r_i (ratio to R from 0 to 1.0) on the image plane, and the derivative $\partial r_0 /_{\partial r_i}$ is shown in the graph as well. According to this calculation, near the droplet

surface (r > 0.95R), the optical distortion becomes huge and can cause large errors, especially in velocity distribution (see the Figure 3-8). Therefore, velocity and temperature data near the droplet surface (when r > 0.95R) were eliminated during the distortion correction.
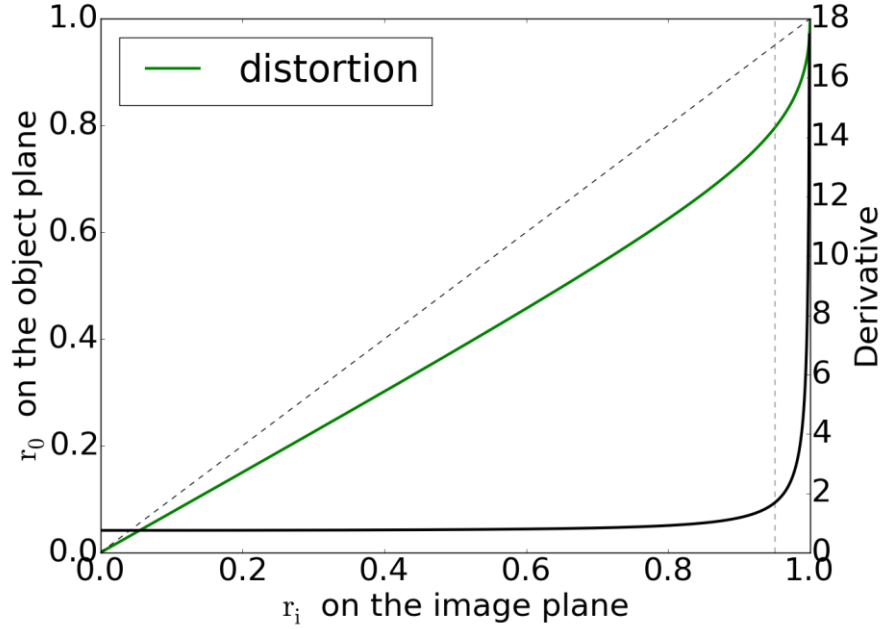
Figure 3-8. Relationship between r_0 and r_i, with derivative ${\partial r_0}/{\partial r_i}$

Using Eq. 3-14 and Eq. 3-15, the changes in the radial and tangential components of velocity can be calculated. The corrected velocity in Cartesian coordinates can be obtained as follows.

$$v_0 = \sin\theta v_{r_0} + \cos\theta v_{t_0} \tag{21}$$

$$v_0 = \sin\theta v_{r_0} + \cos\theta v_{t_0} \tag{22}$$

Figure 3-9 shows a comparison of the measured velocity field and distribution profile along the central axis inside the water droplet after 75 ms in upward air stream at room temperature (approximately 20 °C) before and after the optical distortion correction. It was observed that although the flow field was similar before and after the

distortion, the central plane of the droplet was magnified by the lensing effect, and the velocities were overestimated.
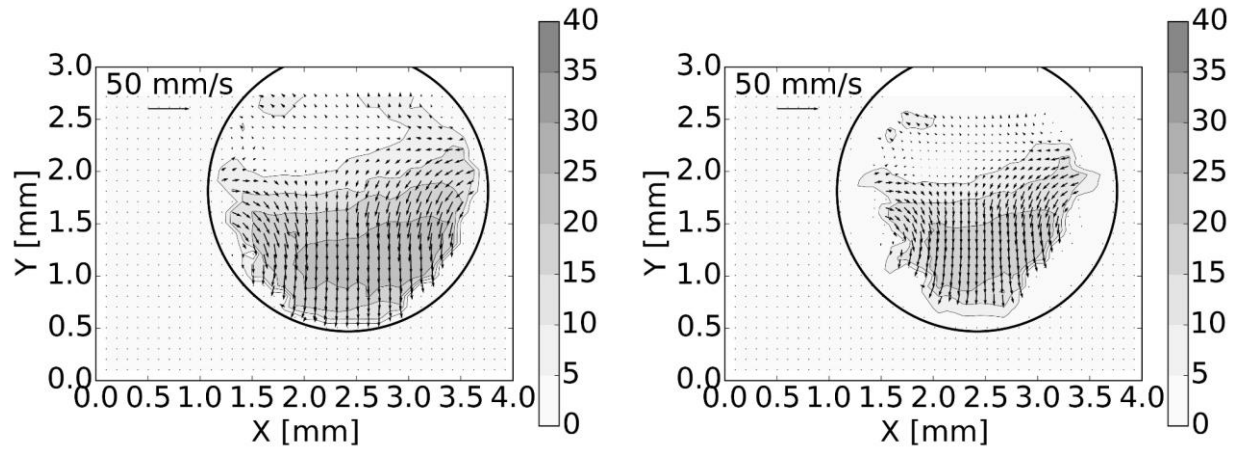
(a) Before the optical distortion correction

(b) After the optical distortion correction
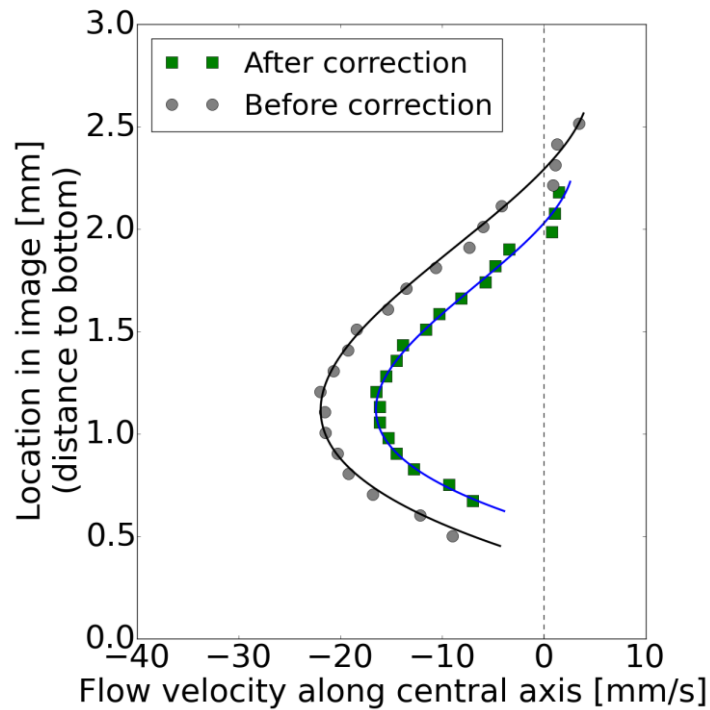
(c) The vertical velocity component distribution profile along the droplet central axis

Figure 3-9. A comparison of the measured velocity distribution inside the water droplet after 75 ms in upward air stream at room temperature (approximately 20 °C) before and after the optical distortion correction.

Because of the optical distortion, at the current stage, it was not possible to obtain an accurate temperature and velocity distribution near the edge of the droplets.

3.1.3.Preliminary experiment

Table 3-1. Experimental parameters of preliminary experiment

Parameter	Value
Droplet initial temperature ($^{\bullet}C$)	24.7
Droplet diameter (*mm*)	1.87
Air stream temperature ($^{\bullet}C$)	100
Air stream velocity (*m/s*)	1
Air stream humidity	Ambient humidity (40%)
Measurement time (*time after air stream started*)	Single shots at 1-20 seconds

Several droplet evaporation experiments have been conducted in this study. Table 3-1 gives the experimental parameters. The initial temperature and size of the water droplets were measured during the experiments.

Before continuous measurements, preliminary tests have been conducted to obtain single shots of the temperature and flow distributions inside the pendant droplets at several different moments after the air stream started.
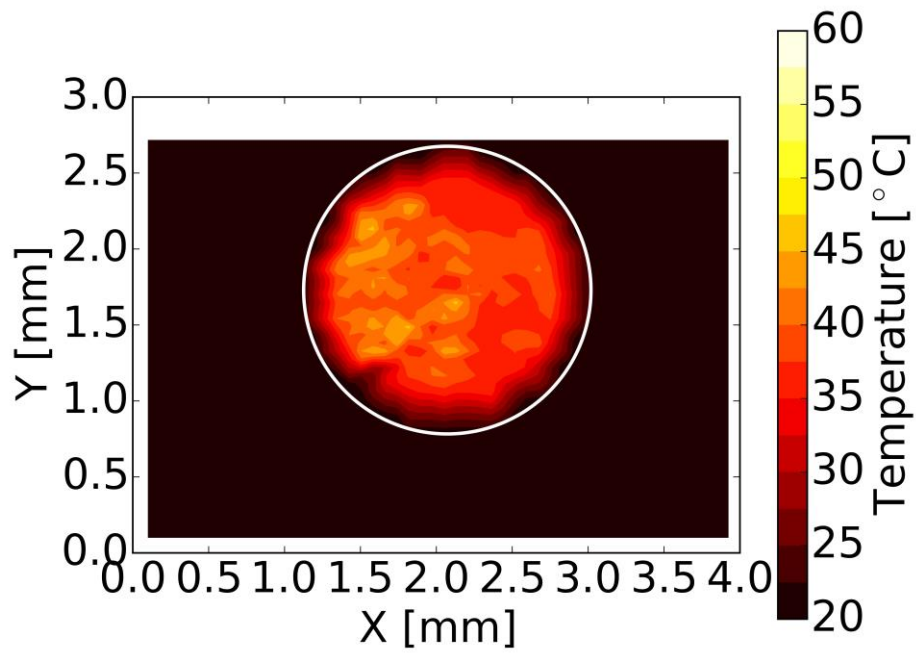
Figure 3-10. Measured temperature distribution inside a pendant droplet at 5 s after air heating was started in 100 °C air stream
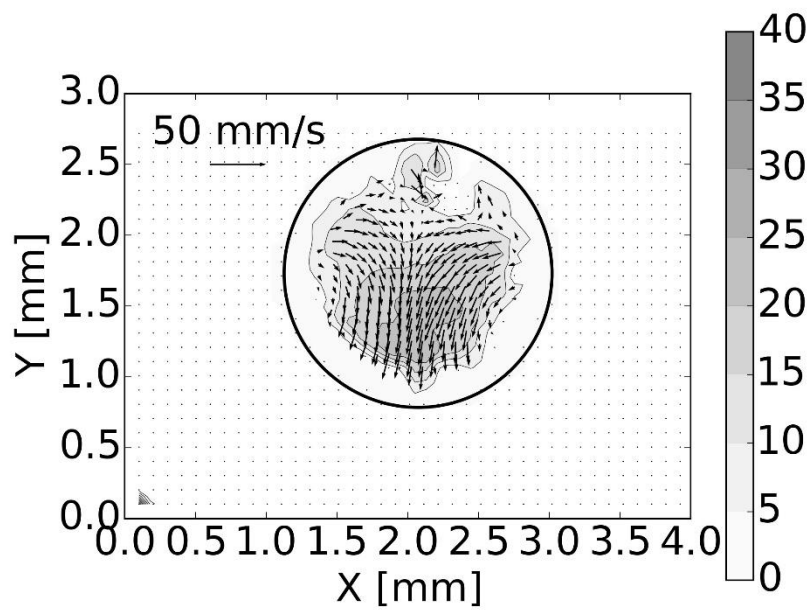
Figure 3-11. Measured velocity distribution inside a pendant droplet at 5 s after air heating was started in 100 °C air stream

Figure 3-10 and Figure 3-11 give the measured temperature and flow distributions at the moment of 5 s after air heating was started inside a pendant droplet in 100 °C air

stream. The white circle in the temperature distribution and the black circle in the velocity distribution represent the interface boundary of the droplet.

Overall, the droplet internal temperature distribution shown in Figure 3-10 was approximately 40 °C, which was considerably low compared to the heating gas temperature of 100 °C, and several uneven regions were observed within a temperature discrepancy of 10 °C. A similar non-uniformity in the internal temperature was reported in the results of a thermographic phosphor measurement that focused on a free-falling spray droplet [21]. Figure 3-10 shows that the droplet temperature did not increase to a high value in 5 s, which indicated a high evaporative heat absorption, and the water mixing inside the evaporating droplet may enhance the internal heat exchange.
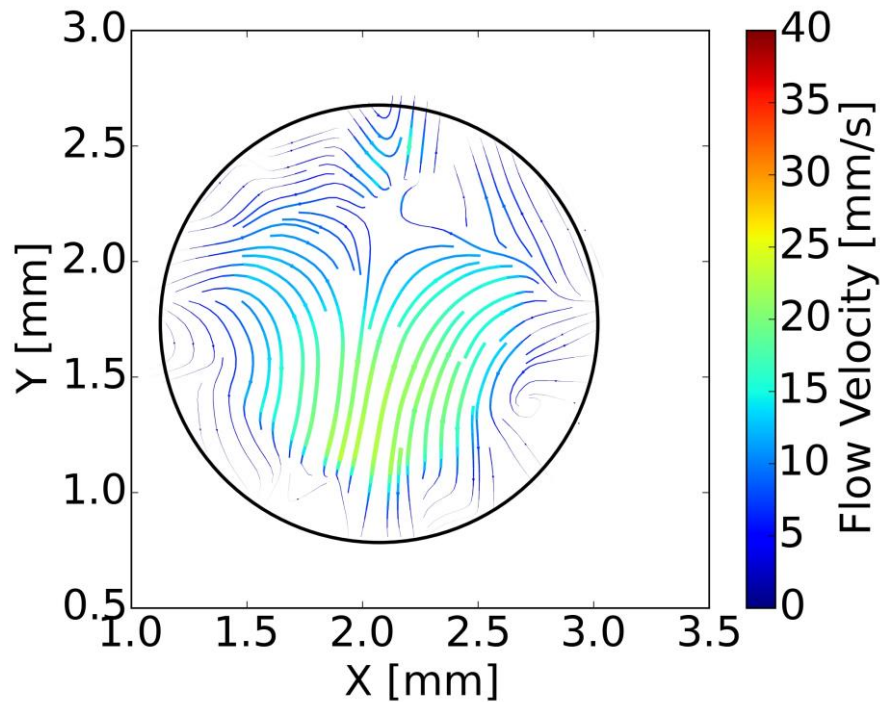
Figure 3-12. Droplet internal streamlines after 5 s in 100 °C air stream

Figure 3-11 shows an overall downward flow pattern at the center of the evaporating droplet. Figure 3-12 shows the droplet internal streamlines at the time instant corresponding to Figure 3-11. Although the streamlines obtained here were not strictly axisymmetric, as previously introduced in section 1.2.2, the central part of a toroidal convection pattern (the Hill's vortex) can be observed to develop inside the

droplet. Despite its incompleteness caused by optical distortion, the internal motion seen here within the droplet has been reported in several previous numerical studies on the droplet behavior in a gas stream [39, 40]. A theoretical model of the internal circulation in water droplets falling at terminal velocity in air was provided by LeClair et al. [41], which showed that the droplet internal streamlines were similar to those shown in Figure 3-12 for a Reynolds number of 100.

A problem observed in the preliminary tests was that the possible EuTTA elution, precipitation, and agglomeration of particles resulted in the loss of tracers during the measurement and caused some desiccated layers of the particles to be attached to the droplet surface, which introduced a noise region, as shown in the upper-right area of Figure 3-11. Besides, due to the loss of tracers during the measurements, the PIV-TSP technique can only be used to measure the temperature and velocity inside droplets continuously for several seconds. This problem is a current limitation of the proposed TSP method for measurements inside droplets and should be taken into account in applications and further investigations.

3.2. Experiment of droplet internal flow development

In order to investigate this toroidal convection pattern inside evaporating droplets, experiments have been conducted focusing on the internal flow development of a pendant droplet at the beginning its evaporation in upward air stream. It should be noticed that in the experiment discussed in this section, since we focused on the flow pattern development and variation, only the velocity distributions were measured. These experiments were conducted at low particle-density conditions that may induce high measurement error into the TSP analysis, therefore the temperature distributions were not measured.

3.2.1.Experimental conditions

Table 3-2 gives the experimental parameters of the experiments to measure the droplet internal flow variation during the developing period.

Table 3-2. Experimental parameters of droplet flow measurements

Parameter	Value
Droplet initial temperature (°C)	22.3
Droplet diameter (mm)	2.31-2.64
Air stream temperature (°C)	20 (RT), 40, 60, 80, 100
Air stream velocity (m/s)	1
Air stream humidity	Ambient humidity (40%)
Measurement time (time after air stream started)	Continuously in the first 150 ms

In the above Table, "RT" means "room temperature". Measurements have been conducted at several different air stream temperature conditions from 20 °C to 100 °C. The temperature of air stream was just measured before the droplet tests and it fluctuated within a range of 5 °C. Because the air stream temperature was not measured during the droplet evaporation, considering there was a short temperature rising time at the outlet of the gas channel after the air stream started, the actual temperature of air stream during the measurements may be lower than the values shown in Table 3-2.

In this experiment, flow distributions were measured inside 2-mm pendant water droplets evaporating in upward air stream once per 15 ms after air stream started, by setting the time period of cyclical signal transmission at 15 ms, and the measurements were conducted continuously for 150 ms to see the variation of droplet internal flow pattern during the developing period.

3.2.2.Experimental results and discussion

The flow distributions obtained in this experiment indicated that the internal flow pattern developed in the high temperature air stream was different from that developed in the air stream at room temperature. The measured internal flow velocity distributions and streamlines of evaporating droplets in 20 °C and 100 °C air stream are shown in Figure 3-13, from 0 ms to 90 ms after air stream started. Comparisons of the vertical component of velocity along droplet central axis obtained at the corresponding time instants are also given in Figure 3-14.

$T_{air} = 20$ °C, t = 0 ms

$T_{air} = 100$ °C, t = 0 ms
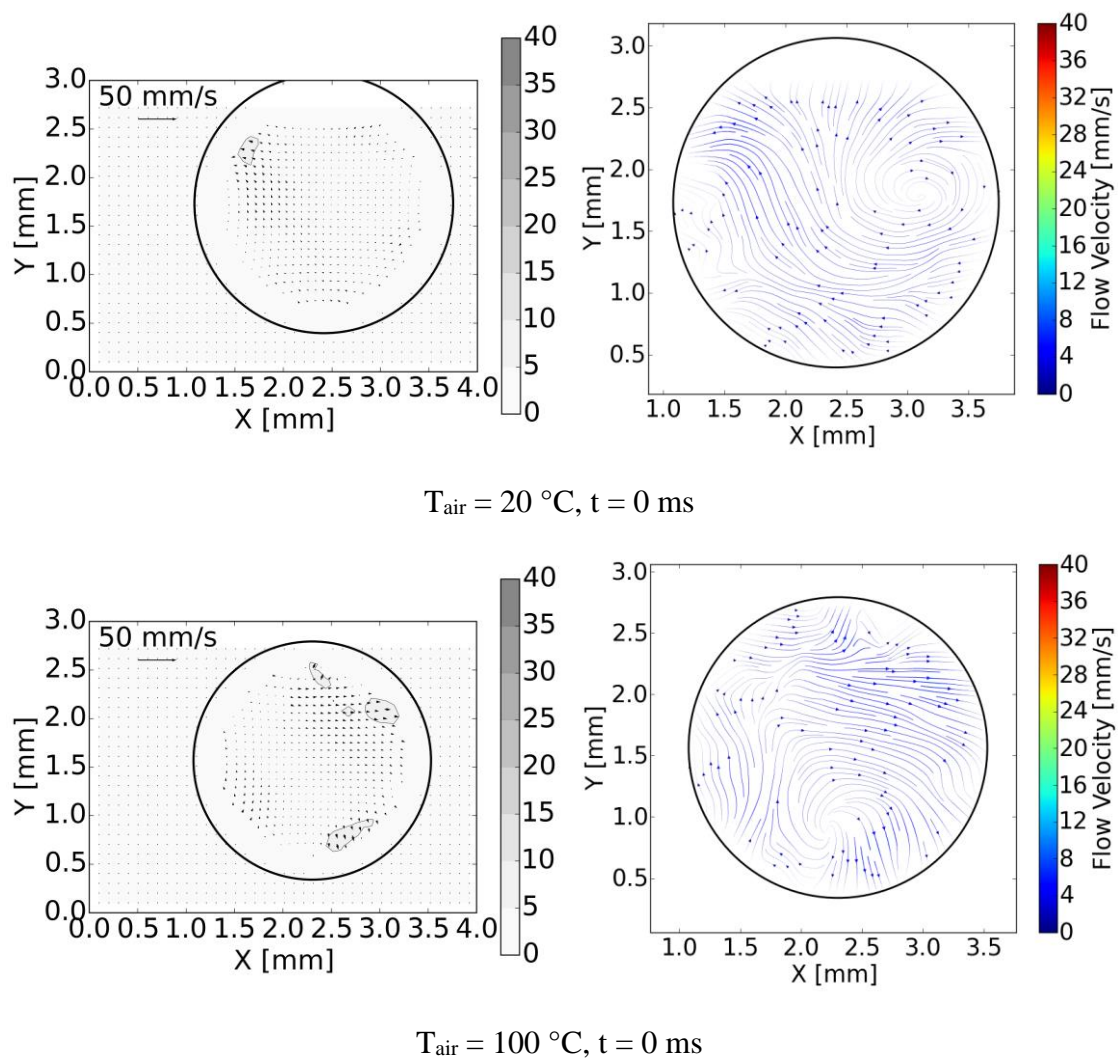
Figure 3-13a. Droplet internal velocity distributions and streamlines

$T_{air} = 20\ ^\circ C$, t = 15 ms

$T_{air} = 20\ ^\circ C$, t = 30 ms

$T_{air} = 100\ ^\circ C$, t = 15 ms
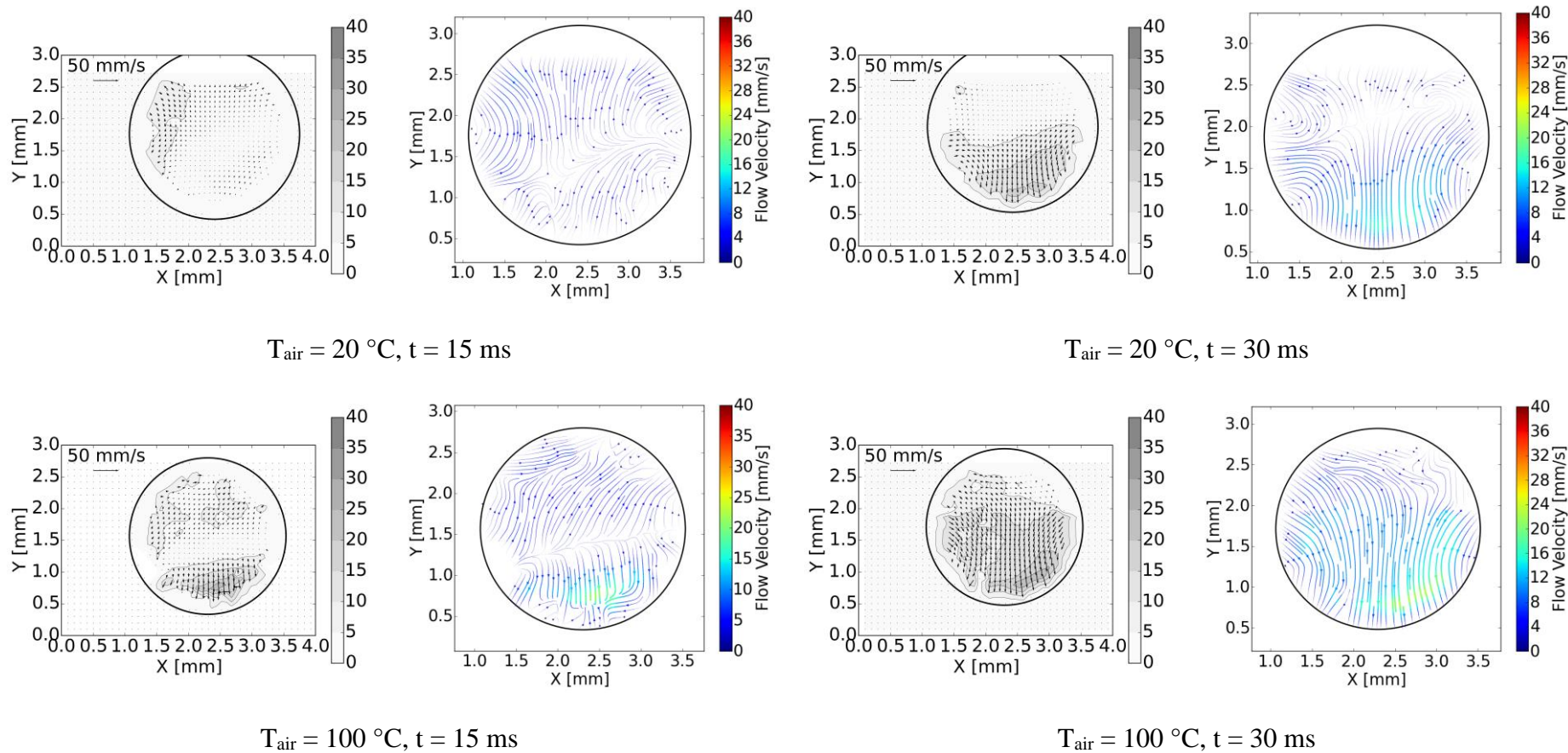
$T_{air} = 100\ ^\circ C$, t = 30 ms

Figure 3-13b. Droplet internal velocity distributions and streamlines

$T_{air} = 20\ °C,\ t = 45\ ms$ 　　　　　　　　　　　　　　$T_{air} = 20\ °C,\ t = 60\ ms$

$T_{air} = 100\ °C,\ t = 45\ ms$ 　　　　　　　　　　　　　$T_{air} = 100\ °C,\ t = 60\ ms$
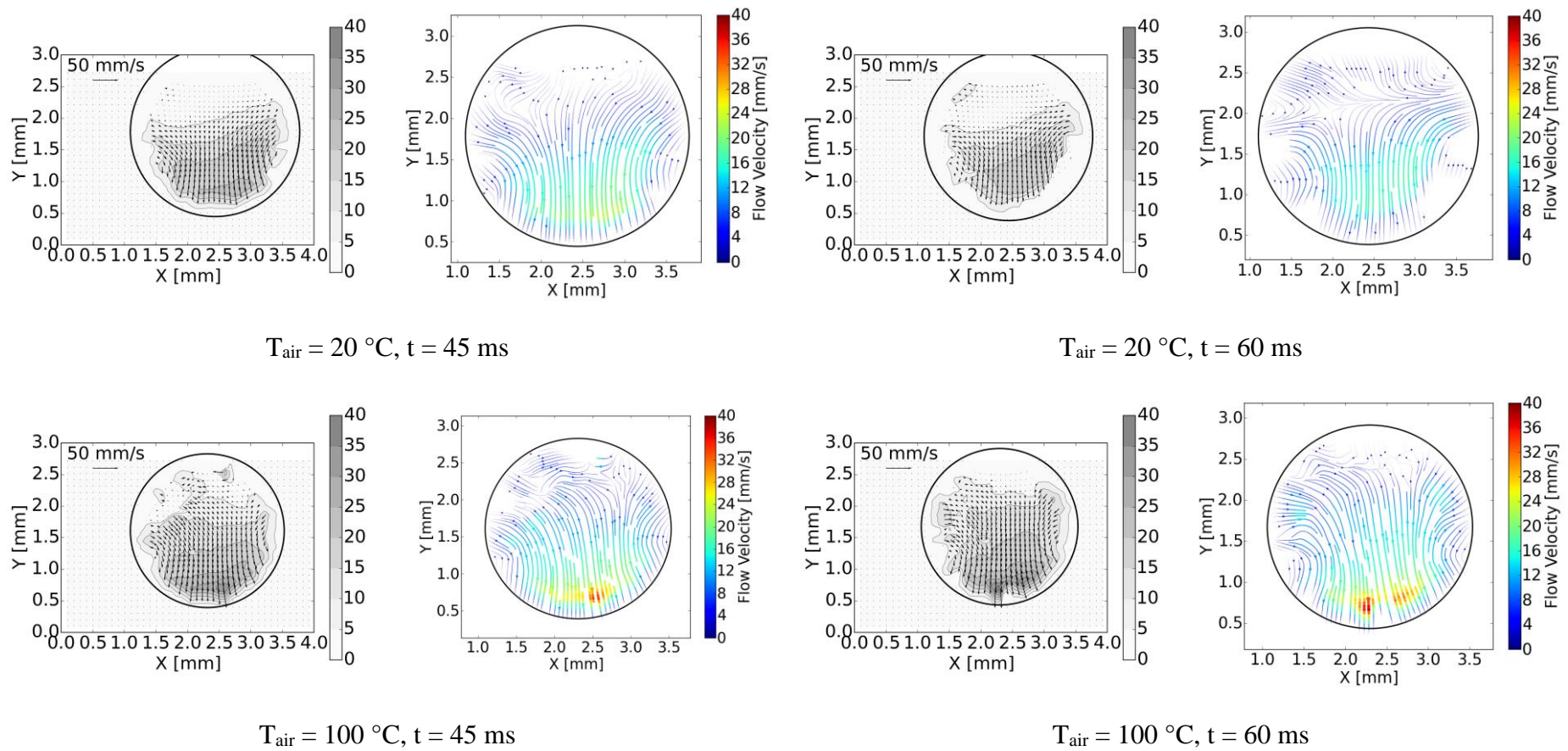
Figure 3-13c. Droplet internal velocity distributions and streamlines
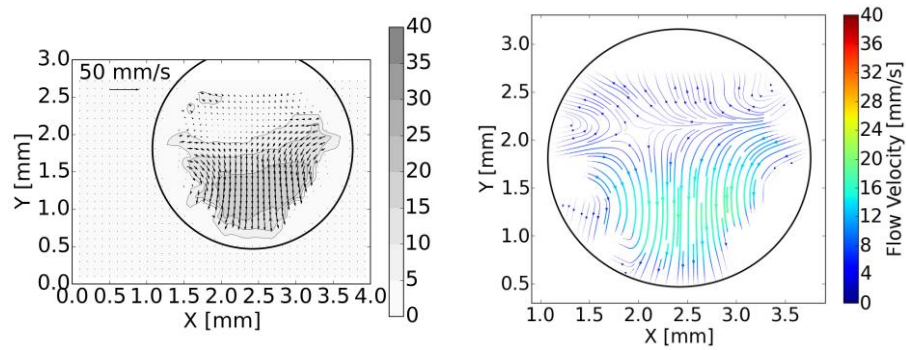
$T_{air} = 20\ °C,\ t = 75\ ms$
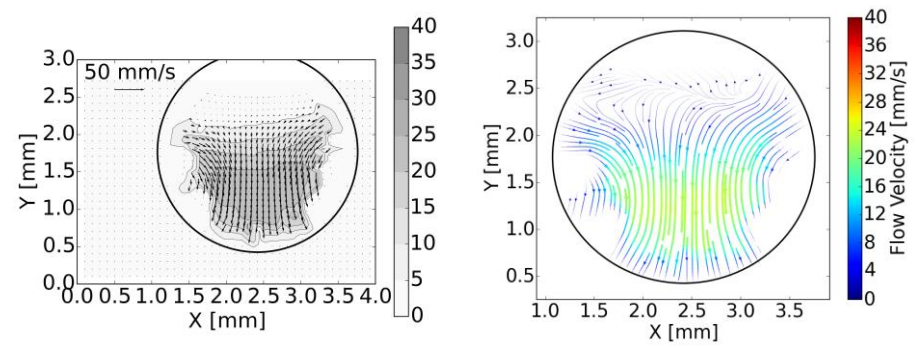
$T_{air} = 20\ °C,\ t = 90\ ms$
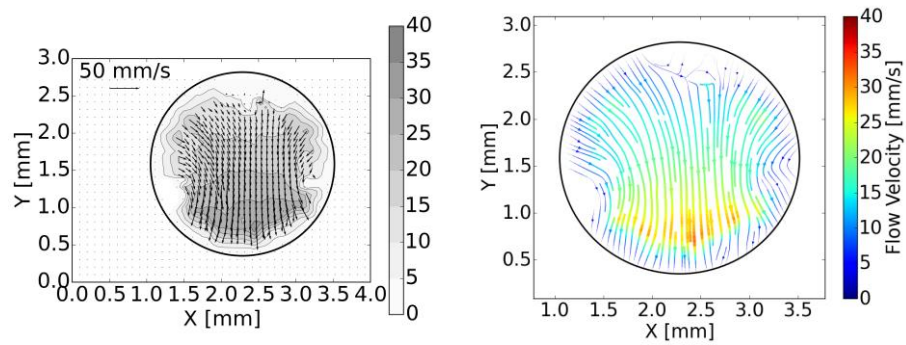
$T_{air} = 100\ °C,\ t = 75\ ms$
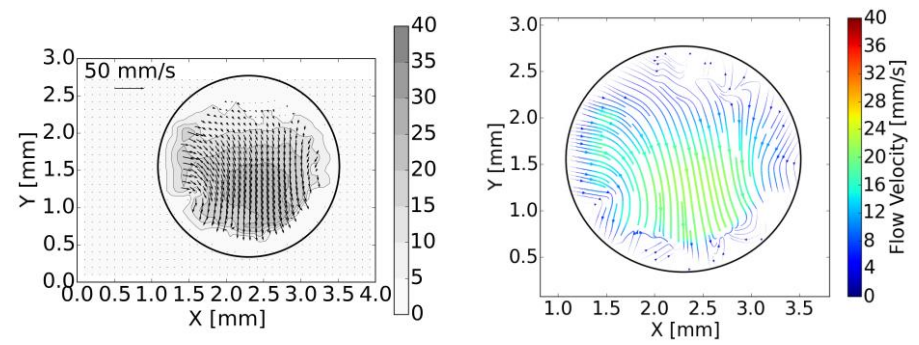
$T_{air} = 100\ °C,\ t = 90\ ms$

Figure 3-13d. Droplet internal velocity distributions and streamlines

t = 0 ms   t = 15 ms   t = 30 ms   t = 45 ms
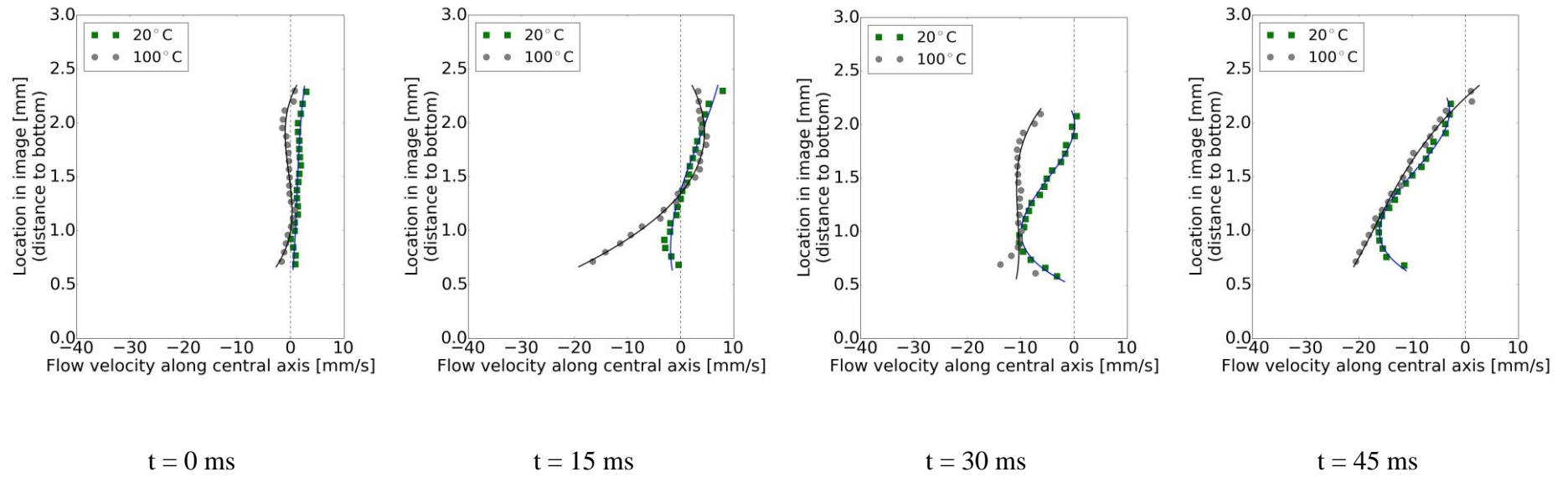
Figure 3-14a. Profile of the vertical component of velocity along droplet central axis

t = 60 ms   t = 75 ms   t = 90 ms
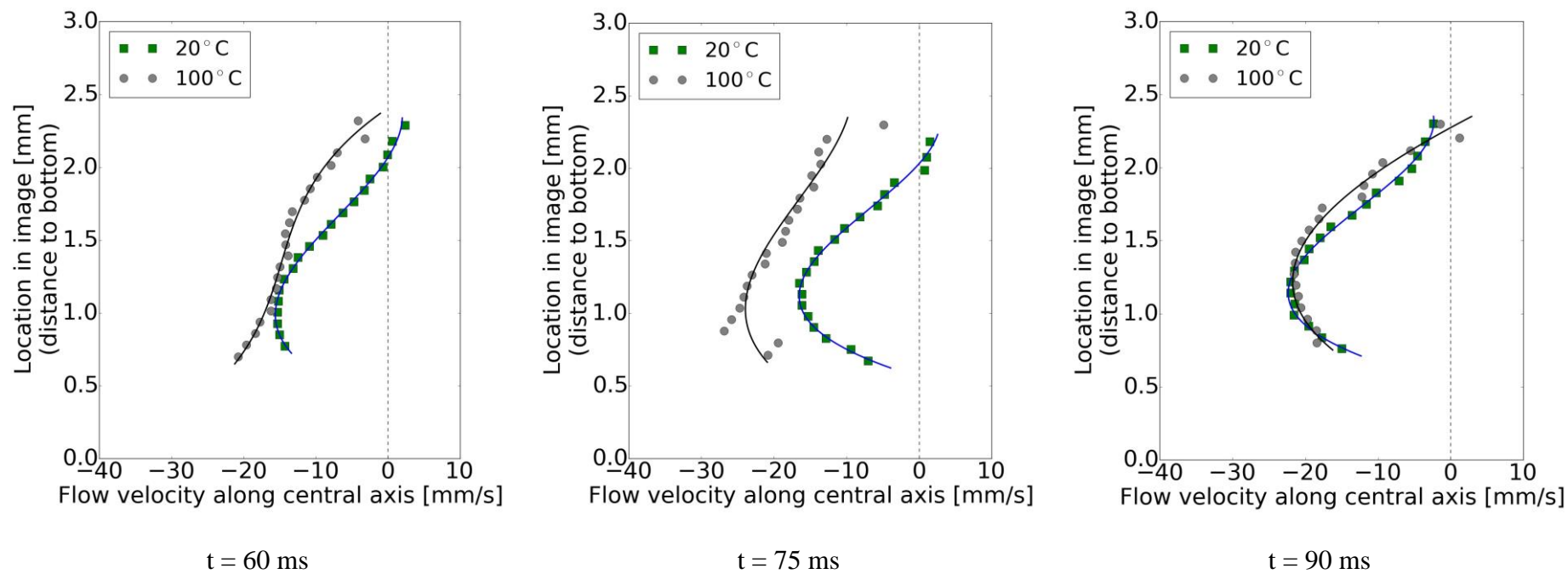
Figure 3-14b. Profile of the vertical component of velocity along droplet central axis

In 1 m/s upward air stream, the droplet internal flow was fully developed within 90 ms, at both 20 °C and 100 °C condition (see Figure 3-13). The internal motion seen here within the droplet was a toroidal convection pattern, downward flow in the center, known as Hill's vortex. It can be observed that a maximum flow velocity of up to approximately 30 mm/s was observed at the center-bottom of the droplet, which means that the internal flow cycled dozens of times per second, and thus, the droplet internal water mixing was believed to be enhanced by this circulation.

At higher temperature, the viscosity of air becomes larger, so the internal flow may develop faster. However, comparing the internal flow developing period of droplet evaporating in different temperature air stream, the results indicated that the flow development inside the droplet at high temperature condition was not as gradual as that in 20 °C air stream. Actually, at 30 ms, the internal flow at 100 °C condition was already developed in the entire droplet, while the downward flow at 20 °C condition only occurred in the lower region of the droplet.

In order to compare the internal circulation developments in 20 °C air stream and 100 °C air stream perspicuously, we focused on the velocity (vertical component) distributions in the center of droplets, as shown in Figure 3-14.

The differences in droplet internal flow developments in 20 °C air stream and 100 °C air stream can be clearly observed from Figure 3-14. The negative sign of velocity means that the flow was downward. At 20 °C air stream condition, the internal circulation was developed gradually, and the maximum velocity occurred in the lower region of the droplet, due to the shear force of air stream. However, at 100 °C air stream condition, flow velocity increased rapidly in the vicinity of the droplet bottom, then expanded to the entire droplet, because of droplet internal vortex. This kind of flow extension occurred several times within 90 ms, and consequently, the flow development was faster in 100 °C air stream than in 20 °C.

Despite the difference in droplet size, downward flow developed inside the entire droplet at high temperature air stream condition, and the flow velocities were higher with an acceleration near the bottom of the droplet during the flow developing period. This acceleration induced the above-mentioned rapid velocity increase near the droplet bottom surface and internal flow extension at high temperature evaporating condition.

Marangoni convection caused by the difference in liquid surface tension is considered to contribute to the droplet velocity distribution heated by high temperature air stream. The inner convective motion driven by the Marangoni effect reported by Tam et al. [42] showed a very similar acceleration at the center-bottom near the heat source. Therefore, analogous to the effect of a hot solid surface on a droplet, it can be inferred that a hot air stream induces a vertical temperature gradient on the droplet surface, which leads to a gradient in the surface tension and in turn contributes to the internal flow circulation.
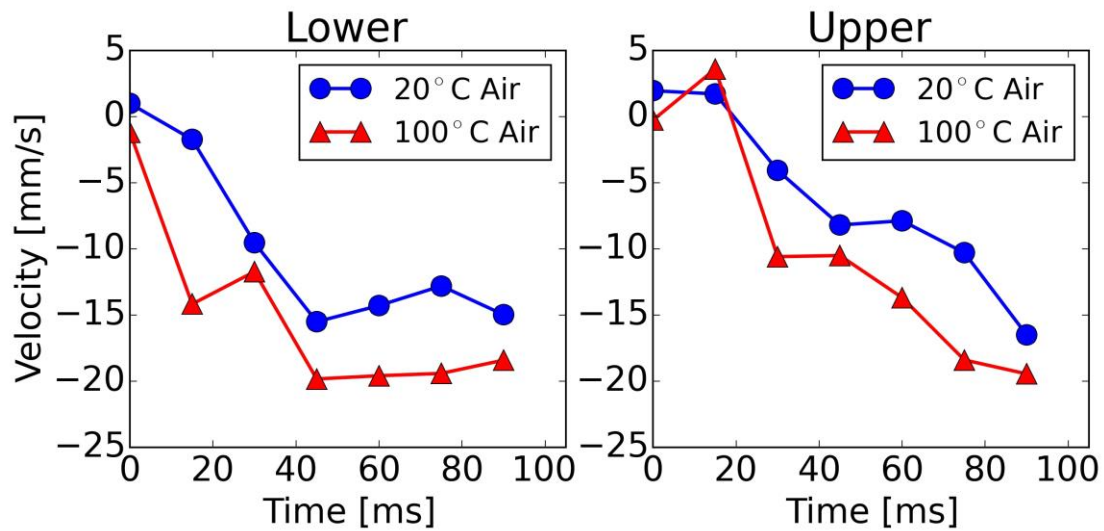
Figure 3-15. Vertical component of velocity variations against time at a lower location (0.4 mm from bottom) and an upper location (1.4 mm from bottom) inside the droplets

Figure 3-15 shows the variations of the vertical component of velocity against time at two different locations inside the evaporating droplets in 20 °C air stream and 100 °C

air stream. It can be observed that in 20 °C air stream, the flow developed gradually, and the development of velocity was synchronous. The flow fully developed at 45 ms in the lower region and at 90 ms in the upper region. However, in 100 °C air stream, the flow developed with step changes, twice at lower location and once at upper location. This development further confirmed the contribution of the Marangoni convection to the droplet internal flow circulation.
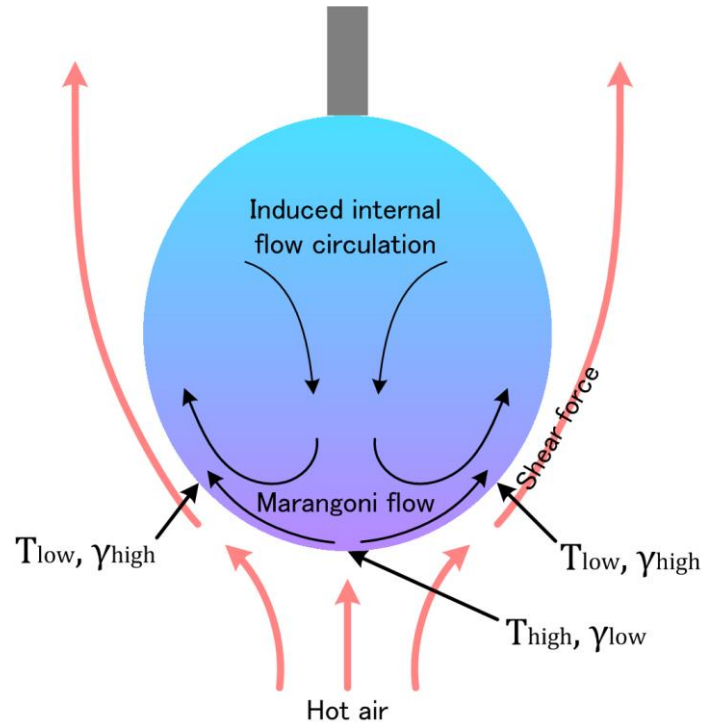
Figure 3-16. Schematic of droplet internal circulation development

A schematic of droplet internal circulation is shown in Figure 3-16. The droplet inner convective motion is induced by the Marangoni effect due to the gradient in the surface tension and the shear force of air flow, and the droplet internal water mixing was enhanced by this circulation. This schematic shows the flow inside droplets driven by the hot air stream at the beginning of evaporation.

Although the velocity distributions obtained at 90 ms are similar in 20 °C air stream and 100 °C air stream, the flow was developed and the flow pattern may remain stable at room temperature condition, but at 100 °C condition, later on, the water mixing of droplets and the hot air stream may further change the temperature gradient on the

surface, and the internal flow pattern may change again. This further variation of internal flow will be shown and discussed in the next chapter.

3.3. Conclusion of the chapter

The proposed technique introduced in chapter 2 was applied to measure the temperature and flow distributions simultaneously inside pendant water droplets in upward air stream. An anti-distortion algorithm was used to correct the optical distortion induced by the curved surface of the droplet.

As preliminary tests, single shots of temperature and flow distributions were measured at several different moments after air stream started. The central part of a toroidal convection pattern (the Hill's vortex) was observed to develop inside the droplets.

Using the cyclical signal control and the RANDOM mode of camera recording, continuous measurements can be implemented to measure the velocity and temperature inside droplets at the beginning of the evaporation after air stream started.

The velocity distributions were measured continuously inside the droplets during the flow developing period at the beginning of droplet evaporation in upward air stream. The results show that the droplet internal flow developed within a short time of approximately 90 ms. Comparing with data obtained under 20°C air stream condition, the droplet internal circulation development in 100°C air stream was faster, and the flow was developed in the entire droplet. It can be inferred that the droplet inner convective motion in upward hot air stream is induced by the Marangoni effect due to the gradient in the surface tension and the shear force of air flow, and the droplet internal water mixing can be enhanced by this circulation.

4. Droplet heat and mass transfer

4.1. Outline of the work

In order to investigate the behavior of droplet evaporation heat and mass transfer, in this chapter, the afore-mentioned PIV-TSP technique was used to measure the internal temperature and flow distributions of droplets evaporating in upward air stream. The experimental results obtained are compared and discussed with the results of droplet heat and mass transfer calculation using some well-known correlations of droplet vaporization.

4.2. Experiment of droplet internal temperature and flow variations

4.2.1. Experimental conditions and method

Table 4-1 gives the experimental parameters of simultaneous droplet internal temperature and flow measurements.

Table 4-1. Experimental parameters of droplet temperature and flow measurements

Parameter	Value		
Droplet initial temperature ($^{\bullet}C$)	23.43	25.00	26.58
Droplet diameter (*mm*)	2.42	2.37	2.36
Air stream temperature ($^{\bullet}C$)	34.2	66.2	79.5
Air stream velocity (*m/s*)	1		
Air stream humidity	Ambient humidity (40%)		
Measurement time (*time after air stream started*)	Continuously in the first 1 s		

The initial temperature and size of the water droplets were measured during the experiments. The ambient temperature of experiments was approximately 22 °C. The temperature and flow distributions were measured inside droplets using PIV-TSP technique every 20 ms.
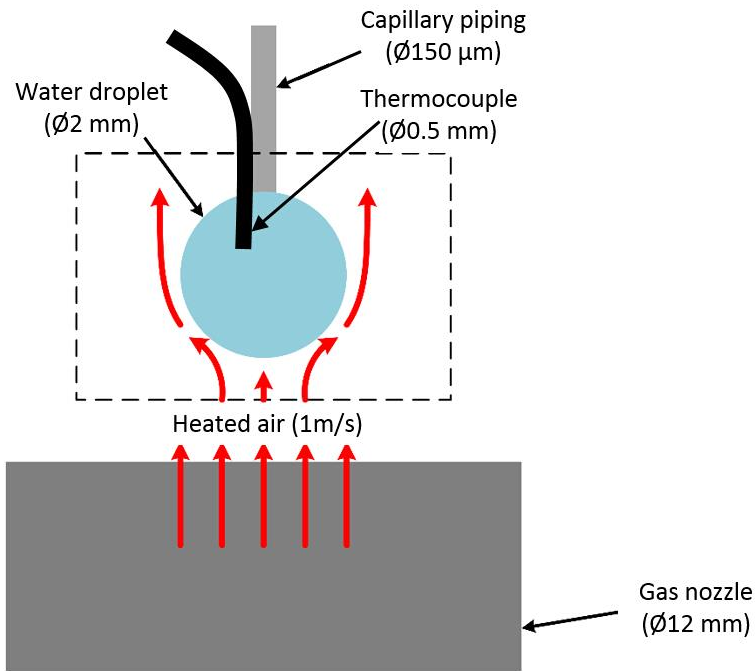
Figure 4-1. Schematic of droplet temperature measurements using thermocouple

Another experiment was conducted to measure the droplet temperature variations using the K-type thermocouple for verification of TSP measurements. As shown in Figure 4-1, a K-type thermocouple with 0.5 mm in diameter was fixed on the capillary piping and inserted into the water droplet. The measurement frequency was 10Hz. Despite that the thermocouple probe may affect the heat exchange and the internal flow of droplets, the comparison between the droplet temperature measured by TSP and thermocouple can be used as a reference.
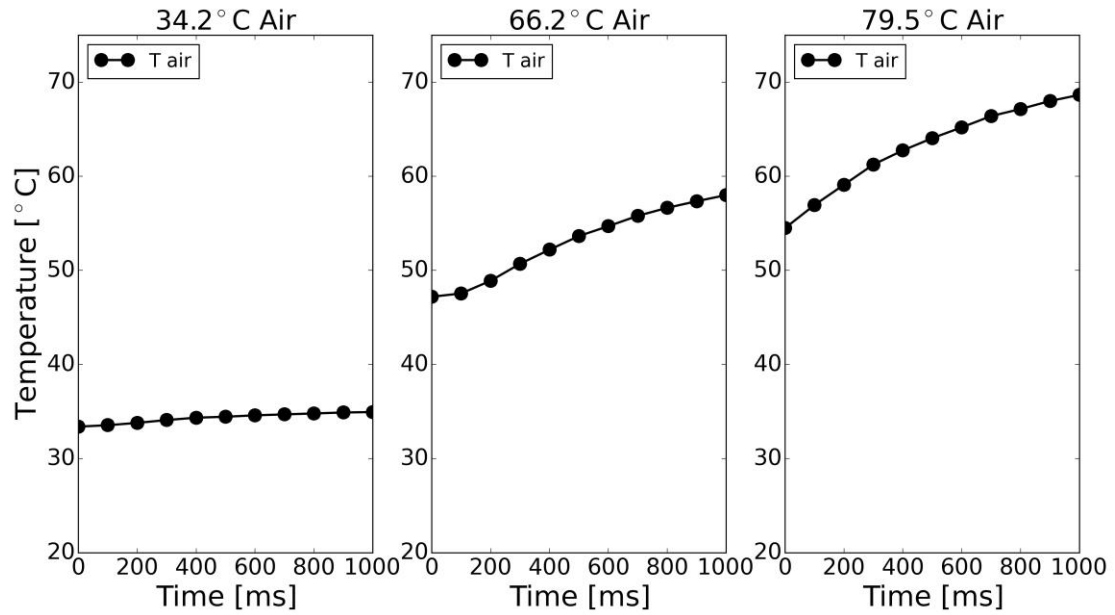
Figure 4-2. Temperature variations of air stream during droplet measurements period

It should be noticed that the air stream temperature shown in Table 4-1 was measured in developed air stream, considering that there was a short temperature rising time at the outlet of the gas channel after the air stream started, the actual temperature of air stream during the measurements may be lower than the values shown in Table 4-1. In this experiment, the air stream temperature variations around the droplet were also measured using a K-type thermocouple during the measurements period (the 1st second of the droplet evaporation). These temperature values of air stream were used for droplet evaporation calculations.

4.2.2. Experimental results

Figure 4-3 gives the internal temperature distributions, velocity distributions and corresponding streamlines inside the evaporating droplets in upward air stream at 34.2 °C, 66.2 °C and 79.5 °C measured by PIV-TSP technique.

T_air = 34.2 °C, t = 0 s   T_air = 34.2 °C, t = 0.1 s   T_air = 34.2 °C, t = 0.2 s   T_air = 34.2 °C, t = 0.3 s

Figure 4-3a. Droplet internal temperature distributions, velocity distributions and streamlines during evaporation

T_{air} = 34.2 °C, t = 0.4 s T_{air} = 34.2 °C, t = 0.5 s T_{air} = 34.2 °C, t = 0.6 s T_{air} = 34.2 °C, t = 0.7 s

Figure 4-3b. Droplet internal temperature distributions, velocity distributions and streamlines during evaporation

T_{air} = 34.2 °C, t = 0.8 s T_{air} = 34.2 °C, t = 0.9 s T_{air} = 34.2 °C, t = 1.0 s

Figure 4-3c. Droplet internal temperature distributions, velocity distributions and streamlines during evaporation

$T_{air} = 66.2\ °C,\ t = 0\ s$ $T_{air} = 66.2\ °C,\ t = 0.1\ s$ $T_{air} = 66.2\ °C,\ t = 0.2\ s$ $T_{air} = 66.2\ °C,\ t = 0.3\ s$
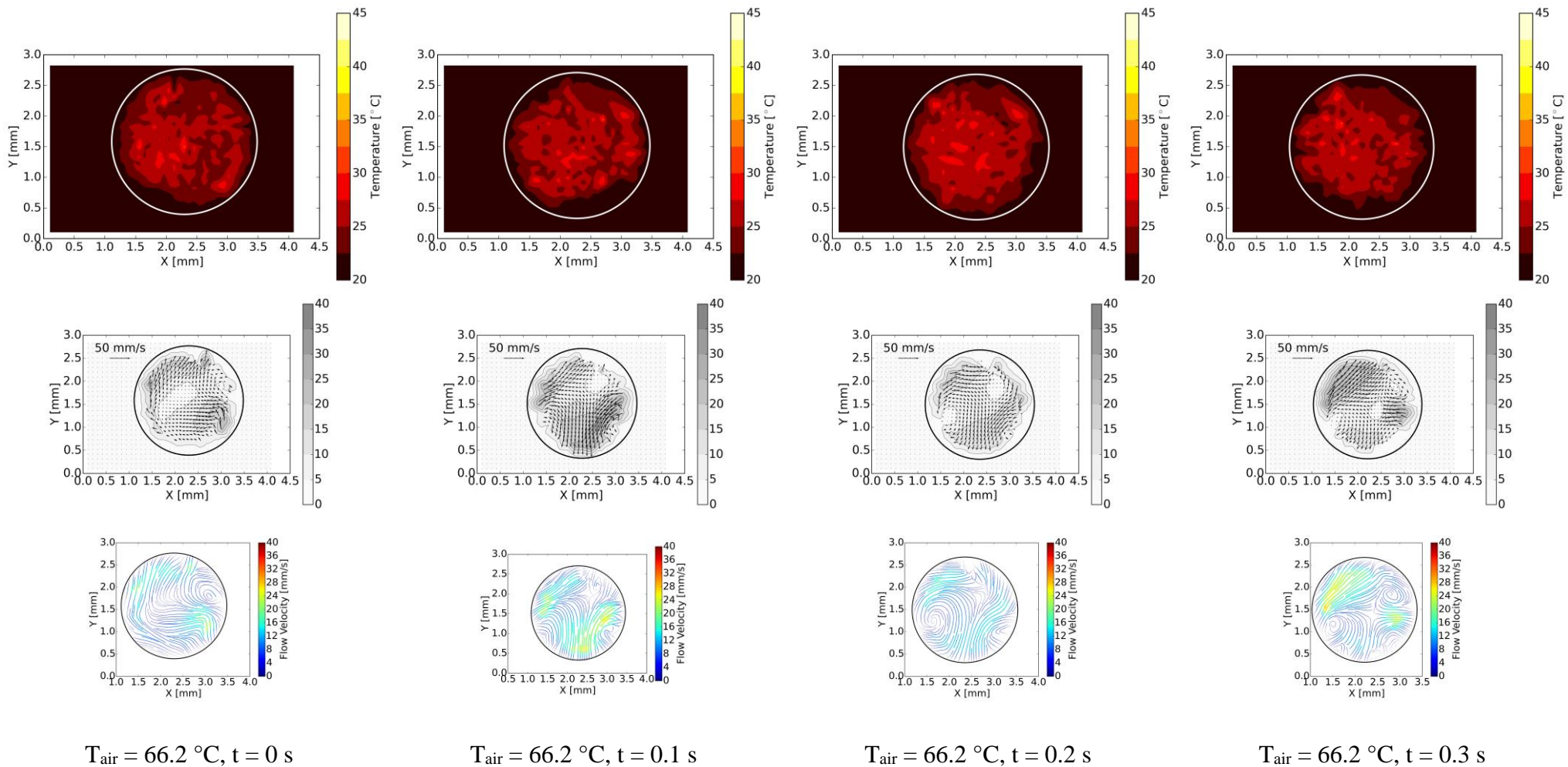
Figure 4-3d. Droplet internal temperature distributions, velocity distributions and streamlines during evaporation
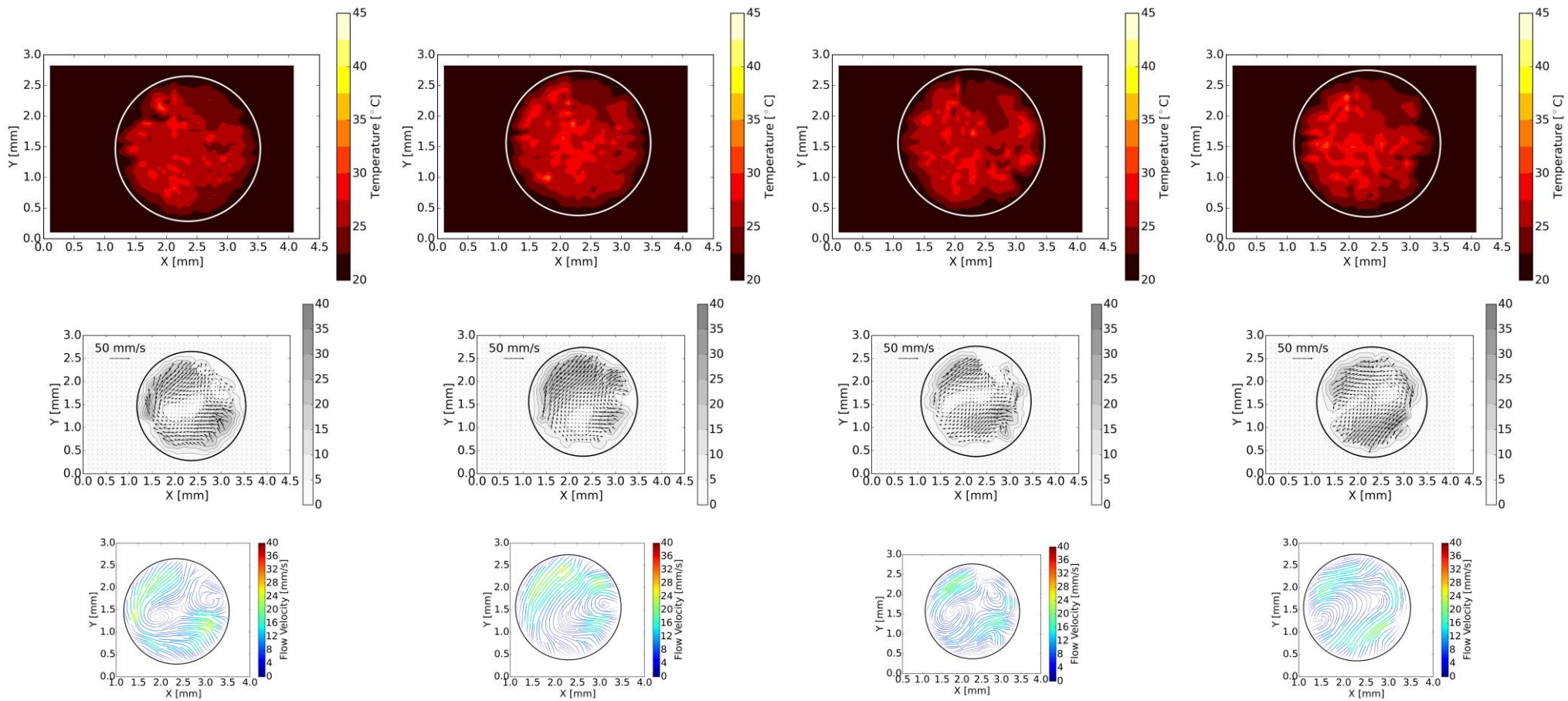
| $T_{air} = 66.2\ °C,\ t = 0.4\ s$ | $T_{air} = 66.2\ °C,\ t = 0.5\ s$ | $T_{air} = 66.2\ °C,\ t = 0.6\ s$ | $T_{air} = 66.2\ °C,\ t = 0.7\ s$ |

Figure 4-3e. Droplet internal temperature distributions, velocity distributions and streamlines during evaporation

T_{air} = 66.2 °C, t = 0.8 s T_{air} = 66.2 °C, t = 0.9 s T_{air} = 66.2 °C, t = 1.0 s
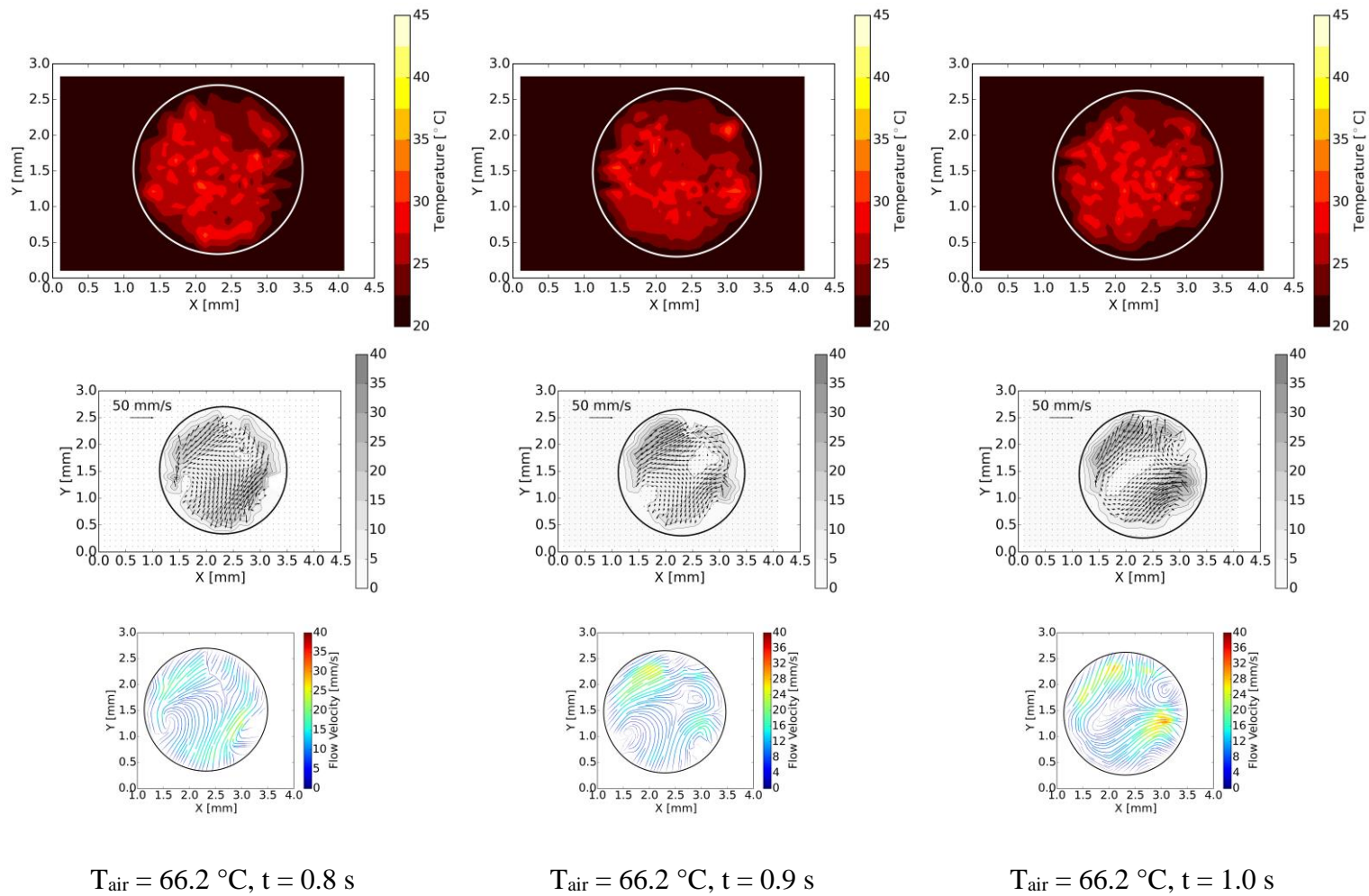
Figure 4-3f. Droplet internal temperature distributions, velocity distributions and streamlines during evaporation

$T_{air} = 79.5\ ^\circ C, t = 0\ s$ $T_{air} = 79.5\ ^\circ C, t = 0.1\ s$ $T_{air} = 79.5\ ^\circ C, t = 0.2\ s$ $T_{air} = 79.5\ ^\circ C, t = 0.3\ s$
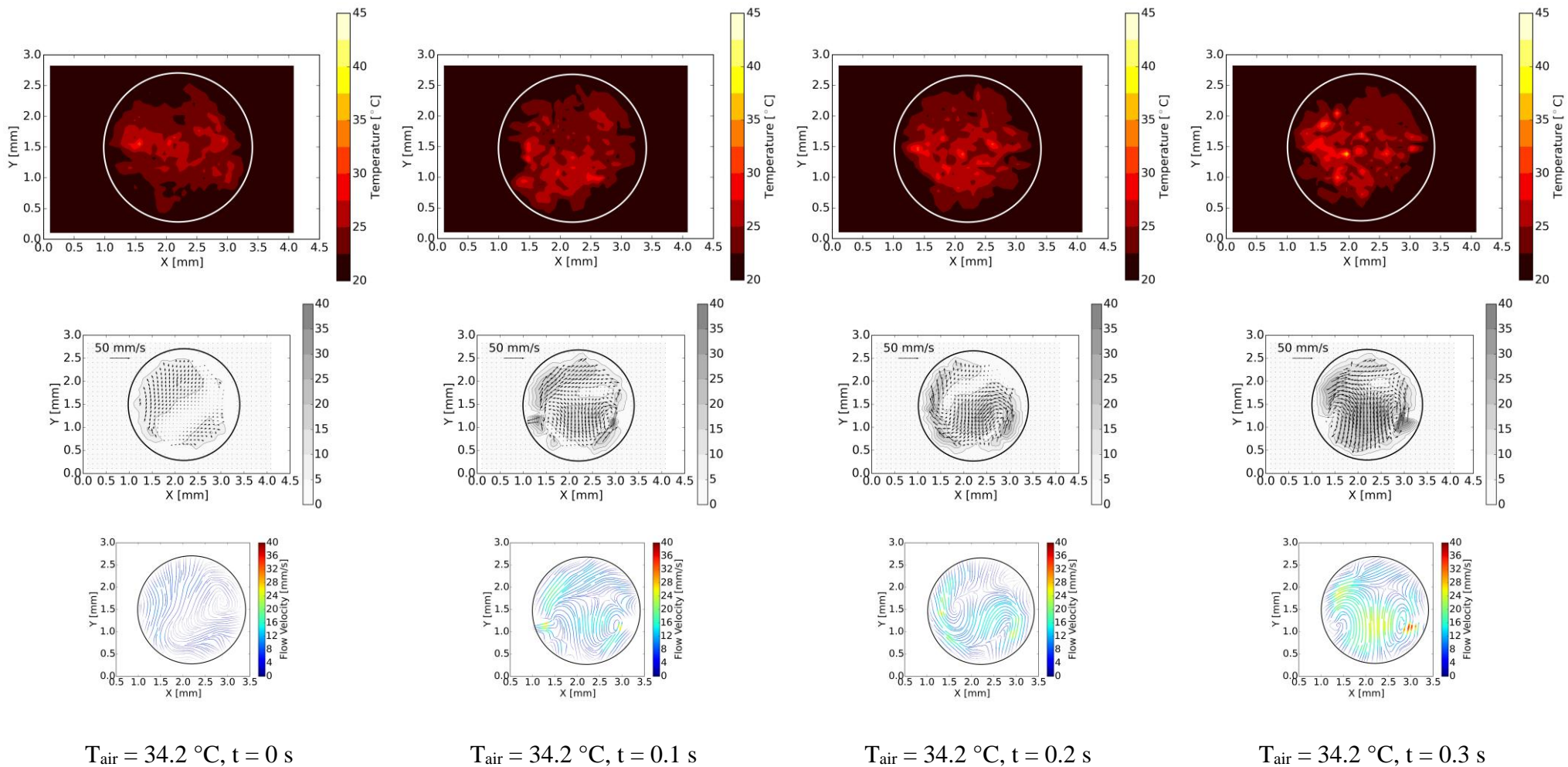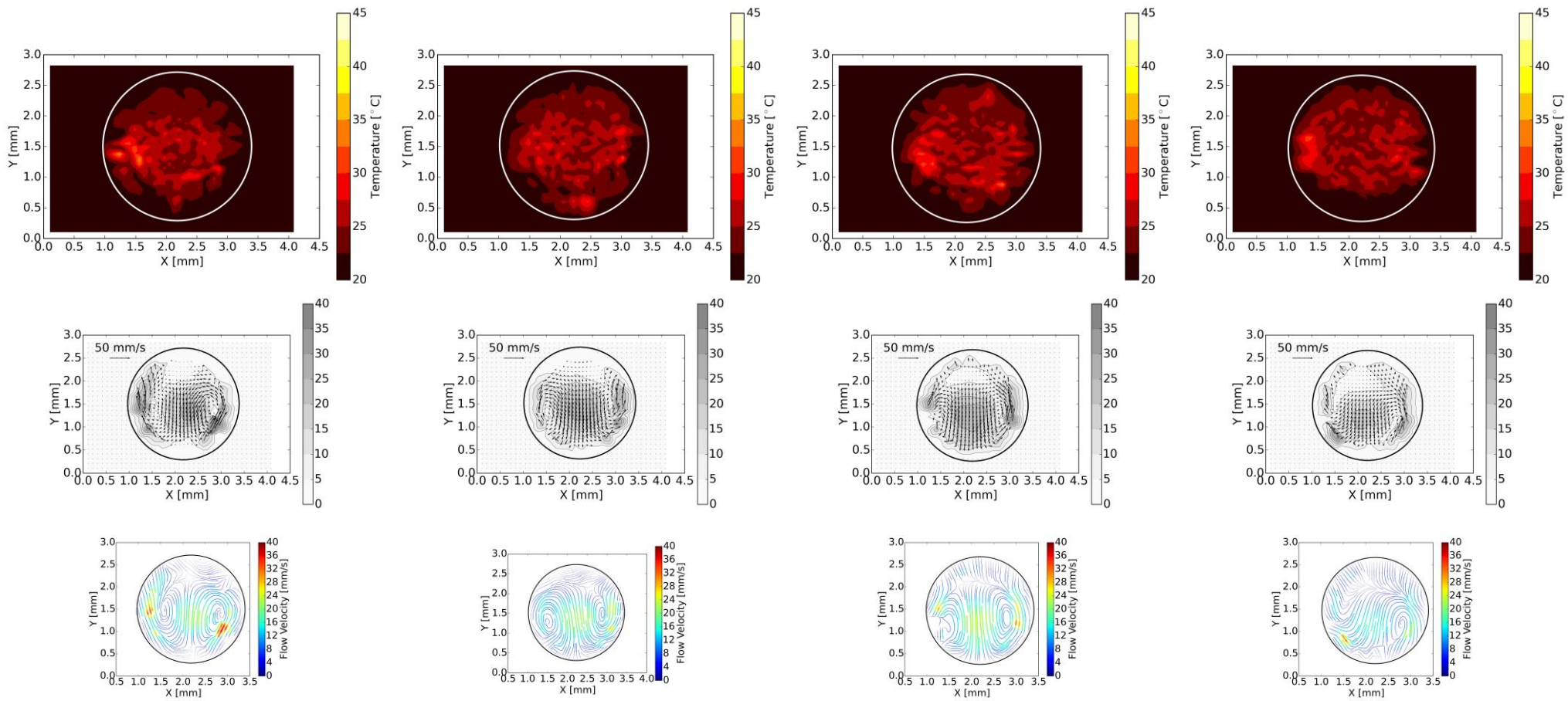
Figure 4-3g. Droplet internal temperature distributions, velocity distributions and streamlines during evaporation

T_{air} = 79.5 °C, t = 0.4 s T_{air} = 79.5 °C, t = 0.5 s T_{air} = 79.5 °C, t = 0.6 s T_{air} = 79.5 °C, t = 0.7 s

Figure 4-3h. Droplet internal temperature distributions, velocity distributions and streamlines during evaporation

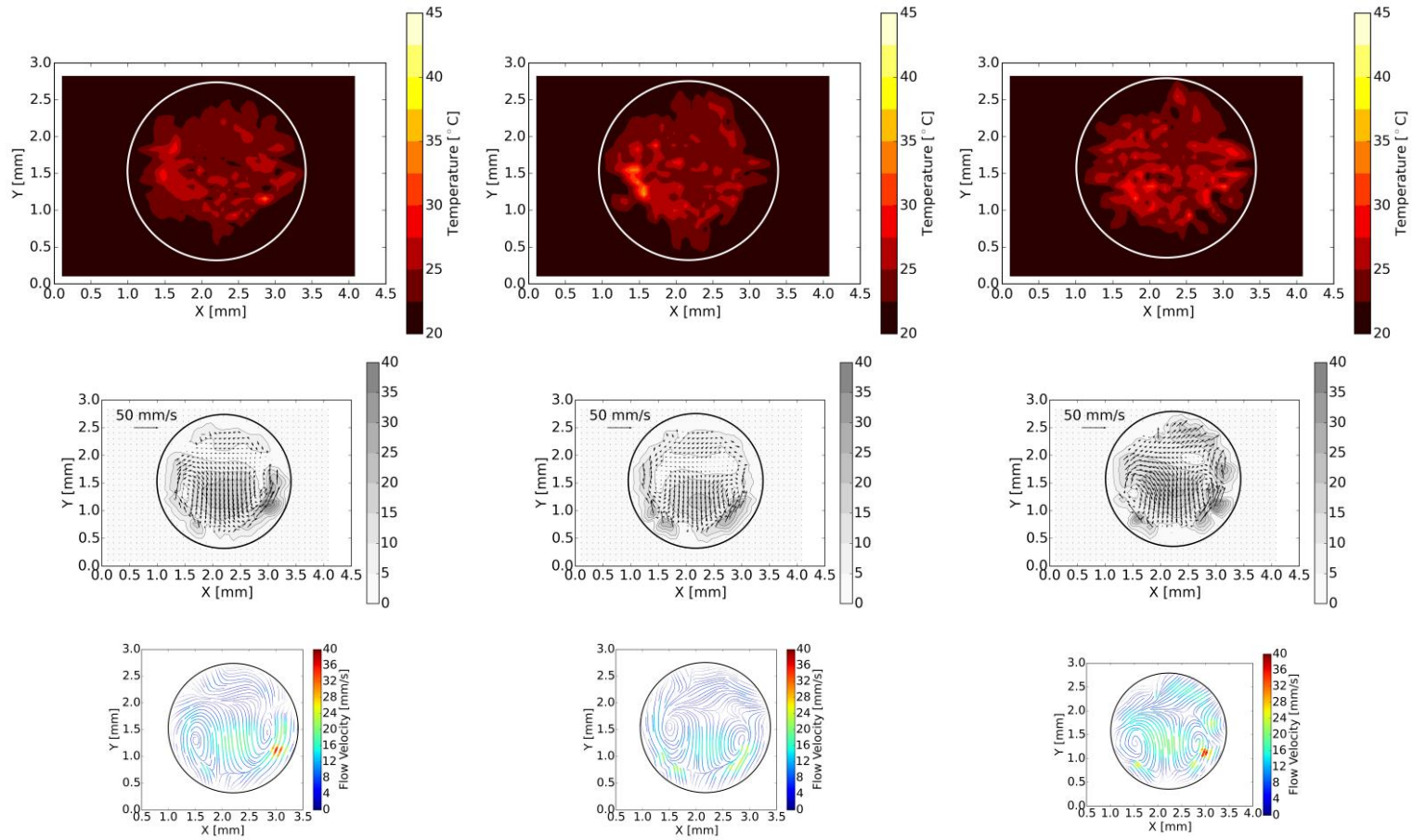T_{air} = 79.5 °C, t = 0.8 s T_{air} = 79.5 °C, t = 0.9 s T_{air} = 79.5 °C, t = 1.0 s

Figure 4-3i. Droplet internal temperature distributions, velocity distributions and streamlines during evaporation

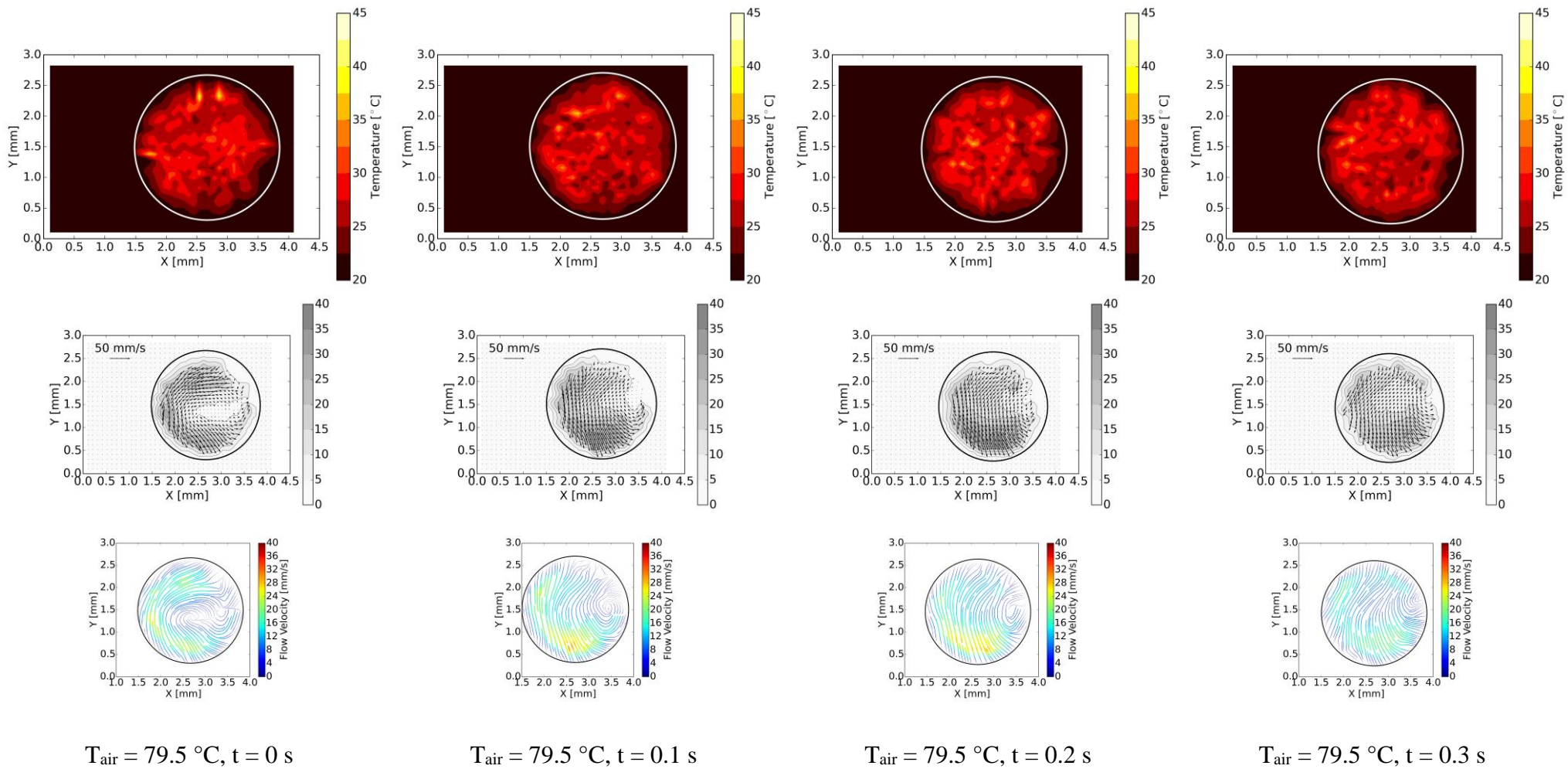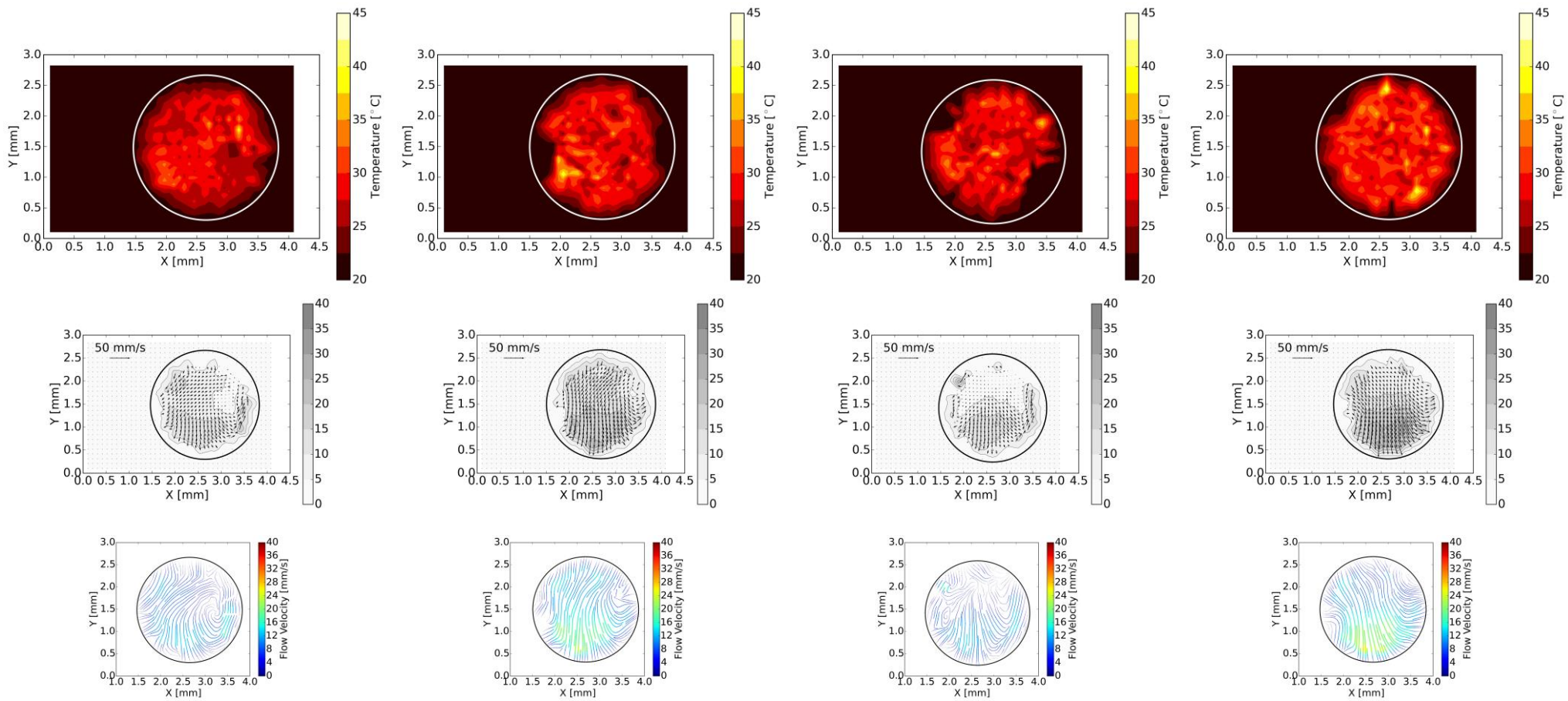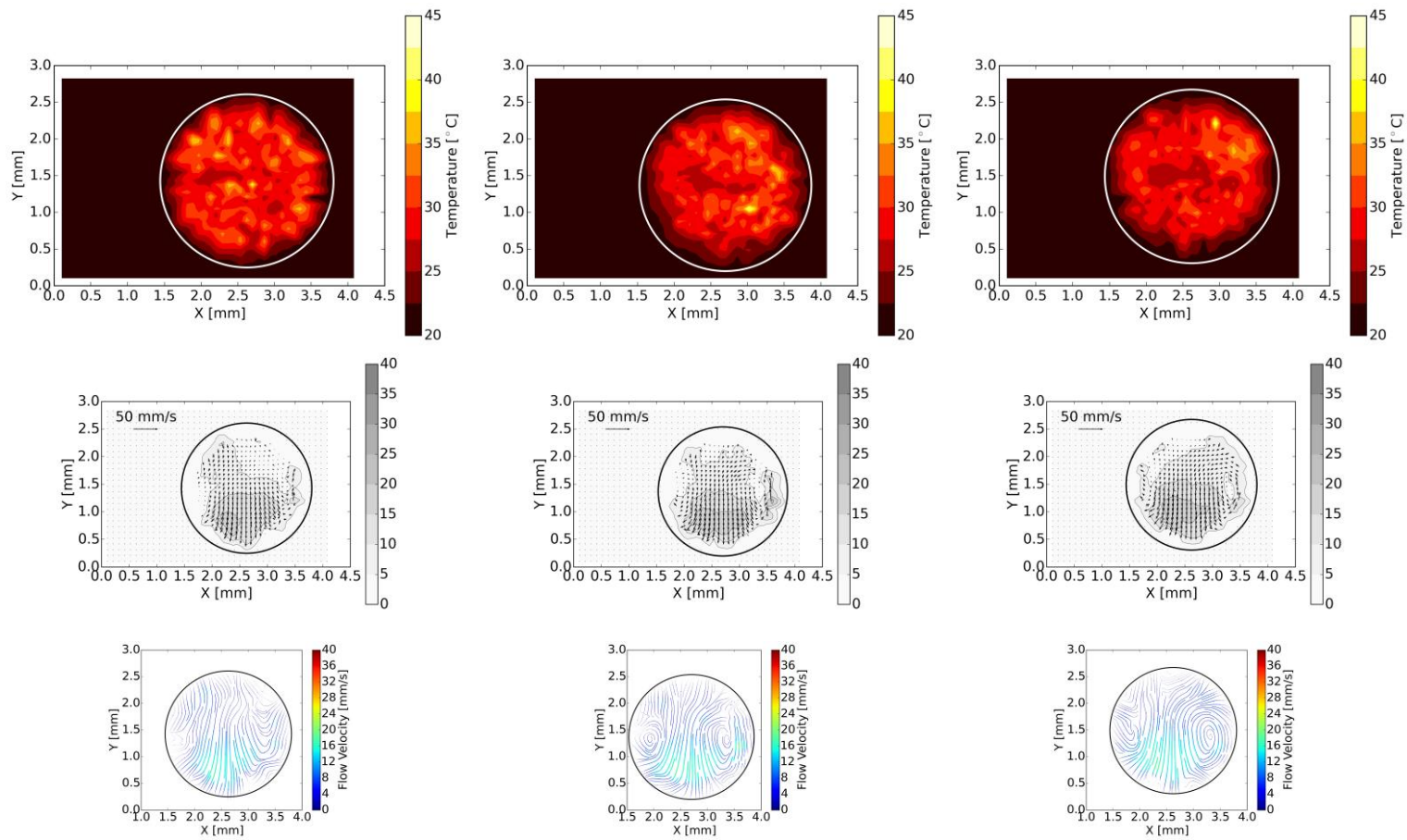Some non-uniformities within a temperature discrepancy of several °C can be observed in the temperature distributions in Figure 4-3. This kind of non-uniformities inside the obtained temperature distributions have been discussed in section 3.1.3. Besides, some area with higher temperature occurred inside the heated droplets due to the internal flow and heat exchange. No overall temperature gradient can be observed, neither on vertical direction nor on radial direction, which means that the internal water mixing was strong enough to exchange the gained heat inside the entire droplet. Besides, as above-mentioned in section 3.1.3, some desiccated layers of the particles were found to attach to the droplet surface, and the calculated decay rates of the phosphorescence emission of these layers also indicate similar temperatures as the results obtained inside the water droplet. Therefore, the spatial averaged temperature of the evaporating droplet can be used as the droplet surface temperature for a simply heat and mass transfer estimation. This assumption was usually used by researches for CFD simulations of containment spray.

In Figure 4-3, the temperature increase of droplet in 66.2 °C air stream and 79.5 °C air stream can be clearly observed. For 34.2 °C case, no obvious temperature increase can be observed within 1 s, which means that the evaporation heat absorption may be appropriately balance with the heat transfer between air stream and the droplet under that condition.

The internal flow developments also indicated different flow patterns inside the target droplets evaporating in air stream at different temperatures. In all three cases, although there were some initial flows inside the droplets, these initial flow were not so strong that downward flow were developed at the center of droplets within 0.2 s. Comparing with the 34.2 °C case, internal flow developed in the entire droplet in air stream at higher temperature.

However, in 34.2 °C case, the droplet internal flow pattern remained relatively stable thereafter, while in other cases, the droplet internal flow pattern kept changing during the evaporation, with droplet temperature increase, especially in 66.2 °C air

stream. With some randomness, these velocity fields were difficult to predict. As discussed in section 3.2.2, the water mixing of droplets and the hot air stream may further change the temperature gradient on the surface after Hill's vortex developed inside droplets, and the internal flow pattern may change again, and then and result in the velocity fields shown in Figure 4-3.
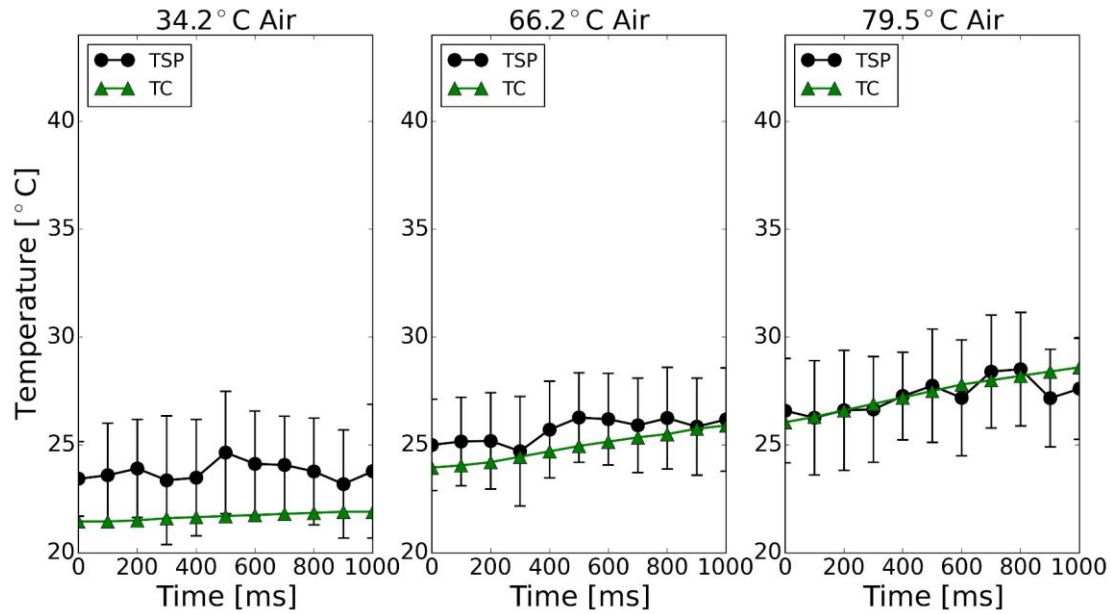
Figure 4-4. Comparison between droplet temperature variations measured by TSP (spatial averaged temperature) and thermocouple

Figure 4-4 gives the comparison between the droplet spatial averaged temperature measured by TSP and the droplet temperature measured by the inserted K-type thermocouple. Since these temperature data were obtained from individual experiments, the droplets had different initial temperatures before the air stream started. These difference may be caused by the air correspondingly heated up near the outlet of gas channel. Therefore, before air stream started, the droplets may be slightly heated up by the natural convection of the surrounding air circumstance. The differences in this temperature increase resulted in the discrepancy in droplet initial temperature.

Despite the differences in droplet initial temperature, the temperature variations obtained by TSP and thermocouple measurements fitted well with each other. Same tendency of temperature increase can be observed from this comparison shown in

Figure 4-4. Some fluctuations can be observed in the temperature variations measured by TSP, which is reasonable considering that TSP measurement is a two-dimensional measurement technique and the flow and heat exchange inside a droplet is three-dimensional.

4.3. Results discussion

As afore-mentioned in section 1.2, some well-known correlations of droplet heat and mass transfer are widely used by researches and nuclear engineers to simulate the behavior containment spray cooling and depressurization all over the world. In this section, some of the correlations will be briefly introduced and used to calculate the heat and mass transfer of droplet evaporation in the experiments in this study. The results will be compared and discussed.

4.3.1. Calculations using existing correlations of droplet heat and mass transfer

The well-known correlations used for Nu and Sh evaluations of droplet heat and mass transfer are shown in Table 4-2. All of the correlations shown in the table can be used for evaporating conditions at Re around 120, same as the experimental conditions in this study.

Table 4-2. Some well-known correlations for Nu and Sh evaluations

Correlations		Validity range
Frössling correlations [43]	$Nu = 2 + 0.552Re^{1/2}Pr^{1/3}$ $Sh = 2 + 0.552Re^{1/2}Sc^{1/3}$	$10 \leq Re \leq 1500$
Ranz & Marshall correlations [44]	$Nu = 2 + 0.6Re^{1/2}Pr^{1/3}$ $Sh = 2 + 0.6Re^{1/2}Sc^{1/3}$	$2 \leq Re \leq 200$
Clift et al. correlations [12]	$Nu = 1 + (1 + RePr)^{1/3}Re^{0.077}$ $Sh = 1 + (1 + ReSc)^{1/3}Re^{0.077}$	$Re \leq 400$
Renksizbulut correlations [16, 45]	$Nu = (2 + 0.57Re^{0.5}Pr^{0.333})(1 + B_H)^{-0.7}$	$Re \cong 100$
	$Sh = (2 + 0.87Re^{0.5}Sc^{0.333})(1 + B_M)^{-0.7}$	$10 \leq Re \leq 2000$

The Renksizbulut correlations also considered the effect of internal flow on heat transfer as enhanced liquid thermal conductivity as [16],

$$k_L' = k_L(1 + 0.056Re_L^{0.5}Pr_L^{0.333}) \quad [16] \tag{4-1}$$

Where,

$$Re_L^{0.5} = Re_\infty^{0.5}\left(\frac{\rho_L}{\rho_\infty}\right)^{1/3}\left(\frac{\mu_\infty}{\mu_L}\right)^{2/3} \quad [16] \tag{4-2}$$

Eq. 4-2 is the equation to calculate the Reynolds number of liquid, ρ_L, μ_L is the density and the viscosity of the liquid, and ρ_∞, μ_∞ is the density and the viscosity of the gas stream.

In Renksizbulut correlations, B_H is the heat transfer number ($B_H = (T_\infty - T_s)c_{p,g}/L$, where $c_{p,g}$ is the specific heat at constant pressure of the gas stream, and L is the latent heat of liquid), and B_M is the mass transfer number ($B_M = (Y_s - Y_\infty)/(1 - Y_s)$, where Y_s is the vapor mass fraction on the droplet surface and Y_∞ is the mass fraction of the evaporating species in the gas stream) [45].

With these correlations, Nu and Sh can be calculated from the evaporating conditions, and then the heat transfer coefficient h and mass transfer coefficient K can be calculated as follows,

$$h = \frac{k_g}{D} Nu \tag{4-3}$$

$$K = \frac{D_m}{D} Sh \tag{4-4}$$

In Eq. 4-3 and Eq. 4-4, k_g is the thermal conductivity of the gas, D_m is the mass diffusivity (the values for gas pair Air-H_2O can be checked from E. L. Cussler's literature [46]), and D is the characteristic length (usually the droplet diameter).

And then, with the obtained heat transfer coefficient h and mass transfer coefficient K, the heat and mass transfer can be calculated,

$$Q_H = \Delta t \cdot h \cdot A \cdot (T_\infty - T_s) \tag{4-5}$$

$$Q_M = \Delta t \cdot K \cdot A \cdot (c_{A_\infty} - c_{A_s}) \cdot M_L \tag{4-6}$$

Where Δt is the time, A is the area of droplet surface, M_L is the molar mass of the evaporating species and c_A is the molar concentration of the evaporating species, which can be calculated by assuming that the air flow was classical thermodynamic ideal gas,

$$c_A = \left. P_{vapor} \middle/ R_g T \right. \tag{4-7}$$

$$P_{vapor} = \varphi \cdot P_s(T) \tag{4-8}$$

In Eq. 4-7, P_{vapor} is the vapor partial pressure, R_g is the universal gas constant. For the gas stream, the vapor partial pressure can be calculated with Eq. 4-7, where φ is the air humidity. For evaporating droplets, the vapor partial pressure on the surface P_s is the saturated pressure at surface temperature T_s.

And then, the temperature increase of droplet can be simply calculated as,

$$\Delta T = (Q_H - Q_M L)/(m \cdot c_{p,L}) \tag{4-9}$$

Where, m is the mass of the evaporating droplet, and $c_{p,L}$ is the heat capacity of the fluid.

4.3.2. Comparisons and discussion

The temperature variations of evaporating droplets were calculated using the afore-mentioned four correlations. Figure 4-5 gives the comparison between the measured spatial averaged temperature variations and the calculated temperature variations of the evaporating droplets. The temperature variations of the air stream are also plotted in the graphs.
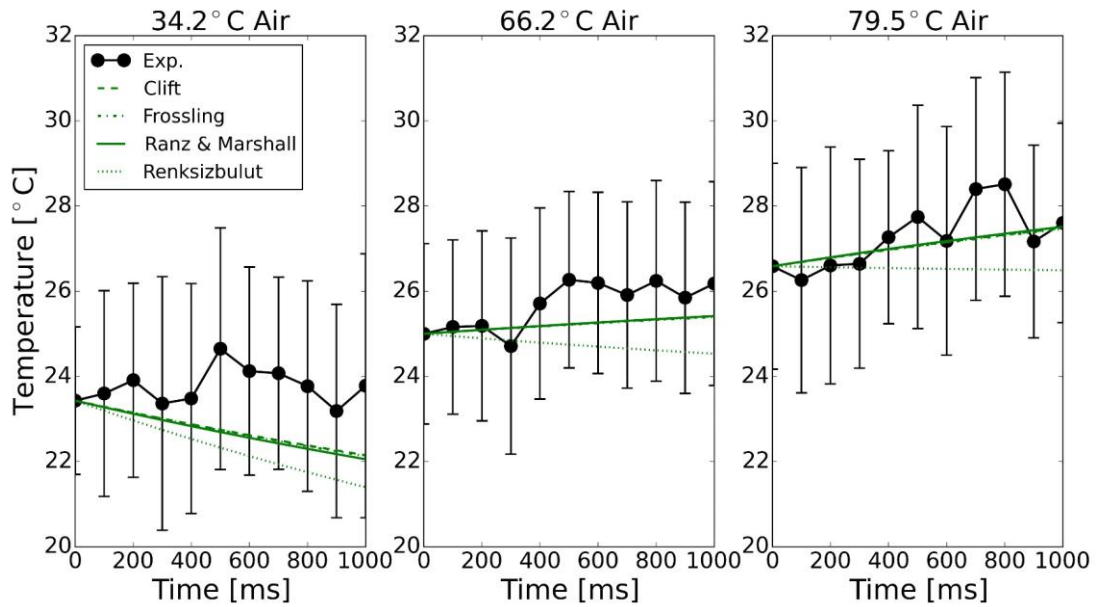
Figure 4-5. Comparison between measured spatial averaged temperature variations and calculated temperature variations of droplets

Figure 4-5 indicates that for the calculations of the transient beginning period of water droplet evaporation in temperature range from 20 °C to 80 °C, Clift, Frossling, Ranz & Marshall correlations give almost same results in the droplet temperature calculations, and Renksizbulut correlations may predict temperature decrease of the

evaporating droplet. Different from the experiment results, all the correlations predicted temperature decrease of droplet evaporating in 34.2 °C air stream.

As we know, the heat gained by droplets may cause the droplet temperature increase or the water evaporation on the droplet surface, and the water evaporation, which is the mass transfer, may cause the temperature decrease of droplets by phase-change heat absorption.

Using the recorded images of droplet evaporation, changes in the droplet size can be obtained. In this study, the volume of evaporating droplet was calculated as the volume of a symmetric solid of rotation, and then the volume of evaporated water can be calculated. In our experiment, since the size changes in 1 s were too small, and the temperature increase in the 1st second was only approximately 2 °C in 79.5 °C air stream, we assumed that the mass transfer coefficient was constant during the 1st second of droplet evaporation, since the Reynolds number and the Prandtl number of air remain almost constant within several °C near the room temperature. With the experimental data of droplet temperature variations and size changes, heat and mass transfer coefficients can be calculated.

Figure 4-6 gives a comparison between the heat and mass transfer coefficients of the water droplet evaporation in 79.5 °C air stream calculated using correlations and from experimental data. As above-mentioned, the mass transfer coefficient was assumed to be constant in the 1st second of droplet evaporation.
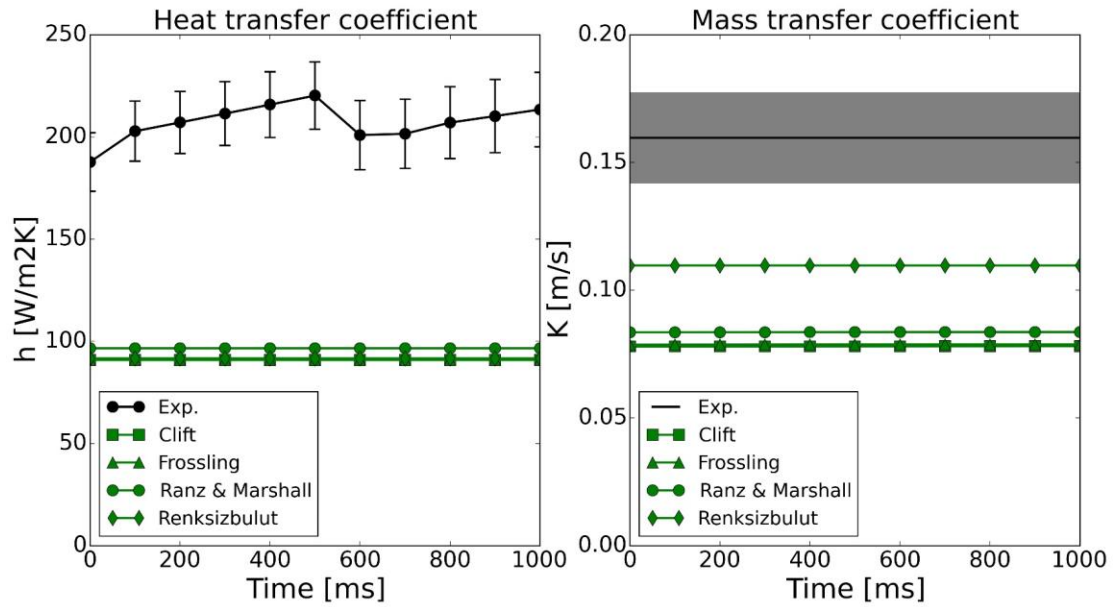
Figure 4-6. Comparison between heat and mass transfer coefficients of water droplet evaporation in 79.5 °C air stream obtained from experimental data and calculated using correlations

Figure 4-6 indicates that, for calculations of the water droplets evaporation in air stream, all the widely-used correlations under-predicted the heat transfer and the evaporation rate of the water droplets. The under-prediction is reasonable because these widely-used correlations didn't consider the enhancement of the Marangoni convection on the heat and mass transfer of droplet evaporation. The comparisons demonstrated that this enhancement is significant and must be taken into consideration.

In section 1.2.1, some previous researches were briefly referred, and the results demonstrated that the cooling and depressurization rate (heat and mass transfer) inside the containment vessel during the containment spray may be over-predicted using the widely-used correlations to calculate the heat and mass transfer between spray droplets and surrounding gas atmosphere. Because the depressurization mainly occurs in phase C of the four-phase spray process (as mentioned in section 1.1.2), the dominant mechanism is the contact condensation on droplets. Condensation is the inverse process of evaporation, so without the consideration of the Marangoni convection effects, the widely-used correlations may under-predict the heat and mass transfer of droplets

89

evaporation while over-predict the heat and mass transfer of steam condensation on droplets.

In conclusion, in further researches, more investigations on the mechanisms of droplet heat and mass transfer during evaporation and condensation are needed to modify the existing correlations or propose new ones for better trend predictions of the temperature variation and the phase change of containment spray droplets.

4.4. Conclusion of the chapter

In order to investigate the behavior of droplet evaporation heat and mass transfer, in this chapter, the PIV-TSP technique was used to measure the internal temperature and flow distributions of droplets evaporating in upward air stream simultaneously. The temperature variations (spatial averaged) of evaporating droplets measured by TSP technique fitted well with the results measured using a K-type thermocouple.

No overall temperature gradient can be observed inside droplets from the obtained temperature distributions, neither on vertical direction nor on radial direction, which means that the internal water mixing was strong enough to exchange the gained heat inside the entire droplet.

The internal flow developments also indicated different flow patterns inside the target droplets evaporating in air stream at different temperatures. The water mixing of droplets and the hot air stream may further change the temperature gradient on the surface after Hill's vortex developed inside droplets, and the internal flow pattern may change again.

The experimental results obtained are compared and discussed with the results of droplet heat and mass transfer calculation using some well-known correlations of droplet vaporization. The results indicate that for the calculations of the transient beginning period of water droplet evaporation in temperature range from 20 °C to 80 °C, these widely-used correlations may under-predict the heat and mass exchange of the

evaporating droplet, by ignoring the heat and mass transfer enhancement of the Marangoni convection. This problem is considered to affect the adequacy of CFD simulations of containment spray cooling and depressurization.

Therefore, in further researches, more investigations on the mechanisms of droplet heat and mass transfer during evaporation concerning the Marangoni convection are needed to modify the existing correlations or propose new ones for better trend predictions of the temperature variation and the phase change of containment spray droplets.

5. Conclusion and future works

5.1. Conclusion

1) PIV-TSP measurement technique

In order to investigate the heat and mass transfer mechanisms of flying droplets evaporating in surrounding gas experimentally, the high time- and spatial-resolution PIV-TSP technique for two-dimensional simultaneous temperature and flow distributions measurements was improved using an ex-situ calibration method.

The calibration results showed that the initial intensity of phosphorescence decay, which varied with the local particle density and laser power, affected the local decay constant as the coefficient of a half sigmoid function. Considering this initial intensity effect, a correlation curve between the temperature and exponential decay constant was obtained by referring to the Arrhenius equation.

The improved PIV-TSP measurement technique is free from the errors induced by local optical noise caused by the non-uniformity of the varying laser power and particle density. The improved ex-situ calibration method can also be applied to various measurement fields having different geometries.

2) Droplet evaporation experiments

The proposed PIV-TSP technique was applied to measure the temperature and flow distributions inside pendant water droplets evaporating in upward air stream, with an anti-distortion algorithm to correct the optical distortion induced by the curved surface of the droplet. This is the first time to measure the temperature and flow simultaneously inside water droplets at the beginning period of the evaporation in air stream which contains highly transient heat and mass exchange phenomena.

At the beginning of the droplet evaporation air stream, the flow motion developed in evaporating droplets was a toroidal convection pattern (the Hill's vortex) driven by

the shear force of the air stream. This kind of flow motion developed within 90 ms in droplets of approximately 2 mm diameter evaporating in 1 m/s air stream.

However, in high temperature air stream, the droplet internal flow developed rapidly with step changes, and the flow was developed in the entire droplet. It can be inferred that the droplet inner convective motion in upward hot air stream is induced by the Marangoni effect due to the gradient in the surface tension and the shear force of air flow, and the droplet internal water mixing can be enhanced by this circulation. The water mixing of droplets and the hot air stream may further change the temperature gradient on the surface after Hill's vortex developed inside droplets, and the internal flow pattern may change again due to the Marangoni convections.

The temperature variations (spatial averaged) of evaporating droplets measured by TSP technique fitted well with the results measured using a K-type thermocouple. No overall temperature gradient can be observed inside droplets from the obtained temperature distributions, neither on vertical direction nor on radial direction, which means that the internal water mixing was strong enough to exchange the gained heat inside the entire droplet.

The experimental data obtained are compared and discussed with the results of droplet heat and mass transfer calculation using some well-known correlations of droplet vaporization. The results indicate that for the calculations of the transient beginning period of water droplet evaporation in temperature range from 20 °C to 80 °C, the widely-used correlations may under-predict the heat and mass transfer rate of the evaporating water droplets, since these correlations didn't consider the enhancement of the Marangoni convection on the heat and mass transfer of droplet evaporation.

This problem is considered to affect the adequacy of the CFD simulations of containment spray cooling and depressurization. Condensation is the inverse process of evaporation, so without the consideration of the Marangoni convection effects, the widely-used correlations may under-predict the heat and mass transfer of droplets the evaporation while over-predict the heat and mass transfer of the steam condensation on

droplets. Since the dominant mechanism of containment spray is the contact condensation on droplets, the depressurization and cooling in containment vessel were over-predicted by the CFD simulations in previous researches.

With the detailed temperature and flow measurements inside evaporating droplets, our understanding of the heat and mass exchange mechanisms within a droplet's internal flow structures and temperature gradients can be potentially improved, and the related researches can further improve the design and prediction techniques of containment spray cooling and depressurization.

5.2. Future works

1) More investigations of PIV-TSP technique

At current stage, the PIV-TSP measurement technique has some limitations and possible errors that should be considered for technique improvements. Further researches should be conducted considering these problems:

1) Because of the optical distortion, it was not possible to obtain an accurate temperature and velocity distribution near the edge of the droplets.

2) Further investigation of the initial intensity effect is needed. The influences of temperature changes on the initial intensity effect on phosphorescence decay constant have not been clearly investigated and discussed.

3) In order to add particles into the water with good dispersion, a small amount of ethanol was added into the water sample. The evaporation of the ethanol may have effect on the droplet temperature variation and the droplet surface tension.

4) The particles inside the water droplet can agglomerate with each other and attach on the droplet surface in a short time (in tens of seconds). Therefore the PIV-TSP technique can only be applied for short time measurements.

2) More investigations of heat and mass transfer mechanisms of droplet evaporation

We have obtained plenty of experimental data, however, due to time constraints, the current theoretical investigation is only a preliminary part of the research.

In further researches, more investigations on the mechanisms of droplet heat and mass transfer during evaporation are needed to modify the existing correlations or propose new ones for better trend predictions of the temperature variation and the evaporation rate.

1) Numerical simulation should be conducted to compare with the measurement results of internal temperature and flow distributions, and the interactions between temperature and flow can be investigated.

2) The influences of the Marangoni convection should be further investigated. The influences of particles on the temperature sensitivity of droplet surface tension should also be considered. Experiments using silicone oil may provide good data for this investigation.

3) The droplet was shaking during the experiments. Although the oscillation didn't affect the PIV analysis using images with 1 ms time interval, the effects of this oscillation on the droplet internal flow and the surrounding gas flow should be considered in further researches.

3) Investigations of heat and mass transfer mechanisms of contact condensation on spray droplets

The dominant mechanism of containment spray is the contact condensation on flying droplets. Similar with the researches on droplet evaporation, further researches should be conducted to investigate the heat and mass transfer on water droplets in hot steam flow with direct contact condensation and droplet internal flow.

Acknowledgement

References

1. Figure 1-1 Accident mitigation systems inside containment vessel including containment spray cooling from Nuclear Regulatory Commission: https://adamswebsearch2.nrc.gov/webSearch2/view?AccessionNumber=ML16106A148.

2. Lemaitre, Pascal, and Emmanuel Porcheron. "Study of heat and mass transfers in a spray for containment application: Analysis of the influence of the spray mass flow rate." Nuclear Engineering and Design 239.3 (2009): 541-550.

3. Porcheron, Emmanuel, et al. "Experimental investigation in the TOSQAN facility of heat and mass transfers in a spray for containment application." Nuclear Engineering and Design 237.15 (2007): 1862-1871.

4. Lemaitre, Pascal, Emmanuel Porcheron, and Amandine Nuboer. "Study of heat transfer and mass transfer in a spray for containment application: analysis of the influence of spray temperature at the injection point." Nuclear Technology 175.3 (2011): 553-571.

5. Paladino, Domenico, and Jörg Dreier. "PANDA: a multipurpose integral test facility for LWR safety investigations." Science and Technology of Nuclear Installations, 2012.

6. Auban, O., R. Zboray, and D. Paladino. "Investigation of large-scale gas mixing and stratification phenomena related to LWR containment studies in the PANDA facility." Nuclear Engineering and Design 237.4 (2007): 409-419.

7. Erkan, Nejdet, et al. "Spray tests in PANDA to study accident mitigation in PWR containments." Proceedings of the International Conference Nuclear Energy for New Europe, Bled, Slovenia, Sept. 2009.

8. Babić, Miroslav, Ivo Kljenak, and Borut Mavko. "Simulations of TOSQAN containment spray tests with combined Eulerian CFD and droplet-tracking modelling." Nuclear Engineering and Design 239.4 (2009): 708-721.

9. Mimouni, S., et al. "Modelling of sprays in containment applications with a CMFD code." Nuclear Engineering and Design 240.9 (2010): 2260-2270.

10. Mimouni, S., et al. "Modelling of sprays in a multi-compartment geometry with a CMFD code." The 15th International Topical Meeting on Nuclear Reactor Thermal-Hydraulics, Pisa, Italy, May 2013.

11. Andreani, Michele, and Nejdet Erkan. "Analysis of spray tests in a multi-compartment geometry using the GOTHIC code." 18th International Conference on Nuclear Engineering. American Society of Mechanical Engineers, 2010.

12. Grace, J. R., R. Clift, and M. E. Weber. "Bubbles, drops and particles." Academic Press, New York (1978).

13. Sirignano, William A. Fluid dynamics and transport of droplets and sprays. Cambridge University Press, 2010.

14. Birouk, Madjid, and Iskender Gökalp. "Current status of droplet evaporation in turbulent flows." Progress in energy and combustion science 32.4 (2006): 408-423.

15. Hill, Micaiah John Muller. "On a spherical vortex." Proceedings of the Royal Society of London 55.331-335 (1894): 219-224.

16. Renksizbulut, M., and R. J. Haywood. "Transient droplet evaporation with variable properties and internal circulation at intermediate Reynolds numbers." International journal of multiphase flow 14.2 (1988): 189-202.

17. Abramzon, B., and W. A. Sirignano. "Droplet vaporization model for spray combustion calculations." International journal of heat and mass transfer 32.9 (1989): 1605-1618.

18. Stanislas, Michel, et al. "Main results of the third international PIV challenge." Experiments in Fluids 45.1 (2008): 27-71.

19. Coppeta, J., and C. Rogers. "Dual emission laser induced fluorescence for direct planar scalar behavior measurements." Experiments in Fluids 25.1 (1998): 1-15.

20. Zelelow, Biniam, et al. "Dual luminophor pressure sensitive paint: II. Lifetime based measurement of pressure and temperature." Sensors and Actuators B: Chemical 96.1 (2003): 304-314.

21. Omrane, Alaa, Gustaf Särner, and Marcus Aldén. "2D-temperature imaging of single droplets and sprays using thermographic phosphors." Applied Physics B: Lasers and Optics 79.4 (2004): 431-434.

22. Fan, L., et al. "Simultaneous, two-camera, 2D gas-phase temperature and velocity measurements by thermographic particle image velocimetry with ZnO tracers." Experiments in Fluids 58.4 (2017): 34.

23. Erkan, Nejdet, and Koji Okamoto. "Full-field spreading velocity measurement inside droplets impinging on a dry solid surface." Experiments in fluids 55.11 (2014): 1845.

24. Kinoshita, Haruyuki, et al. "Three-dimensional measurement and visualization of internal flow of a moving droplet using confocal micro-PIV." Lab on a Chip 7.3 (2007): 338-346.

25. Ninomiya, Nao, and Kazuma Yasuda. "Visualization and PIV measurement of the flow around and inside of a falling droplet." Journal of visualization 9.3 (2006): 257-264.

26. Someya, Satoshi, et al. "Combined measurement of velocity and temperature distributions in oil based on the luminescent lifetimes of seeded particles." Measurement Science and Technology 20.2 (2009): 025403.

27. Someya, Satoshi, et al. "Combined two-dimensional velocity and temperature measurements of natural convection using a high-speed camera and temperature-sensitive particles." Experiments in Fluids 50.1 (2011): 65-73.

28. Hishida, K., and J. Sakakibara. "Combined Planar laser-induced fluorescence–particle image velocimetry technique for velocity and temperature fields." Experiments in Fluids 29 (2000): S129-S140.

29. Omrane, Alaa, et al. "Simultaneous 2D flow velocity and gas temperature measurements using thermographic phosphors." Applied Physics B: Lasers and Optics 92.1 (2008): 99-102.

30. Funatani, S., N. Fujisawa, and H. Ikeda. "Simultaneous measurement of temperature and velocity using two-colour LIF combined with PIV with a colour CCD camera and its application to the turbulent buoyant plume." Measurement Science and Technology 15.5 (2004): 983.

31. Qian, Zhou, et al. 2017 "Ex situ calibration technique for simultaneous velocity and temperature measurements inside water droplets using temperature-sensitive particles." Measurement Science and Technology 28 (2017): 075203.

32. Liebsch, Gregor, Ingo Klimant, and Otto S. Wolfbeis. "Luminescence Lifetime Temperature Sensing Based on Sol‐Gels and Poly (acrylonitrile) s Dyed with Ruthenium Metal‐Ligand Complexes." Advanced Materials 11.15 (1999): 1296-1299.

33. Nagl, Stefan, et al. "Method for simultaneous luminescence sensing of two species using optical probes of different decay time, and its application to an enzymatic reaction at varying temperature." Analytical and bioanalytical chemistry 393.4 (2009): 1199-1207.

34. Einstein, Albert. Investigations on the Theory of the Brownian Movement. Courier Corporation, 1956.

35. Photron FASTCAM Viewer Operation Manual. http://www.biomech.hacettepe.edu.tr/manuals/ Photron_FASTCAM_Viewer_Manual_Rev2410en.pdf

36. Kang, Kwan Hyoung, et al. "Quantitative visualization of flow inside an evaporating droplet using the ray tracing method." Measurement Science and Technology 15.6 (2004): 1104.

37. Minor, G., P. Oshkai, and N. Djilali. "Optical distortion correction for liquid droplet visualization using the ray tracing method: further considerations." Measurement Science and Technology 18.11 (2007): L23.

38. Kumar, S. Santosh, et al. "Internal flow measurements of drop impacting a solid surface." Experiments in Fluids 58.3 (2017): 12.

39. Wong, Shwin-Chung, and Ar-Cheng Lin. "Internal temperature distributions of droplets vaporizing in high-temperature convective flows." Journal of fluid mechanics 237 (1992): 671-687.

40. Sirignano, William A. "Fuel droplet vaporization and spray combustion theory." Progress in Energy and Combustion Science 9.4 (1983): 291-322.

41. LeClair, B. P., et al. "A theoretical and experimental study of the internal circulation in water drops falling at terminal velocity in air." Journal of the Atmospheric Sciences 29.4 (1972): 728-740.

42. Tam, Daniel, et al. "Marangoni convection in droplets on superhydrophobic surfaces." Journal of Fluid Mechanics 624 (2009): 101-123.

43. Froessling, N. "Uber die Verdunstung Fallender Tropfen (The Evaporation of Falling Drops). " Gerlands Beitrage zur Geophysik 52 (1938):107-216.

44. Ranz, W. E., and W. R. Marshall. "Evaporation from drops." Chemical Engineering Progress 48.3 (1952): 141446.

45. Renksizbulut, Metin, Rick Nafziger, and Xianguo Li. "A mass transfer correlation for droplet evaporation in high-temperature flows." Chemical Engineering Science 46.9 (1991): 2351-2358.

46. Cussler, Edward Lansing. Diffusion: mass transfer in fluid systems. Cambridge university press, 2009.